

OPTICAL INVESTIGATIONS AND EFFICIENCY MEASUREMENTS
OF A DUAL-MODE TURBULENT JET IGNITION ENGINE UNDER
LEAN AND HIGH-EGR NEAR-STOICHIOMETRIC CONDITIONS

By

Ravi Teja Vedula

A DISSERTATION

Submitted to
Michigan State University
in partial fulfillment of the requirements
for the degree of

Mechanical Engineering – Doctor of Philosophy

2016

ABSTRACT

OPTICAL INVESTIGATIONS AND EFFICIENCY MEASUREMENTS OF A DUAL-MODE TURBULENT JET IGNITION ENGINE UNDER LEAN AND HIGH-EGR NEAR-STOICHIOMETRIC CONDITIONS

By

Ravi Teja Vedula

Gasoline is the primary fuel being used in its original or in blended form for the current light-duty vehicles of the automotive industry. It is essential to understand the details of gasoline combustion events in modern engines and develop combustion technologies to improve the thermal efficiency and meet the 2025 emissions targets. The current work focuses on the testing and development of a gasoline engine, equipped with MSU patent-pending dual-mode turbulent jet ignition (DM-TJI) concept, which was demonstrated to deliver high thermal efficiency. In a DM-TJI system, mixture composition in the pre-chamber can be individually controlled from that of main chamber as the fuel and air are independently admitted to the pre-chamber. Lean-burn combustion offers increased thermal efficiency and low criteria emissions compared to spark ignition engine of today. Ignition delay times and combustion behavior of ultra-lean iso-octane/air mixture (global air/fuel equivalence ratio, $\lambda \cong 3.0$) were first studied in a DM-TJI-equipped rapid compression machine. Fuel spray recordings in the pre-chamber were completed using borescope and high speed camera imaging. Main chamber visualizations of the reacting jet and combustion were simultaneously recorded using another high speed camera. Providing pre-chamber air injection pulse during the pre-chamber fuel injection event enhanced the combustion burn rates under certain injection timings and mitigated particulate formation.

These RCM results were then applied as baseline operating conditions for the DM-TJI engine testing. Combustion in this DM-TJI engine was studied at compression ratios of 9.5 and

12.0. With the low compression ratio engine, unthrottled operating conditions for a global $\lambda \cong 1.85$ were identified that offered an indicated efficiency of $46.0\% \pm 1\%$ at 1500 rpm and 6.0 bar IMEP. The high compression ratio DM-TJI engine with about 32% nitrogen-simulated exhaust gas recirculation (EGR) dilution delivered an indicated efficiency of $46.6\% \pm 1\%$ under near-stoichiometric operation and at 1500 rpm and 7.7 bar IMEP.

ACKNOWLEDGEMENTS

I would like to thank MSU's Graduate School of Admissions and the Department of Mechanical Engineering for providing this once-in-a-lifetime opportunity of meeting Prof. Harold Schock and for allowing me to pursue my doctoral degree under his kind supervision. I wholeheartedly thank my PhD committee members, Prof. Dennis Miller, Prof. George Zhu, and Prof. Giles Brereton for their understanding, technical guidance and mentoring throughout my graduate studies at MSU. Also, I thank Prof. Andre Benard for his mentoring during my first year. I thank each and every Professor who offered one or more courses that I took at MSU. There are many individuals who provided their assistance during daily activities at the lab while leaving many cherishing moments. I thank: Tom Stuecken whose friendly, witty, joyous acts makes me forget that I work with a highly experienced person with abundant knowledge of technical know-how; Brian Rowley for his persistent "glad to be of help" attitude; The Higels (Jen & Jeff) for their prompt help and for keeping me sane with their enthusiastic questions about the research work; Kevin Moran for sharing some insights on engine controls and for teaching me how to fine-tune a question to make it more specific. I thank MSU Alumni: Mayank Mittal from IITM and Cody Baldwin Squibb from FCA US LLC., working with whom was both a challenging and a valuable experience. I thank current and former graduate students: Gerald Gentz, Ali Kharazmi, Charles J. Maines, Jie Yang, Nariman Mansouri, Ruitao Song, Masumeh Gholamisheeri, Atefeh Tolou ("Ati"), Prasanna Chinnathambi, and Tao Zeng for creating a friendly ambience at the lab. I seize this opportunity to seek blessings from my parents and thank my family members, relatives, teachers/lecturers, and every other being in this world that directly or without my notice, created favorable atmosphere towards the completion of my degree.

PREFACE

A boy found a plant that kindly offers good fruit.

The boy is filled with joy and enjoys both the fruit and the companionship of the silent plant.

The boy develops enormous attachment to the fruit and its flavor that he remains ignorant of how much the plant gets hurt while plucking the fruits in a haste.

The plant smiles in return and continues to provide the fruit until its roots start rotting.

Realizing this, the boy now feels more responsible than ever before and decides to take care of his most beloved plant and find a cure for its roots.

Plant – Earth

Fruits – Oil

Roots – Living Beings

Root rot – Emissions Aftereffects

Boy – Engine User/Developer

TABLE OF CONTENTS

LIST OF TABLES	viii
LIST OF FIGURES	ix
KEY TO SYMBOLS AND ABBREVIATIONS	xii
CHAPTER 1	1
Introduction	1
1.1 STRATIFIED CHARGE COMBUSTION	1
1.2 PRE-CHAMBER INITIATED COMBUSTION	4
1.2.1 Swirl Chamber Spark Plugs	5
1.2.2 Turbulent Jet Ignition	5
1.3 POTENTIAL IMPROVEMENTS IN GASOLINE-FUELED ENGINES	7
1.3.1 Thermal Efficiency	7
1.3.1.1 Production Engines	7
1.3.1.2 Single-Cylinder Research Engines	8
1.3.2 Emissions Control	9
1.3.2.1 Evaluation of Exhaust Aftertreatment Systems	9
1.3.2.2 Diluted Lean Combustion	11
1.4 CONTENTS OF THE PRESENT WORK	15
1.4.1 Dual-Mode Turbulent Jet Ignition	15
CHAPTER 2	17
Effect of Pre-chamber Air and Fuel Injection on Iso-octane Combustion in Turbulent Jet Ignition Mode	17
2.1 SYNOPSIS	17
2.2 EXPERIMENTAL SETUP: DM-TJI CHARACTERIZATION USING A RAPID COMPRESSION MACHINE	17
2.2.1 Fuel Spray and Combustion Visualizations	20
2.2.1.1 Pre-chamber	20
2.2.1.2 Main Chamber	21
2.2.2 Operating Conditions	22
2.3 RESULTS AND DISCUSSION	25
2.3.1 Fuel Spray in the Pre-chamber: With and Without Air Injection	25
2.3.2 Effect of Pre-chamber Fuel Injection Timing	26
2.3.3 TJI-Initiated Combustion in the Main Chamber	29
2.3.4 DM-TJI Initiated Combustion in the Main Chamber	31
2.3.5 Effect of Pre-chamber Air Injection Pressure	33
2.4 SUMMARY	38
CHAPTER 3	41

Visualizations and Efficiency Measurements of Liquid Gasoline Combustion in a Dual-Mode Turbulent Jet Ignition Optical Engine	41
3.1 SYNOPSIS.....	41
3.2 EXPERIMENTAL SETUP.....	41
3.2.1 Engine Operation.....	41
3.2.2 Engine Controls and Data Acquisition.....	43
3.2.3 Combustion Imaging.....	46
3.3 RESULTS AND DISCUSSION	47
3.3.1 DM-TJI Engine: With a Low-Pressure Injector for Main Chamber Fueling.....	47
3.3.2 DM-TJI Engine: With a High-Pressure Injector for Main Chamber Fueling	50
3.4 SUMMARY	52
CHAPTER 4	54
Thermal Efficiency of a High Compression Ratio Dual-Mode Turbulent Jet Ignition Gasoline Engine Under Near-Stoichiometric Operation	54
4.1 SYNOPSIS.....	54
4.2 EXPERIMENTAL SETUP.....	54
4.2.1 High Compression Ratio DM-TJI Engine.....	54
4.2.2 Nitrogen-Simulated EGR Dilution.....	56
4.3 RESULTS AND DISCUSSION	58
4.3.1 DM-TJI Engine: Without EGR Dilution.....	58
4.3.2 DM-TJI Engine: With EGR Dilution.....	61
4.3.2.1 Effect of Air Injection in the Pre-chamber.....	61
4.3.2.2 Main Chamber Fuel Injection Pulse Width.....	62
4.3.2.3 Spark Sweep for Early Pre-chamber Fuel injection Condition.....	64
4.3.3 Thermal Efficiency of the DM-TJI Engine	69
4.4 SUMMARY	71
CHAPTER 5	74
Concluding Remarks	74
APPENDIX.....	76
REFERENCES	90

LIST OF TABLES

Table 2.1: Specifications of TJI-equipped RCM Apparatus	19
Table 2.2: Text Matrix for Fuel and/or Air Injection in the Pre-chamber	24
Table 2.3: Ignition Times for Different Fuel Timings With and Without Pre-chamber Air Injection	28
Table 2.4: Ignition Times and Main Chamber Burn Durations for Different Air Injection Pressures	34
Table 3.1: DM-TJI Engine Specifications.....	43
Table 3.2: Fuel and Air Injection Settings	46
Table 3.3: Output Variables of Interest.....	51
Table 4.1: Specifications of DM-TJI Engine with Extended Metal Piston.....	61
Table 4.2: DM-TJI Engine Results with Approximately 25% EGR Dilution	63
Table 4.3: Reported Efficiencies of Single-Cylinder Light Duty Engines (displacement <1 L). 70	
Table 4.4: Most Favorable Operating Conditions for the DM-TJI Engine at 1500 rpm.....	71
Table A.1: DM-TJI Engine Model Specifications	79
Table A.2: Purge System Model Specifications.....	80
Table A.3: Mean Effective Pressures (bar) in the Purge Pump and the Main chamber.....	87

LIST OF FIGURES

Figure 2.1: Optically accessible rapid compression machine incorporated with the pre-chamber fuel and air injection TJI design.....	18
Figure 2.2: Close-up view of the TJI setting installed in the RCM.	21
Figure 2.3: Raw image during main chamber combustion (left) and corresponding filtered image showing the particulate index (right).	22
Figure 2.4: Instantaneous high-speed recordings of fuel spray event in the pre-chamber without pre-chamber air injection.	26
Figure 2.5: Instantaneous high-speed recordings of fuel spray event in the pre-chamber with pre-chamber air injection (200 psi).	26
Figure 2.6: Details of main chamber pressure plots for different pre-chamber fuel injection timings (without pre-chamber air injection).	28
Figure 2.7: Instantaneous images of jet entry and combustion events in the main chamber for different fuel injection timings (without pre-chamber air injection).	30
Figure 2.8: Instantaneous images of jet entry and combustion events in the main chamber for different fuel injection timings and with pre-chamber air injection (200 psi).	32
Figure 2.9: Instantaneous images of fuel spray event in the pre-chamber for different pre-chamber air injection pressures; pre-chamber fuel SOI was at PPC=3 bar.	34
Figure 2.10: Jet entry and combustion events in the main chamber for different air injection pressures.....	36
Figure 2.11: Normalized particulate indices for different air injection pressures.	38
Figure 3.1: Dual-Mode TJI optical engine (left) and sectional view showing the details of its architecture (right).	42
Figure 3.2: Front- and bottom-views of the spark plug combined with pressure sensor for pre-chamber measurements.....	44
Figure 3.3: Optical Engine Controls System.	45
Figure 3.4: Camera setup for bottom-view imaging of combustion.....	47

Figure 3.5: Pre-chamber and main chamber pressure traces and phase-synchronized images of combustion events for $\lambda=1.8$	48
Figure 3.6: Camera view of the combustion chamber.	49
Figure 3.7: Combustion images showing burning droplets for different fuels in the pre- and main chamber.....	50
Figure 3.8: Main chamber combustion images for three different pre-chamber fuel pulse widths.	52
Figure 4.1: High compression ratio DM-TJI engine with metal piston.....	55
Figure 4.2: Experimental setup for DM-TJI engine with EGR dilution.....	57
Figure 4.3: Pre-chamber pressures and main chamber heat release rates for different spark timings.....	59
Figure 4.4: Pre-chamber and main chamber pressures for different pre-chamber fuel injection timings.....	61
Figure 4.5: Effect of having pre-chamber air injection on the combustion of diluted mixture consisting an intake O_2 of 15.5% (left) and 15.2% (right).....	62
Figure 4.6: Comparison of pressures for different main chamber fuel pulse widths (left) and zoomed-in view of pre-chamber pressure first peak regions.	64
Figure 4.7: Graphical plots showing the DM-TJI engine test results with approx. 30% EGR. ..	66
Figure 4.8: Main chamber heat release rates for EFI-1 (left) and EFI-2 (right) injection conditions.....	67
Figure 4.9: Main chamber combustion images for three different spark timings.....	68
Figure A.1: DM-TJIv concept with air supplied through a camshaft-controlled poppet valve (figure taken from patent disclosure).....	78
Figure A.2: (a) Cam-driven purging system; (b) a section of the numerical model showing the corresponding purging system.	79
Figure A.3: Plunger position profile in an engine cycle.....	81
Figure A.4: GT – Power model schematic of the DM-TJIv engine.	82

Figure A.5: Plot comparing the measured and calculated pressure traces in the main chamber during firing cycle..... 84

Figure A.6: Mass flow rate at the pre-chamber valve for different purge pump volumes. 85

Figure A.7: Major burned species mass fractions for the three cases in (a) Pre-chamber and (b) Vol object (above pre-chamber valve)..... 86

KEY TO SYMBOLS AND ABBREVIATIONS

CO	Carbon monoxide
CO ₂	Carbon dioxide
ΔP	Pressure differential
H ₂	Hydrogen
λ	Air/fuel equivalence ratio (= $AFR/AFR_{Stoichiometric}$)
N ₂	Nitrogen gas
NO	Nitric oxide
NO ₂	Nitrogen dioxide
N ₂ O ₄	Nitrogen tetroxide
O ₂	Oxygen gas
P _{PC}	Pre-chamber pressure
T	Temperature
AFR	Air-to-fuel ratio
aSOI	After start of injection
aSPI	After spark initiation
aTDC	After top dead center
BDC	Bottom dead center
BMEP	Brake mean effective pressure
bTDC	Before top dead center
CAD	Crank angle degree
CAS	Combustion analysis system

COV	Coefficient of variation
CVCC	Compound vortex controlled combustion
DI	Direct injection
DM-TJI	Dual-mode turbulent jet ignition
EFI	Early fuel injection
EGR	Exhaust gas recirculation
fps	Frames per second
GDI	Gasoline direct injection
HC	Hydrocarbons
HCCI	Homogeneous charge compression ignition
IC	Internal combustion
IMEP	Indicated mean effective pressure
LAG	Lavinia Aktyvatsia Gorenia
LFI	Later fuel injection
MFB	Mass fraction burned
MFI	Middle fuel injection
NMOG	Non-methane organic gases
NOx	Mixture of oxides of nitrogen
NPI	Normalized particulate index
OEM	Original equipment manufacturer
PCCI	Pre-mixed charge compression ignition
PCI	Pre-chamber ignition
PFI	Port-fuel-injection

PM	Particulate mass/matter
PMEP	Pumping mean effective pressure
PN	Particulate number
RCCI	Reactivity controlled compression ignition
RCM	Rapid compression machine
rpm	Revolutions per minute
SACI	Spark assisted compression ignition
SCR	Selective catalytic reduction
SI	Spark-ignition
SOI	Start of injection
TDC	Top dead center
TJI	Turbulent jet ignition
TTL	Transistor-transistor logic
TWC	Three-way catalyst

CHAPTER 1

Introduction

Improvement in thermal efficiency and a reduction in criteria emissions continue to be major challenges to the IC engine community. Most passenger cars utilize less than 10% of their maximum engine power during daily commute [1]. This fact highlights the importance of improving engine part-load efficiency. Direct injection is more advantageous than the port fuel injection for engine part-load operating conditions. This is because with port fuel injection, the engine load is controlled by throttling the intake which incurs pumping losses. Direct-injection system offers unthrottled operation wherein the engine load can be controlled by the amount of fuel injected, thereby avoiding pumping losses. Some of the strategies currently being pursued, in a broad view, to improve part-load efficiency of direct-injection engines and reduce exhaust emissions are: (i) engine downsizing and turbo/supercharging [2, 3]; (ii) use of alternative fuels [4, 5]; (iii) variable valve timing and variable compression ratio engines [6-8]; and (iv) stratified charge combustion [9-13].

1.1 STRATIFIED CHARGE COMBUSTION

In stratified charge direct-injection spark ignition engines (DISI), fuel is injected in the cylinder during compression stroke (for part-load conditions). In this way, a small volume of heterogeneous fuel-rich mixture is created close to the spark plug. The turbulent flame initiated upon ignition of this mixture at the spark plug leads to diffusion-controlled combustion of the remaining bulk mixture. The composition leanness of this mixture increases with distance from the spark plug in the combustion chamber. The stratification in DISI engines can be attained by

one of the three conventional systems: wall-guided stratified charge, air-guided stratified charge, or spray-guided stratified charge combustion systems [12].

In wall-guided systems, a contoured bowl or cavity in the piston crown aids in redirecting the fuel vapor towards the spark plug. In air-guided systems, motion of air charge inducted in the cylinder guides the fuel spray towards the spark plug. The desired air swirl and tumble flow is achieved by choosing suitable orientation and geometry of inlet ports, inlet valve deactivation or by introducing charge motion control devices such as baffles in the inlet ducts. In spray-guided systems, fuel is sprayed from a fuel injector that is placed close to the spark plug. Also, the spark plug electrodes are oriented carefully with respect to the spray direction. The close injector-to-spark plug spacing and short time separation between injection and spark allow a compact fuel cloud, resulting in better combustion phasing (faster burn with less cyclic variability) [13]. Wall- and air-guided stratified combustion systems have shown unfavorable emission, specific power, and fuel consumption characteristics due to the impingement of directly-injected fuel on the piston and cylinder wall [14-16].

Spray-guided systems are capable of overcoming several unfavorable consequences seen with the other two systems. However, spray-guided systems are susceptible to random misfires and partial burns. Recently, Fansler et al. [17] reviewed various scenarios of combustion instabilities seen with spray-guided stratified charge systems in spark ignition engines under part-load operating conditions. The following are the highlights extracted from that work on spray-guided systems.

- Two types of high-pressure injectors have been used in the past: solenoid-actuated, inwardly opening multi-hole injector and piezo-electrically actuated, outwardly

opening A-nozzle injector. Only the latter type have gone into mass production to date; see for example [18].

- A one crank angle degree (CAD) difference in spark timing between two experiments resulted in a misfire and a partial burn. This observation illustrates the sensitivity of spray-guided stratified charge systems to small changes in the operating conditions.
- Spark, when fired shortly before the spray plume reached the plug, experienced high-frequency restrikes indicating very rapid spark stretching due to the intense spray-induced flow. Also, spark extinctions were occasionally observed due to interaction of liquid droplets with plasma.
- Factors identified to cause combustion instabilities were: (i) In-cylinder flow variations that hindered the flame kernel from reaching the bulk of the fuel present in the piston bowl. (ii) Low flame speeds due to presence of locally lean mixtures. (iii) Retarded ignition kernel that would consequently face overly lean regions nearby, due to transport and mixing phenomena, resulting in flame extinction.

Multiple injections could improve combustion stability of spray-guided stratified charge systems [19]. This could be achieved by (i) delivering a rich mixture to the flame kernel formed from the previous injection; (ii) driving the burning mixture into the piston bowl, where the major part of the fuel would exist; or (iii) reducing spray-induced turbulence during initial flame kernel formation. The multiple injection strategy would especially be beneficial with piezo-injectors, which are usually preferred for their fast response times [17].

Another issue of concern with respect to DI stratified charge operation is the significantly higher particulate emissions [20]. Maricq et al. [21] reported that the particulate number emissions increased by a factor of 10-40 when the engine operation was switched from homogenous to

stratified mode. In another study, nine light-duty gasoline direct-injection (GDI) engine vehicles equipped with either wall-guided or spray-guided injection systems exhibited higher particulate emissions compared to PFI vehicles [22]. Recently, Zhu et al. [23] noted that under extremely cold ambient conditions of -7°C , PFI vehicle emissions including carbon monoxide (CO), unburned hydrocarbons (HCs), and particulate mass were higher than with the GDI vehicle. At an ambient temperature of 30°C , the GDI vehicle emitted more pollutants. This result is in agreement with the aforementioned studies.

1.2 PRE-CHAMBER INITIATED COMBUSTION

Another technique to control combustion and extend lean flammability limits of lean-burn mixtures is divided chamber stratified charge or “pre-chamber” combustion initiation technique. Various pre-chamber-initiated combustion systems developed in the past are reviewed in [24]. A 2-stroke Ricardo Dolphin engine was built in the first part of the twentieth century. This engine had two valves for intake and exhaust and a third auxiliary valve, from which fuel-rich mixture entered a pre-chamber cavity [25]. The pre-chamber cavity was connected to a much larger-volume main chamber through an intermediary nozzle. A spark ignited this rich mixture in the pre-chamber, thereby burning a leaner main chamber mixture. A variant of this 3-valve engine was the torch cell engine design. Examples of this design were developed by several OEMs and were intended to eliminate auxiliary pre-chamber fueling [26-28]. During compression stroke, some of the main chamber charge entered the pre-chamber, wherein a spark created a turbulent torch that further ignited the remaining main chamber mixture. One of the mass-produced pre-chamber combustion engines was based on Honda’s compound vortex-controlled combustion (CVCC) system that was installed in a Honda Civic passenger car [29]. The CVCC engine incorporated a larger pre-chamber and a larger orifice nozzle. The flame torch from pre-chamber combustion

ignited the main chamber's swirl (vortex-induced) flow mixture through normal flame propagation behavior.

1.2.1 Swirl Chamber Spark Plugs

Several Tier-1 suppliers developed pre-chamber spark plug designs, and some of them are currently available as commercial products. A swirl chamber spark plug with 5 orifices (4 tangential and 1 central) was used to create 5 torch jets. These jets insured rapid and uniform energy conversion in the main combustion chamber [30]. During the compression stroke, the 4 tangential orifices generated significant swirl in the swirl chamber, and the spark reached the chamber walls rapidly and emanated rapid jets out of the orifices. In an advancement to this design, a novel swirl chamber spark plug was recently proposed for stationary gas engines whose center-to-ground electrode distance is adjustable [31]. The adjustable gap distance feature was intended to reduce manufacturing costs by minimal use of precious metals on the electrodes. A swirl chamber cap was attached to the combustion chamber end of the plug.

A different concept, called pre-chamber spark plug, was previously proposed for gaseous fuels such as natural gas. In this case, a small pre-chamber was attached, with or without orifice, to the end of spark plug during compression. The consequent flame jet aided in igniting the main chamber mixture [32, 33]. A novel high-performance pre-chamber spark plug was previously demonstrated to extend the lean limit of natural gas to an air/fuel equivalence ratio ($\lambda = \text{AFR}/\text{AFR}_{\text{stoichiometric}}$) equal to 2.0 in an open chamber engine [34].

1.2.2 Turbulent Jet Ignition

Jet ignition is a pre-chamber-initiated combustion design that was first introduced by the developer of the theory of chemical chain reactions, Nikolai Semenov [35, 36]. In jet ignition systems, a much smaller orifice connects a small pre-chamber combustion cavity to an engine-

cylinder main chamber. Gussak et al. determined that the highly chemically active species arising from incomplete combustion of a rich pre-chamber mixture produces fast, complete, and stable combustion of the main chamber mixture [37, 38]. Employing such a smaller orifice in jet ignition systems extinguishes the flame initiated in the pre-chamber, thereby creating active radicals that penetrate further downstream into the main chamber. As the flame breaks up into incompletely burned active radicals, several turbulent vortices are created, which carry these radicals at their centers in the main chamber. Thus the radical-charge admixing leads to fast and complete combustion of the main chamber mixture. This phenomenon was termed the torch-ignited 'LAG' (Lavinia Aktyvatsia Gorenia or Avalanche Activated Combustion) process. Pulsed jet combustion is a field of study led by Oppenheim and others [35, 39, 40] that focuses on the fluid dynamic features of the evolution of exothermic energy and its deposition on the turbulent combustion systems as seen during the LAG process. A first jet ignition engine was built based on the LAG process. Its suggested dimensions were: optimal pre-chamber size of 2-3% of the clearance volume, an orifice area of 0.03-0.04 cm² per 1 cm³ of pre-chamber volume and an orifice length-to-diameter ratio of 0.5 [38].

Turbulent jet ignition (TJI) is a further refinement of the jet ignition concept directly applicable to spark ignition engine designs. In a TJI design, the pre-chamber is connected to the main chamber using multiple smaller orifices. The pre-chamber housing carries a flush mounted spark plug and a pre-chamber fuel injector. This housing can be installed as a bolt-on addition by replacing the conventional spark plug in a modern engine design [41]. A spark-ignited reactive mixture in the pre-chamber flows through the nozzle orifices and results in multiple chemically active turbulent jets that emanate into the main chamber. These reacting jets provide spatially

distributed ignition sources (jet-to-jet as well as individual jet area) for the fuel-air mixture in the main chamber, thereby burning the mixture rapidly.

1.3 POTENTIAL IMPROVEMENTS IN GASOLINE-FUELED ENGINES

1.3.1 Thermal Efficiency

1.3.1.1 Production Engines

Most of the global focus in the development of light-duty vehicles is to improve the thermal efficiency of DISI gasoline engines and reduce exhaust emissions using various strategies such as high compression ratio, charge dilution, tumble enhancement, high ignition energy, and late intake valve closures (Miller/Atkinson cycles). According to a recent benchmarking study conducted by the US EPA, current production engines carry a brake thermal efficiency ranging from 30-35%. An exception to this was Mazda's 2.0L engine that showed a peak of 37%, for a brake MEP of 5-10 bar at 2000 rpm engine speed (see Figure 3 in [42]). On the other hand, Toyota developed a 1.3L Atkinson cycle gasoline engine with a compression ratio of 13.5 that is expected to deliver a brake efficiency of 38%. Toyota claims that this is the world's highest brake thermal efficiency for a mass-produced gasoline engine [43]. In another announcement, Toyota predicted that its engine for the next-generation Prius comes with a brake thermal efficiency of 40%. This efficiency would be made possible by extending the exhaust gas recirculation (EGR) limit from 21% (current) to 28% using improved tumble-inducing intake ports, thereby increasing the combustion speed [44]. Recently, a Mahle's turbulent jet ignition engine has been incorporated in a Scuderia Ferrari racing car that is believed to offer an indicated thermal efficiency of up to 45% [45]. Reese [46] made a "propulsion system efficiency" analysis based on 2015 US EPA certification data to estimate the net improvements required in the engine, transmission, and driveline efficiencies to meet US 2025 GHG regulations. According to this analysis, a further 30% reduction in fuel

consumption is required for gasoline engines if all this improvement is to originate solely from engine development [46, 47]. If a thermal efficiency of 35% is considered as the current industry standard, this analysis would indicate a brake thermal efficiency of 50% ($=35/0.7$) to meet the 2025 regulations.

1.3.1.2 Single-Cylinder Research Engines

Single-cylinder engine research is being pursued by several groups to improve engine efficiency using different combustion technologies that are motivated by the benefits of HCCI or diesel combustion. Homogeneous charge compression ignition (HCCI) has been appreciated for its exceptional performance of reduced fuel consumption, soot, NO_x , and high mean effective pressures (with boosted intake) compared to the conventional spark ignition approach [48-50]. However, the major issues with this technique are the uncertainty in combustion phasing, high pressure rise rates, limited operating range, and high engine-out HC and CO emissions [51-53]. Gasoline premixed charge compression ignition (PCCI) has been majorly demonstrated in heavy duty research engines [54-56]. The main idea of this combustion technology is to inject gasoline at high pressures in a compression ignition engine during early compression stroke, leading to a more homogeneous charge mixing. Due to its high resistance to ignition compared to diesel, gasoline combustion is started after the end of injection, thereby resulting in low stratification. With an EGR $\sim 50\%$ ($\lambda=1.4$) and highly boosted intake, operating conditions were identified for a heavy duty engine using gasoline partially premixed compression ignition with a remarkable indicated efficiency of approximately 53.5% across a load range of 5-26 bar IMEP [57]. Reactivity-controlled compression ignition (RCCI) is a variant technique of PCCI in which a low-reactivity fuel such as gasoline is premixed via port fuel injection, while a relatively small mass of diesel is injected into the cylinder during compression stroke. The gradient of fuel reactivity thus

created from in-cylinder blending aids in a broad combustion event and reduced pressure rise rate. Inagaki et al. [58] used the RCCI technique (or dual-fuel PCCI) to attain indicated efficiency values greater than 50% for IMEP values greater than 9 bar by employing a compression ratio of 14.0 and supercharged intake. Other works that utilized RCCI to investigate potential improvements in the efficiency and exhaust emissions of heavy duty and or light duty engines are described in [59, 60] and references therein. Spark-assisted compression ignition (SACI) is another technique inspired by HCCI, where the spark ignition consumes a part of the fuel/air mixture and the heat thus released assists in auto-igniting the remaining charge earlier than with the HCCI process [61, 62]. In this way, the slowly propagating flame (compared to autoignition) moderates the heat release rates and the ringing effect seen during autoignition in HCCI.

1.3.2 Emissions Control

According to the vehicular emission regulations for light duty vehicles as reviewed by Johnson [63], a 75% reduction in fleet average non-methane organic gases (NMOG) and NO_x will be phased in from 2015 to 2025. By 2025, the target NMOG+NO_x will be 30 mg/mile for both cars and light-duty trucks. Another targeted criteria emission is the particulate mass (PM). The PM standard will undergo a rigorous reduction of 90% from the current 10 mg/mile down to 1 mg/mile in 2025. These targets should be achieved using a combination of better-quality combustion and economically feasible exhaust aftertreatment systems. To develop more efficient and cleaner combustion techniques, it will be helpful to begin with an understanding of the working standards of aftertreatment systems, as follows.

1.3.2.1 Evaluation of Exhaust Aftertreatment Systems

Exhaust aftertreatment systems are by default employed in every automobile released in the market. These systems are used to convert toxic pollutants, a result of non-ideal combustion

(incomplete burn and/or excess air), to mildly toxic (excess CO₂) or inert end products. Among the aftertreatment systems available, the three-way catalyst (TWC) has been most widely used, is a cheaper alternative, and requires less complicated feedback systems. The TWC is a multi-functional catalyst that can (i) oxidize CO and HC to CO₂, and (ii) reduce NO_x to N₂ and H₂O, with near-stoichiometric exhaust gas composition [64]. The catalyst needs to attain a “light-off temperature” before it can undergo these chemical reactions. This implies that during engine startup, when the exhaust pipe is cold, emissions (mainly HC) are released to the atmosphere without conversion [65]. In the older TWC systems, only underfloor catalysts were employed. In modern TWC systems, the catalyst is mounted next to the exhaust manifold to minimize heat losses and hence termed as close-coupled TWC; an additional underfloor catalyst would be employed in some vehicles. Based on efficiency requirements discussed earlier, the vital importance of reducing fuel consumption is evident to reach the mobility targets for 2025. Such an engine operation under excess air or the “lean-burn” mode would result in lower exhaust gas temperatures. A traditional TWC has a sufficient oxidation efficiency for CO and HC but poor reduction efficiency for NO_x under lean-operation [66]. This limitation in the TWC shifted the attention to the lean-NO_x traps/NO_x storage catalyst and selective catalytic reduction (SCR) systems. During lean burn operation, the NO_x storage catalyst chemically stores the oncoming NO_x compounds in the form of nitrites and nitrates on an alkali metal. These stored compounds are converted later when the engine management system switches briefly to fuel-rich operation. In SCR, the NO_x is reduced to N₂ using a selected reducing agent or reductant such as ammonia or urea. Although ammonia is a well-established reductant in stationary applications such as in power plants, urea is the preferred reductant due to its negligible toxicity and vapor pressure [67]. A distinctive feature of SCR compared to TWC is that the former works optimally even at exhaust temperatures lower

than 250°C which is close to the light-off temperature of TWC [68, 69]. Overall, both NO_x storage catalyst and SCR are expensive and add significant complexity to a vehicle [70].

1.3.2.2 Diluted Lean Combustion

Based on the above discussion, it is clear that employing a close-coupled three-way catalyst is the preferred aftertreatment system. Recall that the TWC has an optimal conversion efficiency under near-stoichiometric conditions. On the other hand, reducing fuel consumption is the best way to achieve efficiency targets and CO₂ emissions. An ideal solution for both goals is to improve combustion technologies by employing exhaust gas recirculation. By using EGR, both the fuel and intake O₂ mass fraction can be reduced, thereby resulting in near-stoichiometric conditions. Controlling the amount of intake O₂ without throttling further promotes the part-load efficiency due to reduced pumping losses.

NO_x is a mixture of nitric oxide (NO) and nitrogen dioxide (NO₂), and other minor concentrations of nitrogen oxides. Thermal NO_x, described by the Zeldovich mechanism, is a major source of NO_x formation in engine applications and is created when combustion temperatures reach higher than 1800 K. Prompt NO_x mechanism is another source of NO_x possibly formed during combustion in low-temperature, fuel-rich conditions [71]. Lean-mixture combustion with EGR dilution (or diluted lean combustion) has received significant attention in the past few decades because of its reduced peak combustion temperatures and thus NO_x formation. The EGR dilution is especially advantageous under mid-to-high load operating conditions. Francqueville and Michel [72] observed that EGR addition mitigated knock occurrence at a speed/load of 2000 rpm/19 bar IMEP. Lattimore et al. [73] observed that by adding 12% EGR, fuel consumption decreased by 4.1% at 1500 rpm/9.5 bar IMEP.

One problem with using EGR is the aggravation of combustion instabilities. By replacing O_2 with N_2 or residual gases of combustion, the spark-ignited charge propagates at a slow rate. The slow flame speeds would result in significantly delayed combustion initiation and combustion phasing, and longer burn durations. This effect is more impactful at low speeds/loads because of the low in-cylinder pressures and temperatures which further delays the combustion process [74]. Park et al. [16] found that the NO_x formation was lowered by 45% using EGR under a 2000 rpm/2.8 bar IMEP operating condition. However, more fuel had to be injected to compensate for combustion fluctuations. It was interpreted that the delayed peak heat release rate observed with EGR could be the reason behind reduced NO_x .

Particulate matter (PM) from engine combustion is a combination of accumulation mode particles and nucleation mode particles. Accumulation mode particles include solid carbon particles (soot), and organic compounds such as sulphates and polycyclic aromatic hydrocarbons. The geometric mean diameter of the accumulation mode particles is greater than 30 nm. Nucleation mode particles (<30 nm) are inorganic compounds (e.g. SO_2 , NO_2 , and H_2SO_4) that are adsorbed and condensed on the solid particles [23, 75]. Traditionally, particulates were quantified by measuring the particulate mass using gravimetric or optical techniques [76]. The filter-based gravimetric technique was demonstrated to result in measurement errors, high variability, and inadequate sensitivity to the exhaust conditions seen with the modern low-emission vehicles [77]. To address this issue, a “Particulate Measurement Programme” was initiated by the United Nations’ UN-GRPE with the introduction of EURO 6. A major outcome of this program was to regulate particulate emissions by measuring PM using more accurate measurement techniques as well as by measuring particulate number (PN). Details of this program’s regulations and methods to obtain PN measurements can be found in [78]. Two current state-of-the-art instruments are

electrical low-pressure impactor for measuring total PN concentrations, and the condensation particle counter or solid particle sampling system for solid PN concentrations. As discussed in Section 1.2, GDI engines emit significantly higher particulates than the PFI engines during engine start-up period. During start up and aggressive vehicle acceleration, a GDI engine emits higher particulate number emissions compared to a diesel engine equipped with particulate filter [75].

The major determining factors for particulates formation are the amount of film deposition, wall-wetting and mixture formation [79-81]. Piston temperature, fuel injection settings, and in-cylinder air flow play crucial roles in these phenomena. The effect of EGR on soot and other particulate formation depends on several factors such as engine speed, load, operating conditions, and the thermodynamics of EGR used. Manente et al. [82] observed an increase in soot production with the EGR% at low speed (<1400 rpm) and 16-18 bar IMEP. The constant level of mixture stratification for different EGR amounts and reduced combustion temperatures were attributed to the higher soot observed there. Hedge et al. [83] compared the soot mass and PN measurements for a GDI engine with internal EGR (valve event overlap) and cooled external EGR dilution systems. They noted that cooled external EGR reduced the brake-specific soot mass (mg/kWh) by more than 60% and solid PN (#/kWh) by at least 40% for 2000-3000 rpm speed and 6.7-16.0 bar BMEP. At light load operation (2.0 bar BMEP), however, the particulate emissions were significantly higher using cooled external EGR compared to the hotter internal EGR. From similar results seen with internal EGR at low load, Piock et al. [84] interpreted that the higher in-cylinder mixture temperatures offered better fuel vaporization and reduced the PN emissions.

Studies have shown that NO_x reduction and stable combustion can be attained simultaneously when EGR is implemented along with other combustion-enhancing strategies [85, 86]. Diana et al. [87] noted that the benefits of higher compression ratio and improved part-load

efficiency can be attained by employing EGR (this reduces NO_x and mitigates knocking); along with enhanced in-cylinder flow, in harmony with the recent developmental strategies of Toyota engines. The lean and EGR dilution limits might be extended using advanced ignition systems [88, 89]. Alternatively, turbulent jet ignition has been demonstrated to ignite leaner mixtures and extend flammability limits beyond those obtained using spark ignition combustion. Vaporized gasoline was used as the pre-chamber fuel, and the engine was operated successfully at $\lambda > 2.1$ with minimal NO_x emissions [90]. A supersonic hot jet was created by using a converging-diverging, nozzle-ignited, ultra-lean H₂/air mixture (equivalence ratio 0.22) in a dual-chamber design [91]. However, combustion instabilities occurred near the lean-limit conditions. Turbulent jet ignition with gasoline in the main chamber and gaseous propane in the pre-chamber was demonstrated to maintain stable combustion with 50% more diluent mass (air and residual gases) than spark ignition combustion [41]. In another lean burn TJI study, using indolene in both chambers with a global $\lambda \cong 2.0$, the nozzle design was shown to influence jet velocity and penetration into the main chamber before creating ignition sites there [92].

Literature related to particulate formation in pre-chamber initiated gasoline combustion could not be found. Nevertheless, as most of the fuel (>95%) is injected into the main chamber through PFI injection, an engine equipped with the TJI technology is likely to have low particulate emissions (similar to PFI engine particulate emissions). Fujiwara et al. [93] noted that a part of the soot particulates (from diesel combustion) that entered the main chamber were burned up before leaving the exhaust. Also, soot oxidation occurred as long as the oxygen concentration in the main chamber was more than 5%.

1.4 CONTENTS OF THE PRESENT WORK

The current research work identified part-load unthrottled operating points for an advanced gasoline combustion engine that delivers an indicated efficiency of greater than 45% with high combustion stability. Different tasks involved in developing this engine are described as follows.

1.4.1 Dual-Mode Turbulent Jet Ignition

A patented Michigan State University concept dual-mode (DM) TJI engine was employed. It consists of a fuel injector as well as an additional air injector in the pre-chamber. The air injector is intended to (i) enhance the ignitability of injected fuel in the pre-chamber and (ii) purge out the residuals in the pre-chamber by injecting air during exhaust or intake stroke. The effects of pre-chamber air injection were investigated in a TJI-equipped rapid compression machine (RCM) using ultra-lean iso-octane/air mixture of global $\lambda \cong 3.0$. Mie-scattered iso-octane fuel spray images in the pre-chamber, ignition delay times (both pre-chamber and main chamber), burn durations (main chamber), and particulate formation were compared for different operating conditions in the RCM. The operating conditions that showed better results during RCM testing were chosen as the baseline conditions for further development of the DM-TJI optical engine of geometric compression ratio 9.5. Separate combustion visualizations were made for the engine's main chamber, fueled using a low-pressure injector and a high-pressure injector in the intake manifold. Using combustion visualizations of gasoline and in-cylinder pressure related data, a set of 1500 rpm and 6 bar IMEP operating points were determined that resulted in stable combustion for a global $\lambda \sim 2.1$ and showed a cleaner burning flame without luminous soot regions.

With the upcoming auto industry requirements of high efficiency and low emissions as the primary targets, MSU employed a DM-TJI engine with metal piston (and Bowditch extension) having a high geometric compression ratio of 12.0 in the next stage of this research. After

investigation of different fuel injection settings and spark timing sweeps, these experiments determined operating points for 1500 rpm and 6 bar IMEP that delivered an indicated thermal efficiency of $46.6\% \pm 1\%$ without EGR and an exhaust $\lambda \cong 1.9$. The above lean burn points were enriched to near-stoichiometric mixture while diluting with N_2 simulated EGR. In the end, operating points for 1200 rpm/1500 rpm and 7.6 bar IMEP were found that delivered an indicated thermal efficiency of $46.1\% \pm 1\%$ and an exhaust $O_2 \cong 0.5\%$. Such low non-zero exhaust O_2 could indicate that almost all the fuel is burned up for work output, while any unburned hydrocarbons are oxidized before leaving the exhaust manifold.

Having an additional air injector calls for more controls and/or optimization efforts. To this effect, work is underway in developing an alternative design for air supply to the pre-chamber. A numerical analysis was made, attached in the *Appendix*, to determine the geometrical requirements for this design as well as to estimate the work input required to operate this design.

CHAPTER 2

Effect of Pre-chamber Air and Fuel Injection on Iso-octane Combustion in Turbulent Jet Ignition Mode

2.1 SYNOPSIS

In the current work, ignition delay times and combustion behavior of jet-ignited iso-octane/air mixture were compared for different operating conditions using an optically accessible RCM. Optical access to the pre-chamber was obtained using a borescope and high speed camera setup. These operating conditions included different pre-chamber fuel injection timings based on the pre-chamber pressure at the start of injection. The effect on combustion of having pre-chamber air injection, as seen in the dual mode TJI (DM-TJI) system, was studied by comparing the results obtained with and without having an air injection in the pre-chamber. In addition, different air injection pressures were tested for a given air/fuel injection timing.

2.2 EXPERIMENTAL SETUP: DM-TJI CHARACTERIZATION USING A RAPID COMPRESSION MACHINE

Lean-burn investigations of iso-octane were completed in an optically accessible rapid compression machine, shown in **Figure 2.1**. A detailed description of this RCM's design and operation was included in [94, 95]. The single-stroke RCM uses the mechanical stroke of a flat-top piston (without crevice) to compress an air/fuel mixture rapidly to engine-relevant temperatures and pressures. The hydraulic reservoir was pressurized by pumping hydraulic fluid into it. This fluid offered the holding pressure while the fuel-air charge was allowed to mix well and prevented the coupled pneumatic-hydraulic piston from moving. The pneumatic piston was activated using compressed air and was used to drive the hydraulic piston which in turn moved the combustion cylinder piston, resulting in the RCM compression stroke. There is no expansion

stroke and thus the piston remains at top dead center (TDC) position at the end of compression stroke. A Kistler type 6117BFD17 spark plug and pressure sensor combination was used to record pre-chamber pressure data. A piezoelectric pressure transducer (Kistler type 6125C) placed at the bottom of the combustion chamber was used to record main chamber pressure data. All input signals used to control injection timings, durations, and spark timing as well as pressure data output were managed using LabVIEW software. Iso-octane was used for fueling both pre-chamber and main chamber. Before performing each combustion experiment, the chambers were evacuated using a vacuum pump. By following this approach, any film buildup on the wall during fuel delivery to the main chamber would be difficult to clean up and such improper purging can have a strong influence on the subsequent combustion experiment. This undesirable possibility was moderated by using an initial cylinder wall temperature of 120°C (or 393.15 K) which is greater than the boiling point of iso-octane, 372.4 K \pm 0.2 K [96]. The chamber temperature was controlled using electrical band heaters that are wrapped with high-temperature insulation and wall-embedded thermocouples. The LabVIEW program maintained the chamber at a constant temperature using feedback from wall-embedded thermocouples.

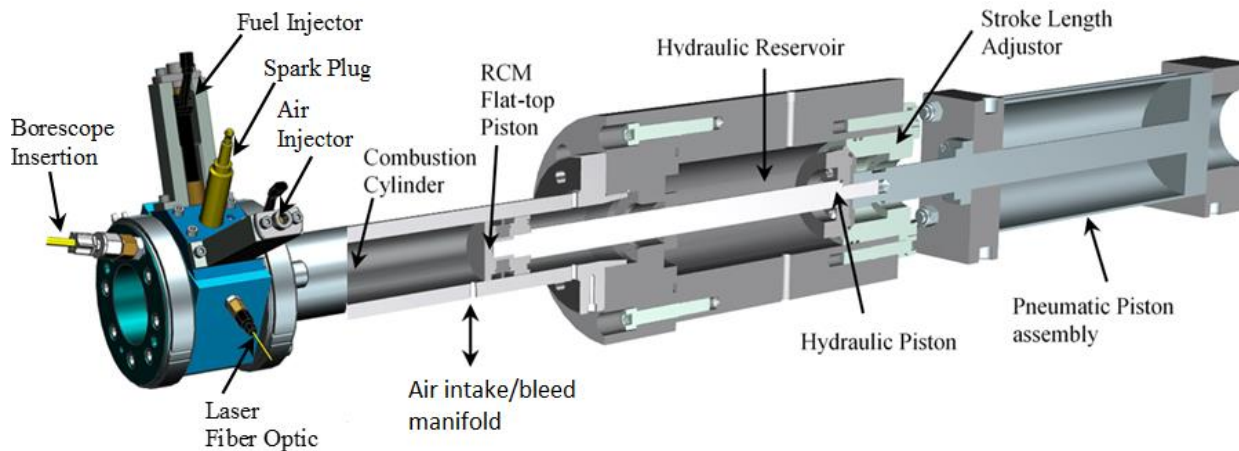


Figure 2.1: Optically accessible rapid compression machine incorporated with the pre-chamber fuel and air injection TJI design.

A notable difference between a TJI-based engine and a TJI-based RCM operation is the way fuel is delivered to the main chamber. In a TJI engine configuration, the fuel is delivered to the main chamber through port-fuel injection using a second injector installed in the intake port. In the RCM, this homogeneous main chamber fueling was replicated by initially injecting multiple pulses of fuel from the same injector installed in the pre-chamber, followed by supplying air through the intake manifold. When the total pressure measured at the intake manifold reached 1.04 bar, the manifold valve was closed and the fuel and air were allowed to mix for a certain time period. It was verified that a time period of 3 mins gave similar pressure plots and showed similar combustion behavior to those obtained with a wait time of 10 mins, and hence the former time period was chosen here. Three minutes after the manifold valve was closed, the pre-chamber fuel injection and/or air injection occurred during compression stroke. The fuel injection pressure was 100 bar for both pre-chamber and main chamber injections. The spark event occurred 6 ms after the piston reached the TDC position. The main chamber fuel injection specifications along with spark timing are included in **Table 2.1**. The mass of fuel injected for a given pulse width was determined based on fuel injector calibrations done separately. From this calibrated data, the pre-chamber λ value was approximately equal to 1.40 and the global λ was about 3.00.

Table 2.1: Specifications of TJI-equipped RCM Apparatus

Cylinder Wall Temperature	393.15 K
Compression Ratio	11.2
Main Chamber Diameter	50.75 mm
Piston Stroke Length	254 mm
Clearance Volume	50.63 cm ³
Pressure at Compression TDC	20.76 bar
Pre-chamber Volume	2.51 cm ³

Table 2.1 (cont'd)

Nozzle Orifice Size (Length x Diameter)	Two orifices 3 mm x 2.185 mm
Fuel for Both Chambers	Iso-octane
Fuel Injection Pressure	100 bar
Air/Fuel Equivalence Ratio	
Pre-chamber	$\lambda_{pre-chamber} \approx 1.40$
Combined	$\lambda_{global} \cong 3.02 \pm 0.11$
Spark Plug with Pressure Sensor	Kistler 6117BFD17
Spark Dwell	5 ms

2.2.1 Fuel Spray and Combustion Visualizations

2.2.1.1 Pre-chamber

Liquid droplets illuminated with a wavelength of light smaller than the droplet diameter undergo elastic scattering of light, known as Mie-scattering. Mie images of fuel were recorded to capture the fuel spray event in the pre-chamber. A 20 W Copper (Cu)-Vapor laser beam with a 25 ns pulse was directed to the pre-chamber using a 1 mm diameter fiber optic cable. The laser beam, emitted at wavelengths of 510.6 nm (green) and 578.2 nm (yellow), flood-illuminated the pre-chamber after the laser beam passed through a 4 mm quartz window. The pre-chamber fuel spray event was recorded while the laser was on. Optical access to the pre-chamber was attained by inserting a borescope along a machined hole in the pre-chamber. The borescope used was a Karl Storz rigid borescope with a viewing angle of 0° , field angle of 67° , outer diameter of 7 mm, and working length of 330 mm. **Figure 2.2** shows a closer view of the dual mode TJI setup in the RCM, highlighting the locations of the fuel and air injectors, spark plug, and fiber optic for spray illumination. The borescope was positioned orthogonal to this view (normal to the image in **Figure 2.2**), which implies that all the fuel spray images presented in this work follow the same locations

of different components as seen in **Figure 2.2**. The borescope was attached to a PHOTRON high-speed monochrome video camera. Recordings were acquired at an imaging frame rate of 10000 frames/sec. Laser pulse timing was controlled by the camera trigger, which was provided by a 5V transistor-transistor logic (TTL) pulse using LabVIEW program. The camera timing was originally synchronized with the commanded start of fuel injection. However, the fuel spray images consistently showed that the spray plume was first seen to enter the pre-chamber at 0.5 ms after start of injection (aSOI). This delay could be explained by the mechanical response of the fuel rail-injection system or by random noise introduced from the laser pulsing. Nevertheless, this factor did not affect the observations made here and the first frame was assumed to be at 0.5 ms aSOI for all operating conditions. It should be noted that the images presented here are two-dimensional representations of the three-dimensional spray development inside the chamber.

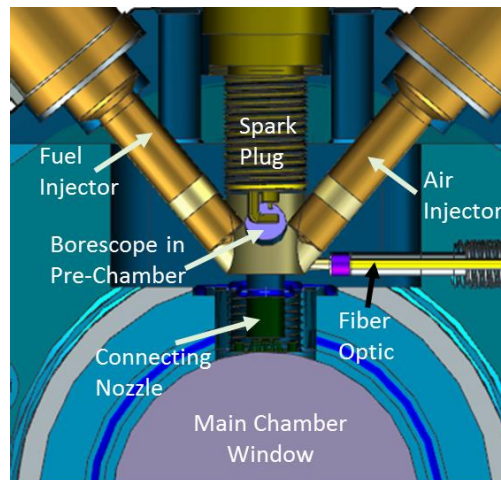


Figure 2.2: Close-up view of the TJI setting installed in the RCM.

2.2.1.2 Main Chamber

Main chamber visualizations were recorded looking through a 50.75 mm diameter sapphire window installed onto the combustion chamber (see **Figure 2.2**). Recordings of less-luminous combustion due to lean conditions were completed using a PHOTRON SA4 high-speed color

video camera and Nikon 50 mm f/1.2 objective lens at an imaging frame rate of 4500 frames/sec. These recordings were completed simultaneously with the pre-chamber recordings to identify visible correlations between fuel spray behavior in the pre-chamber and the resulting combustion in the main chamber.

Particulate content was used here as a metric to evaluate the combustion behavior. Natural luminosity of soot in the visible wavelengths has been shown to be orders of magnitude higher than the chemiluminescence of combustion gases [97]. This property was used to characterize soot and was extended to identify particulate content as a whole. A pixel threshold approach was employed wherein the pixels of the true color image whose red values exceeded a chosen threshold were considered to be occupied by particulates. The pixels with intensities below this threshold were filtered to zero values. **Figure 2.3** illustrates this pixel threshold approach. For better comparison, a “particulate index” was included that indicates the number of particulate-representative pixels in the filtered image. The filtered image is 270x270 pixels which corresponds to a resolution of approximately 5.3 pixels/mm.

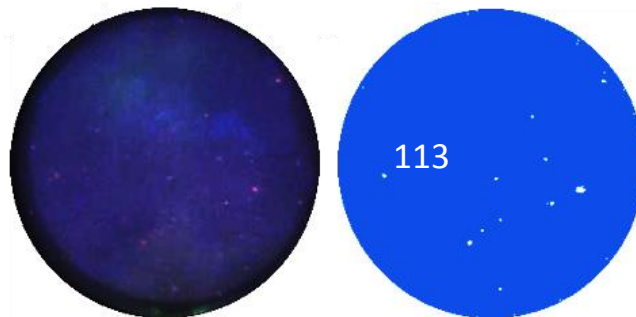


Figure 2.3: Raw image during main chamber combustion (left) and corresponding filtered image showing the particulate index (right).

2.2.2 Operating Conditions

After observing promising results with the DM-TJI concept in the engine [98], the concept was further investigated in this study to elucidate the physics of DM-TJI. The RCM was operated

under different working conditions as listed in the test matrix, **Table 2.2**. The RCM operation is a time-based event, unlike an engine stroke, which is a crank-angle based event. In both setups, however, the piston position is designated with respect to the top dead center (TDC) position. The pre-chamber mixture undergoes a non-linear polytropic compression process. Hence, instead of selecting the operating conditions on a time basis, a wide variation in pre-chamber fuel injection timing was studied here by choosing different injection times with respect to the pre-chamber pressure (P_{PC}). The work conducted is summarized in **Table 2.2**. Three injection conditions were chosen: a) where the pre-chamber pressure at the start of injection (SOI) was 3 bar – early fuel injection (EFI); b) 10 bar – middle fuel injection (MFI) and c) 18 bar – later fuel injection (LFI). All the experiments done in this work involved only one fuel injection pulse, with a pulse width of 0.75 ms. In the RCM, a set of fuel injection experiments were conducted without pre-chamber air injection (test #1 to #3).

These operating conditions were then repeated while including air injection (tests #4 to #6) in the pre-chamber. Injecting air at different P_{PC} values changes the total air mass propelled into the pre-chamber, depending on the difference between the injection pressure and the chamber pressure. In order to maintain constant air mass flow, the air injection pressure was calibrated and then adjusted to compensate for the pressure differential (ΔP) in each condition. For example, air injected into the pre-chamber was set to an injection pressure of 300 psi when $P_{PC} \sim 10$ bar and 200 psi when $P_{PC} \sim 3$ bar. In this way, the additional 100 psi (approximately 7 bar) injection pressure was considered for the middle fuel injection timing to match the amount of air mass injected with 200 psi injection pressure for the early fuel injection timing. In addition to air injection timing, three air injection pressures of 200 psi, 400 psi, and 800 psi were tested at $P_{PC} \sim 3$ bar. As the pre-chamber pressure was the same for these conditions, no pressure differential compensations were

made. The injector calibration data showed that the amount of air mass injected increased linearly with the air injection pressure. This implies that the air mass injected with 800 psi injection pressure was four times the mass injected with 200 psi injection pressure. When compared to total air supplied through the intake manifold, the additional air mass injected in the pre-chamber due to a difference in the air injection pressure (800 psi vs 200 psi) had negligible effect on the overall compression pressures (maximum pressure difference was 0.35% of peak pressure). All the experiments having air injection involved only one air injection pulse, with a pulse width of 0.95 ms and injection time of 0.2 ms before fuel SOI in the pre-chamber. A total of three repeated experimental runs was carried out for each data point reported. A representative pressure trace and/or burn durations close to the mean values was chosen for comparing different parameters of interest.

Table 2.2: Text Matrix for Fuel and/or Air Injection in the Pre-chamber

TEST NO:	PRE-CHAMBER AIR			PRE-CHAMBER FUEL	
	Pressure (psi)	Timing (ms b.Fuel)	Pulsewidth (ms)	Timing (ms)	Pulsewidth (ms)
#1 to #6	<i>Without Air and With Air</i> For Conditions with Air:- 200 + ΔP 0.2 0.95			@ P _{PC} =3 bar (EFI)	0.75
				@ P _{PC} =10 bar (MFI)	0.75
				@ P _{PC} =18 bar (LFI)	0.75
#7	400	0.2	0.95	@ P _{PC} =3 bar	0.75
#8	800	0.2	0.95	@ P _{PC} =3 bar	0.75

2.3 RESULTS AND DISCUSSION

2.3.1 Fuel Spray in the Pre-chamber: With and Without Air Injection

Figure 2.4 shows the pre-chamber fuel spray recordings for the three injection timings without air injection. Fuel was injected from left to right in these images, and laser reflections from the chamber wall were seen upstream of the fuel spray close to the injector tip. When compared to the early fuel injection condition, the higher chamber pressures seen during middle and later fuel injection conditions applied more initial resistance to spray penetration as highlighted on 0.5 ms aSOI images. Also, higher chamber pressures resulted in the descending order of spray penetration lengths observed with the three injection timings. In **Figure 2.4**, without air injection in the pre-chamber, the EFI condition caused impingement on the opposite wall and rebounded as highlighted at 1.1 ms aSOI. On the other hand, spray images during MFI and LFI conditions showed little evidence of wall impingement and/or scattered light from the rebounded fuel droplets. Such an absence of wall impingement indicates that the higher chamber pressure might have enhanced fuel vaporization. **Figure 2.5** shows the pre-chamber fuel spray recordings that included an air injection, air being injected from right to left in this imaging view. Due to pre-chamber air injection, the fuel spray was deflected towards the bottom as indicated in 0.7 ms and 1.1 ms aSOI images. Based on the fuel and air injection pressures, the turbulent flow inside the pre-chamber could carry some droplets to the nozzle and/or main chamber which were outside the borescope view. Comparing **Figure 2.4** and **Figure 2.5**, no major differences were directly evident in the fuel spray behavior with and without pre-chamber air injection for MFI and LFI conditions. The higher chamber pressures for later air/fuel injection appear to dampen the influence of the air injection at 200 psi (or 13.79 bar).

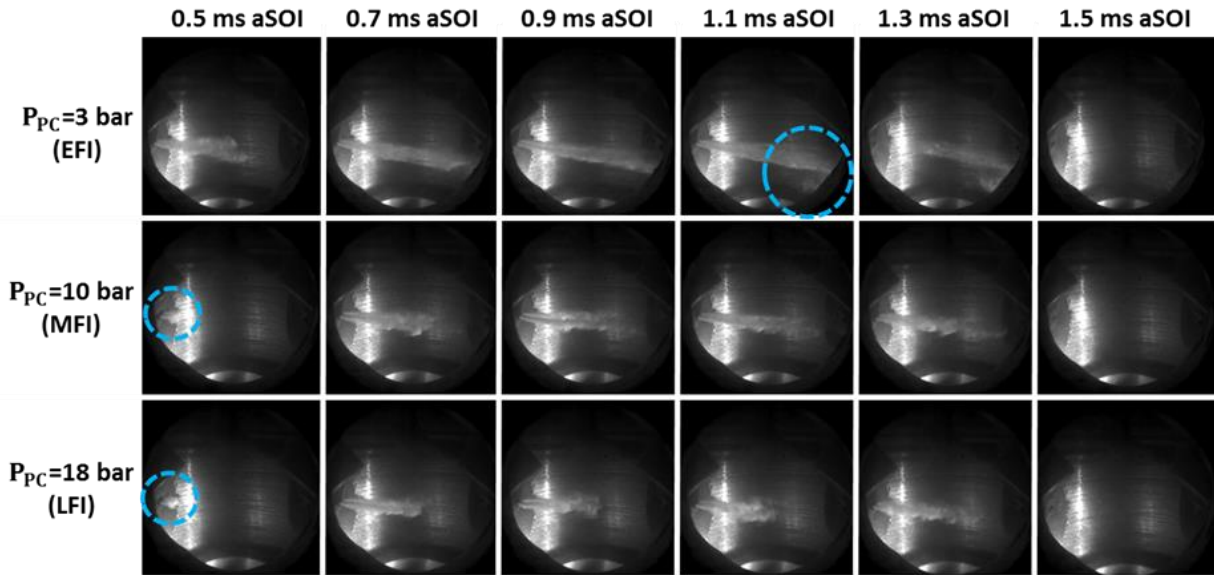


Figure 2.4: Instantaneous high-speed recordings of fuel spray event in the pre-chamber without pre-chamber air injection.

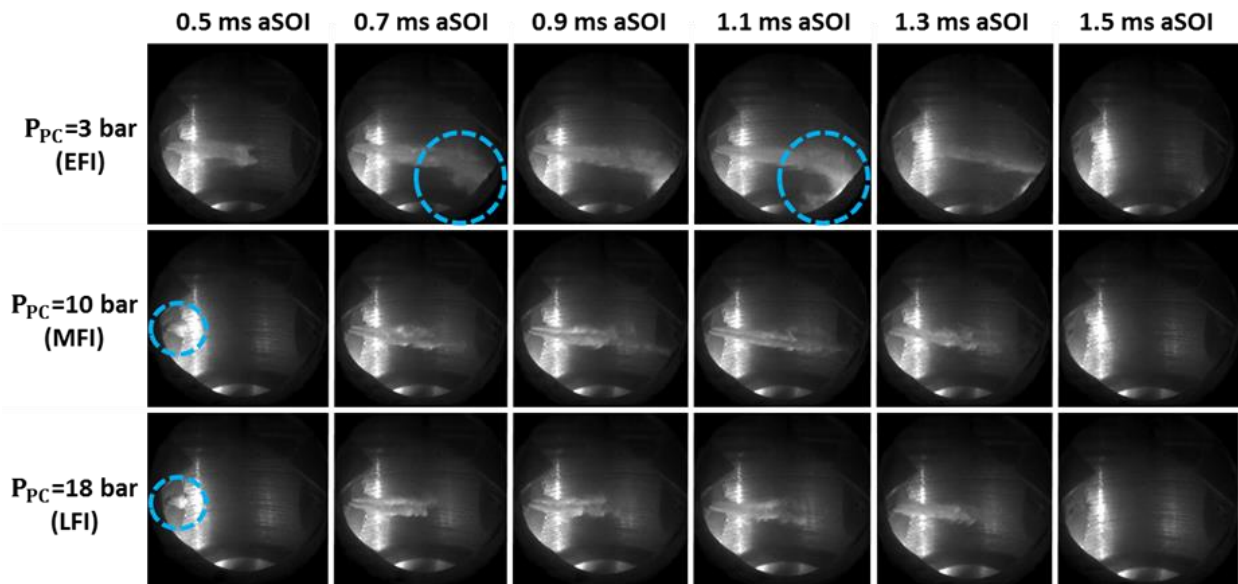


Figure 2.5: Instantaneous high-speed recordings of fuel spray event in the pre-chamber with pre-chamber air injection (200 psi).

2.3.2 Effect of Pre-chamber Fuel Injection Timing

Figure 2.6 shows the main chamber pressure plots for different fuel injection timings without pre-chamber air injection. The x-axis values were designated with respect to spark timing

(zero point). The fuel injection pulse signals at $P_{PC}=3$ bar, 10 bar, and 18 bar for the corresponding conditions are shown here as well. The pressure rise due to compression was similar for the three conditions. However, pressure rise due to combustion showed some differences among these conditions.

Ignition delay in the pre-chamber is defined as the duration between spark initiation (SPI) and the time when the pre-chamber pressure differential first reached about 20% of its maximum pressure differential (similar to the definition in [99]). The time from spark command to the 20% pressure differential point is shown here as the pre-chamber ignition time, PCI (in ms aSPI). Similarly, ignition delay in the main chamber was defined as the duration between PCI and the time when the main chamber pressure differential first reached approximately 20% of its maximum pressure differential. The time from PCI to the 20% pressure differential point is called here the main chamber ignition time (in ms after PCI). Note that the reactive mixture from pre-chamber combustion enters the main chamber through the connecting nozzle. With pre-chamber ignition time known, the main chamber ignition time indicates the time required for the reacting jet to ignite the lean mixture in the main chamber. **Table 2.3** lists the ignition times, based on the average of three repetition runs per case, in the pre-chamber and main chamber. Without air injection, pre-chamber ignition time was delayed with an advanced fuel injection timing condition. The presence of lower pre-chamber pressure and temperature was believed to delay ignition for the EFI condition. The LFI condition resulted in faster main chamber ignition. In **Figure 2.6**, during combustion, a second inflection point was observed for these and all other conditions in this work. This phenomenon was previously related to the end of the jet discharge event [100]. With the ignition source, i.e. jet discharge, ended, any unburned fuel can be transferred from the pre-

chamber into the hot main chamber volume, thereby resulting in a late secondary combustion event.

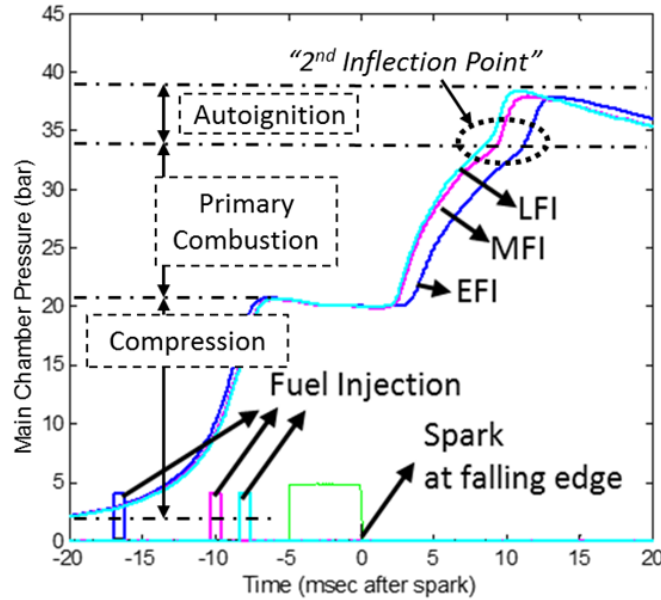


Figure 2.6: Details of main chamber pressure plots for different pre-chamber fuel injection timings (without pre-chamber air injection).

Table 2.3: Ignition Times for Different Fuel Timings With and Without Pre-chamber Air Injection

Fuel Injection Condition	WITHOUT AIR INJECTION		WITH AIR INJECTION	
	Pre-Chamber Ignition Time (ms aSPI)	Main Chamber Ignition Time (ms after PCI)	Pre-Chamber Ignition Time (ms aSPI)	Main Chamber Ignition Time (ms after PCI)
Early ($P_{PC} = 3$ bar)	2.60	0.74	2.11	0.85
Middle ($P_{PC} = 10$ bar)	1.64	0.73	1.68	0.79
Later ($P_{PC} = 18$ bar)	1.52	0.64	1.60	0.88

2.3.3 TJI-Initiated Combustion in the Main Chamber

Visible images captured during main chamber combustion without air injection are shown in **Figure 2.7**. Main chamber combustion images were recorded simultaneously with the pre-chamber fuel spray images. The green-yellow shade comes from Mie scattered Cu-vapor laser light used to illuminate pre-chamber fuel spray. Numbers on the upper left corner represent time duration (in ms) after spark. These images are arranged according to different visible reacting jet events that occurred during main chamber combustion. The first column shows the frames when the reacting jet was first seen to enter the main chamber. This event of jet entry was considered as the baseline time ($t_1=0$). As seen previously in **Table 2.3**, the pre-chamber mixture ignited faster with middle and later fuel injection conditions compared to early fuel injection condition. This is indicative of the more favorable conditions for ignition, wherein the high temperatures and pressures present at later pre-chamber fuel injection overcame the increased mixing time for early fuel injection. On correlating the pre-chamber ignition time (**Table 2.3**) and the main chamber jet entry time (**Figure 2.7**) for each condition, the duration between PCI and the jet entrance time was smaller for the LFI condition compared to MFI and was slightly longer compared to EFI condition. The pressure difference between pre-chamber and main chamber pressures was largest for the LFI condition. Faster burn rate and larger pressure difference between the two chambers result in higher jet exit velocities [101]. Hence, the fastest reacting-jet occurred with the later fuel injection condition. The second column in **Figure 2.7** shows the frames captured after 1.1 ms ($t_1=1.1+ \text{ms}$) during jet penetration where the jets coming out of the two-orifice nozzle reached close to or sheared the main chamber wall. The third column represents the images where the two jets mixed with each other. The time when the two jets met was the same for the three injection conditions, i.e. at $t_1=3.3+ \text{ms}$. This indicates that the speed of the reacting jet was similar in all the conditions

after entering the main chamber. This observation was also checked with the main chamber pressure curves that exhibited similar steepness during combustion for all the conditions.

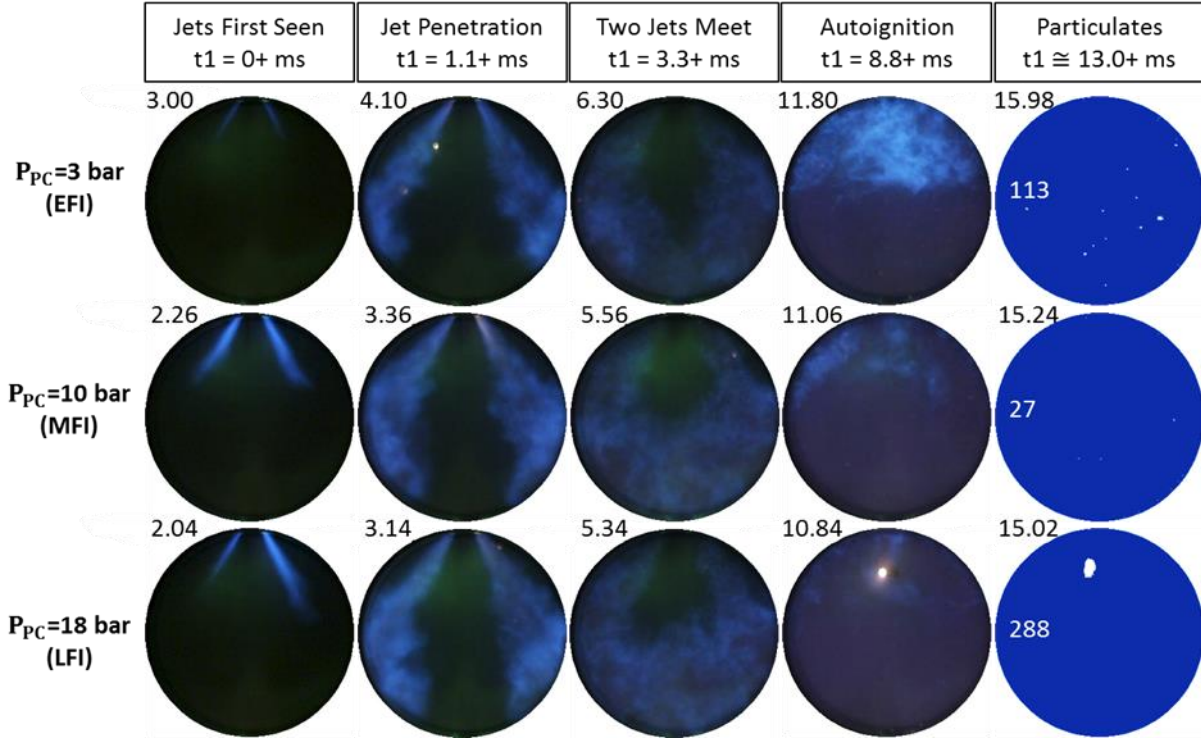


Figure 2.7: Instantaneous images of jet entry and combustion events in the main chamber for different fuel injection timings (without pre-chamber air injection).

As described earlier, a second combustion event, resembling sequential autoignition was observed in all the current experiments. Selected images during this autoignition event are shown in the fourth column (**Figure 2.7**). At $t_1=8.8+ \text{ ms}$, the autoignition event was at an early stage in the EFI condition. At this time, the MFI condition showed signs of autoignition completion while the LFI condition showed bright spot resembling particulates or burning droplet from autoignition. The images during autoignition showed discrete regions of reactions or reaction fronts in the upper-half of the main chamber, as also observed in [102] during lean burn iso-octane ignition. The pixel threshold-based images of particulate content are shown in the last column. The particulate index at $t_1 \cong 13.0+ \text{ ms}$ was highest with LFI, followed by EFI and MFI conditions in

that order. The main chamber ignited faster for LFI than in the other two injection conditions (see **Table 2.3**). Faster combustion could have further reduced the air-fuel mixing time in the main chamber, leading to rapid consumption of oxygen under the later fuel injection condition. In addition to this factor, the higher particulate content could also be attributed to locally fuel-rich burning caused by lower residence time in pre-chamber with the LFI condition, where fuel was injected about 2 ms later than during MFI condition.

2.3.4 DM-TJI Initiated Combustion in the Main Chamber

Air injection in the pre-chamber aided in igniting the pre-chamber mixture earlier for the EFI condition while the ignition time was delayed for LFI condition, compared to those without air injection in the pre-chamber (see **Table 2.3**). The main chamber ignition times for these conditions were delayed with air injection on. Main chamber events recorded with pre-chamber air injection are shown in **Figure 2.8**. The images are arranged in a similar fashion as seen before while discussing conditions without air injection. Although pre-chamber ignition was delayed with pre-chamber air injection under LFI condition, the jet appeared first in the main chamber with respect to PCI timing with LFI compared to EFI and MFI conditions (first column in **Figure 2.8**). The MFI condition showed a bright spot near the bottom of the chamber while the visible jet was still in the upper half of the chamber. In the third column, the time when the two jets met was almost same for MFI and LFI conditions and was delayed for the EFI condition. This indicates that the reacting jet speed was slower with the early fuel injection condition. A rough estimate of reacting jet speed ($\propto 1/\text{time}$) could be done by considering the relation,

$$\text{Reacting Jet Speed} \propto \frac{1}{\{(\text{Time when two jets meet}) - (\text{Pre-chamber ignition time})\}} \quad (2.1)$$

where the two jets are assumed to travel the same distance.

Using this relation, reacting jets with air injection in the pre-chamber are estimated to be faster by a factor of 1.3 (early-injection) and 1.4 (middle-injection) compared to those without air injection. The jet speed was unaffected with pre-chamber air injection for the LFI condition. At $t_1=8.8+$ ms, the autoignition event was on the verge of completion or already completed for all the conditions. As seen in the last column, the particulate index at $t_1 \cong 13.0+$ ms was highest with the later fuel injection condition, as noted previously for this condition without air injection. Delayed main chamber ignition times are identified as the primary reason behind reduced particulate index values with pre-chamber air injection, especially for early and later fuel injection conditions. Overall, an air injection pressure of 200 psi seemed to have little influence on mixture burning and particulate formation under the middle fuel injection condition, which had a pre-chamber pressure of 10 bar ($\cong 145$ psi).

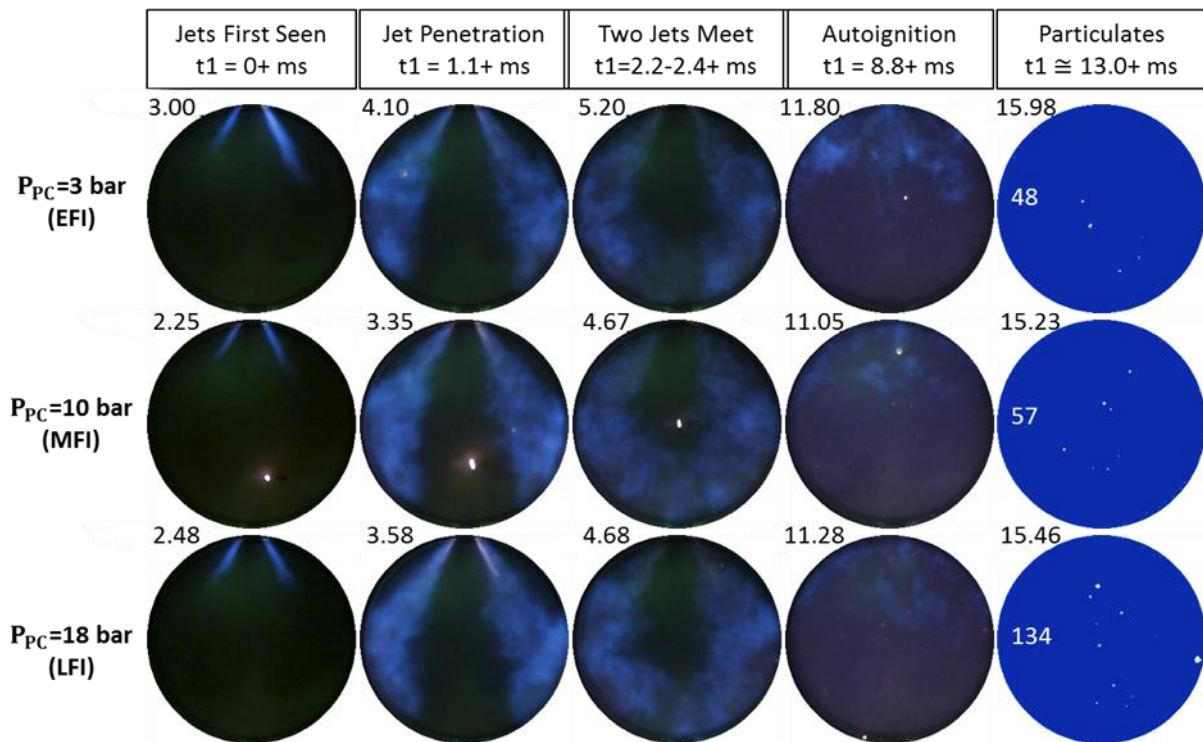


Figure 2.8: Instantaneous images of jet entry and combustion events in the main chamber for different fuel injection timings and with pre-chamber air injection (200 psi).

2.3.5 Effect of Pre-chamber Air Injection Pressure

In a companion set of experiments, three air injection pressures of 200 psi, 400 psi, and 800 psi were tested under the early fuel injection condition ($P_{PC} = 3$ bar). The 200 psi results were shown in **Figure 2.8** in the discussion of the effect of fuel injection timing with pre-chamber air injection on main chamber combustion. Also, results obtained without air injection in the pre-chamber are included here for a complete comparative study. **Figure 2.9** shows the high-speed images of fuel spray injected into the pre-chamber. At 0.5 ms aSOI, a small notch was seen at the head of the fuel spray for injection pressures of 200 psi and 400 psi while a smooth head was seen for 800 psi condition. As highlighted in images at 0.6 ms aSOI, a higher air injection pressure led to higher fuel-air mixing. Light scattered from the fuel spray continued to extend beyond the mean bulk fuel flow direction. The droplet clouds formed along the spray plumes are highlighted with arrows. These cloud structures were previously attributed to air entrainment and global spray-flow interactions that enhanced the droplet evaporation rate [103, 104]. Higher levels of droplet clouds were seen with the 800 psi condition, indicating enhanced spray break-up and improved evaporation processes occurred with this condition compared to others. At 1.3 ms aSOI, the 200 psi condition showed least light-scattering of droplets rebounded from the chamber wall.

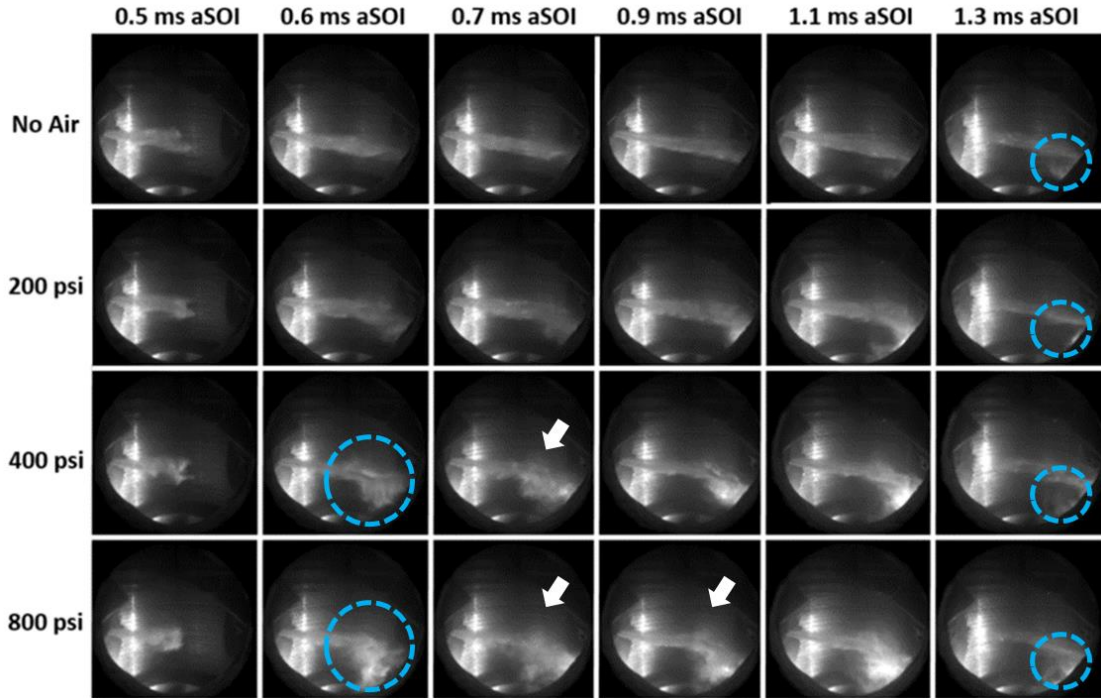


Figure 2.9: Instantaneous images of fuel spray event in the pre-chamber for different pre-chamber air injection pressures; pre-chamber fuel SOI was at $P_{PC}=3$ bar.

The pre-chamber and main chamber ignition times (average of three runs), along with the burn durations in the main chamber, are listed in **Table 2.4**. A higher air injection pressure resulted in longer ignition delay in the pre-chamber. All the air injection conditions resulted in equivalent ignition delay in the main chamber which was longer compared to without air injection.

Table 2.4: Ignition Times and Main Chamber Burn Durations for Different Air Injection Pressures

Air Injection Condition	Pre-chamber Ignition Time (ms aSPI)	Main Chamber Ignition Time (ms after PCI)	Burn Duration 10-90% (ms)
No Air	2.60	0.74	11.23
200 psi	2.11	0.85	10.30
400 psi	2.23	0.86	10.54
800 psi	2.70	0.87	11.63

Figure 2.10 shows the heat release rates (HRR) along with the photographic recordings of main chamber events for the set of pre-chamber air injection conditions shown in **Figure 2.9**. The HRR calculation was based on Heywood's model [105] while the heat loss terms are neglected for a simple analysis. It is to be noted that all these conditions had the same fuel injection timing and, where air was injected, the same air injection timing and injection duration. Also, recall that the numbers on the upper-left corner of the instantaneous images represent time duration (in ms) after spark initiation. Looking at the HRR plots on top, at 3 ms aSPI, the 400 psi air injection condition showed the highest HRR, closely followed by the 200 psi air injection condition. Accordingly, the jets were seen first with 400 psi and 200 psi conditions compared to others at 3 ms aSPI ($t_1=0$). At this time, the "no-air" condition showed a less penetrating, fainter jet indicating a less energetic jet. By the time $t_1=1.1+$ ms, the curves of both 200 psi and 400 psi conditions peak and then plummet. At this point, the rising curve of the no-air condition was close to its peak value. Accordingly, the jets in the no-air condition penetrated to the same extent as with the 200 psi condition. However, the jets in the 800 psi condition penetrated only halfway through the chamber.

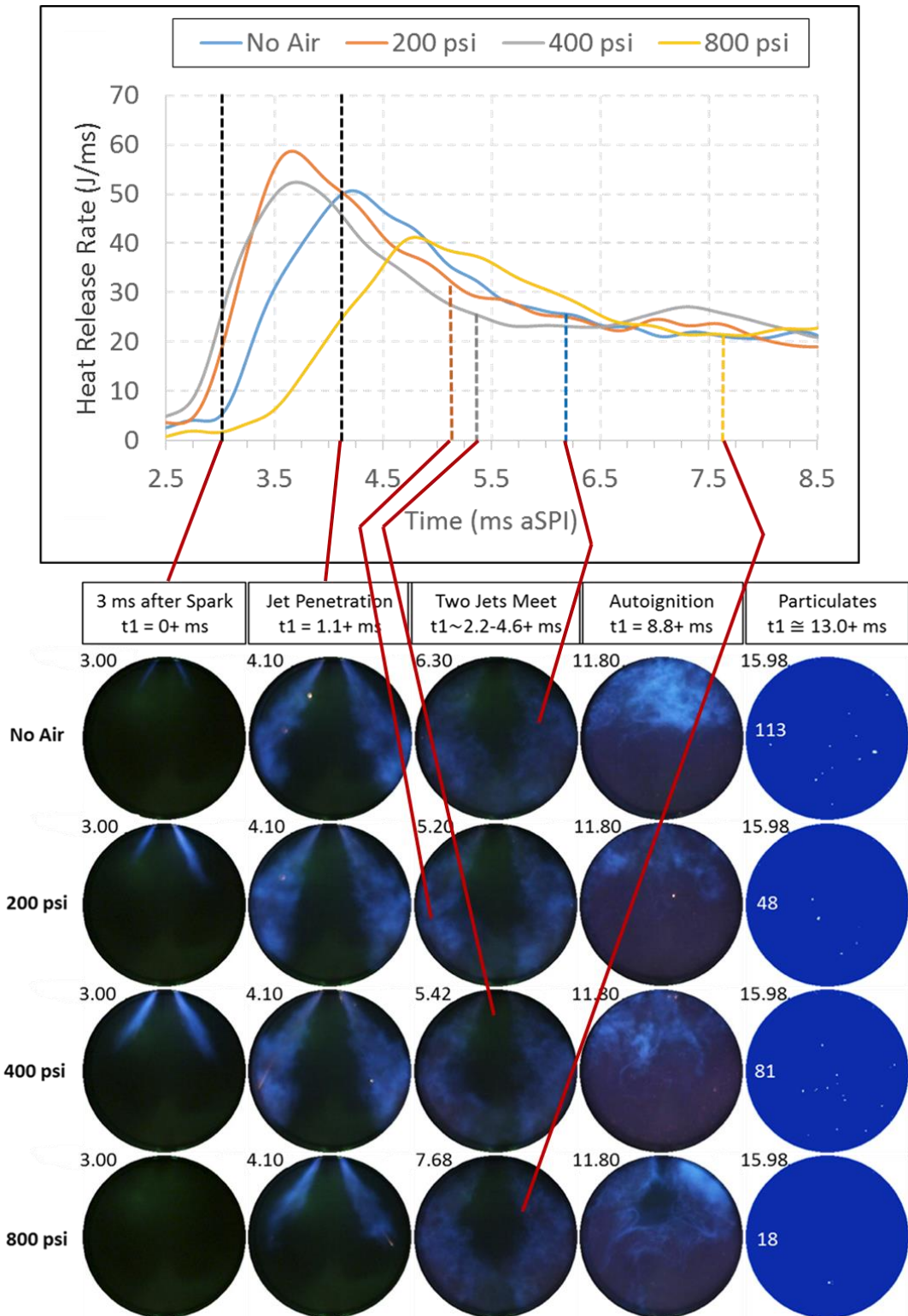


Figure 2.10: Jet entry and combustion events in the main chamber for different air injection pressures.

The point where the two visible jets mixed showed some differences among these conditions. The jets met earliest with 200 psi air injection and latest with 800 psi air injection since the point of spark initiation. The corresponding time stamps are highlighted with dashed lines in the HRR plots. It is interesting to see that the 200 psi condition released more heat by the time the two jets mixed compared to other conditions. From Equation 3.1, the reacting jet speed was calculated to be highest for 200 psi and lowest for 800 psi conditions. A faster jet combined with a higher heat release is attributed to the fastest 10-90% burn duration for the 200 psi condition as shown in **Table 2.4**. Following a similar trend of combustion, images at $t_1=8.8+$ ms show that the autoignition occurred first with 200 psi followed by 400 psi, no-air, and 800 psi condition in that order. The pixel threshold particulate images show that the 800 psi condition resulted in the smallest particulate index value among all the conditions tested in this work. This air injection condition showed the slowest combustion and least heat release during primary combustion in the main chamber. As previously mentioned, the competing factors of mixing, early pre-chamber reactions, and heat transfer are complex and require further analysis for sound interpretation. This most likely can be undertaken with a high-fidelity large eddy simulation applied directly to these experimental conditions.

To confirm the observations related to particulate formation, a normalized particulate index (NPI in %) was determined by dividing the particulate index values with the image area and multiplying with a factor of 100. These NPI values were plotted for different air injection conditions during combustion after the end of autoignition and are shown in **Figure 2.11**. Also, time-averaged values along this burn duration are exhibited in the curve on right. As shown here, both individual and average NPI values were lower for 800 psi and 200 psi air injection pressures. A common observation here and from the previous discussion on fuel injection timing is that a

longer main chamber ignition delay time formed the least number of particulates. In addition, the air injection pressure results showed that a longer ignition-to-10% burn duration in the main chamber reflected lower particulate formation. The 400 psi air injection pressure showed abnormally high NPI values. Although the combustion characteristics agree with the aforementioned observations regarding the ignition times, it is unclear why this injection condition showed exceptional ignition behavior.

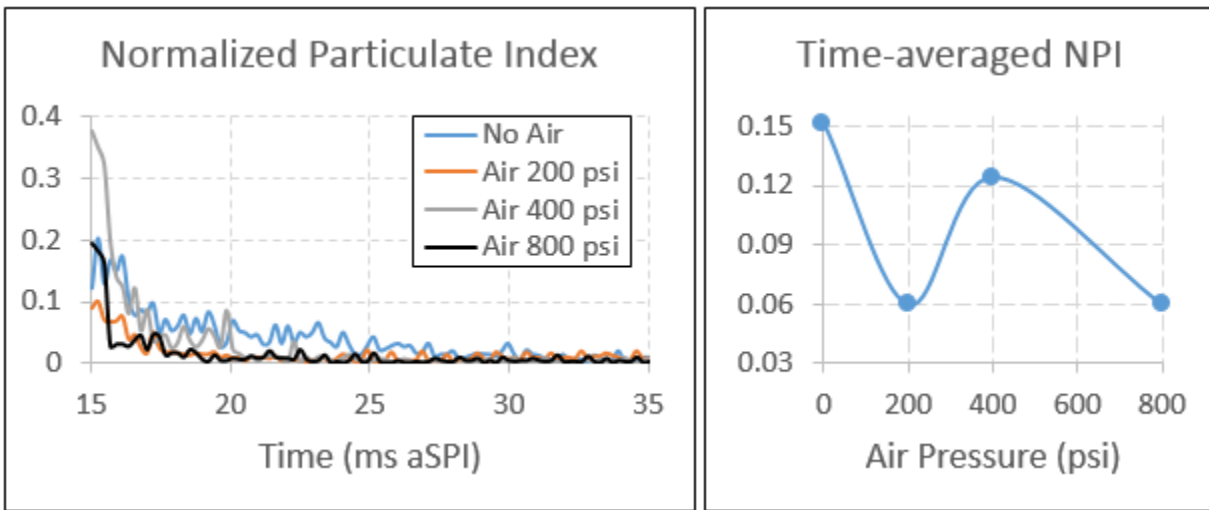


Figure 2.11: Normalized particulate indices for different air injection pressures.

2.4 SUMMARY

The effects of (i) pre-chamber fuel injection timing, (ii) including pre-chamber air injection of (iii) different air injection pressures on iso-octane/air combustion were studied in the TJI-equipped rapid compression machine for a global air/fuel equivalence ratio of 3.0.

- *Without air injection:* The middle and later fuel injection conditions showed less wall impingement, indicating that the higher chamber pressures might have enhanced fuel vaporization compared to the early fuel injection condition. In addition, the lower pre-chamber pressures and temperatures present at early fuel injection were believed to

delay the pre-chamber ignition. A faster reacting jet occurred with later fuel injection condition than with the other two fuel injection timings. The air/fuel mixture in the main chamber ignited and burned fastest with the later fuel injection condition.

- *With air injection:* Air injected at 200 psi pressure influenced the fuel spray more for the early fuel injection condition, while less jet damping occurred for the other two fuel injection timings where the pre-chamber pressures were higher than the air injection pressure. When compared to test conditions without air injection, pre-chamber air injection aided in quicker ignition for early fuel injection condition while the ignition timing was delayed for later fuel injection condition. Based on visual inspection, faster jets are expected for early and middle injection timings with the chosen pre-chamber air injection pressure.
- *With different air injection pressures:* A higher air injection pressure enhanced the spray break-up process and droplet evaporation rate. However, a higher air injection pressure resulted in longer ignition delay in the pre-chamber under the early injection condition. The additional air injected at 800 psi pressure, compared to 200 psi pressure, under the early injection condition could have resulted in local highly-lean regions in the pre-chamber thereby delaying ignition. The reacting jet speed was estimated to be significantly lower for an air injection pressure of 800 psi compared to other air injection pressures.
- At the end of jet discharge, autoignition occurred in the form of discrete regions of reactions or reaction fronts in the upper-half of the main chamber.
- Statistical analysis of particulate content showed that a longer main chamber ignition delay time and/or ignition-to-10% burn duration formed the least amount of

- particulates. Following this ignition behavior, the middle fuel injection condition without pre-chamber air injection resulted in fewer particulates than with the other two fuel injection timings. Similarly, an air injection pressure of 200 psi and 800 psi under the early fuel injection condition resulted in a lower particulate count. Higher particulate presence was attributed to (i) faster combustion, leading to rapid consumption of oxygen before the contents of the main chamber is properly mixed and (ii) lower pre-chamber residence time with the later fuel injection condition.
- For a fuel injection timing set at $P_{PC}=3$ bar, an air injection pressure of 200 psi is thus the favored choice for lean burn combustion. This air injection condition offered the fastest penetrating jet (reliable ignition source), relatively longer main chamber ignition time (avoiding particulate formation), and rapid 10-90% burn duration (increase indicated work and avoid accumulation mode particulate content or soot).

The current results would act as baseline conditions for engine testing where the continuous piston motion induces additional turbulence, and the inherent wave dynamics due to valve actuations would influence the pre-chamber and main chamber pressures.

CHAPTER 3

Visualizations and Efficiency Measurements of Liquid Gasoline Combustion in a Dual-Mode Turbulent Jet Ignition Optical Engine

3.1 SYNOPSIS

Selected operating conditions tested during RCM experiments were used as baseline points for the testing and development of dual-mode turbulent jet ignition (DM-TJI) optical engine. Both fuel and air injections were included in the pre-chamber. The main chamber was fueled using either a low-pressure injector or a high-pressure injector installed in the intake port. Combustion visualizations recorded while using the low-pressure injector indicated that this injector was not able to completely atomize the gasoline fuel and thus resulted in droplet burning regions. This finding was verified by comparing the combustion recordings of three different fueling approaches: 1) gasoline in both chambers; 2) gasoline in pre-chamber and gaseous methane in main chamber; 3) gasoline in main chamber and gaseous methane in pre-chamber. Hence, a high-pressure injector was employed for main chamber fueling in the subsequent experiments. With this high-pressure injector, operating conditions were identified at a global air/fuel equivalence ratio of ~ 2.1 and a speed/load of 1500 rpm/6 bar IMEP. With the developed operating points, the DM-TJI engine delivered an estimated indicated efficiency of 42% and showed high combustion stability, with no visible soot in the combustion recordings.

3.2 EXPERIMENTAL SETUP

3.2.1 Engine Operation

The DM-TJI optical engine was fired at engine speeds of 600 rpm, 1000 rpm, and 1500 rpm while all the discussions here pertain to 1500 rpm as this was the speed of interest. The engine consists of a flat head that was pre-heated by flowing coolant through the flow passages. The

coolant used was 50:50 ethylene-glycol water mixture that was heated to 90°C using an electrically-powered heating element. Using a PID (proportional-integral-differential) controller, the temperature was maintained at this set temperature during the entire testing time. Such an approach of pre-heating the head is usually employed for single-cylinder research engines to attain metal engine steady temperatures. A high-pressure fuel injector and a high-pressure air injector were inserted in the pre-chamber. For the main chamber, a low-pressure fuel injector as well as a high-pressure fuel injector were tested separately; the fuel injector was located in the intake port. **Figure 3.1** shows the DM-TJI optical engine (flat head) with the three major sections: pre-chamber, main chamber and the connecting orifice nozzle. Optical access to the engine's main chamber was provided by inserting a flat top sapphire window in the piston crown. Engine dimensions and other specifications are listed in **Table 3.1**.

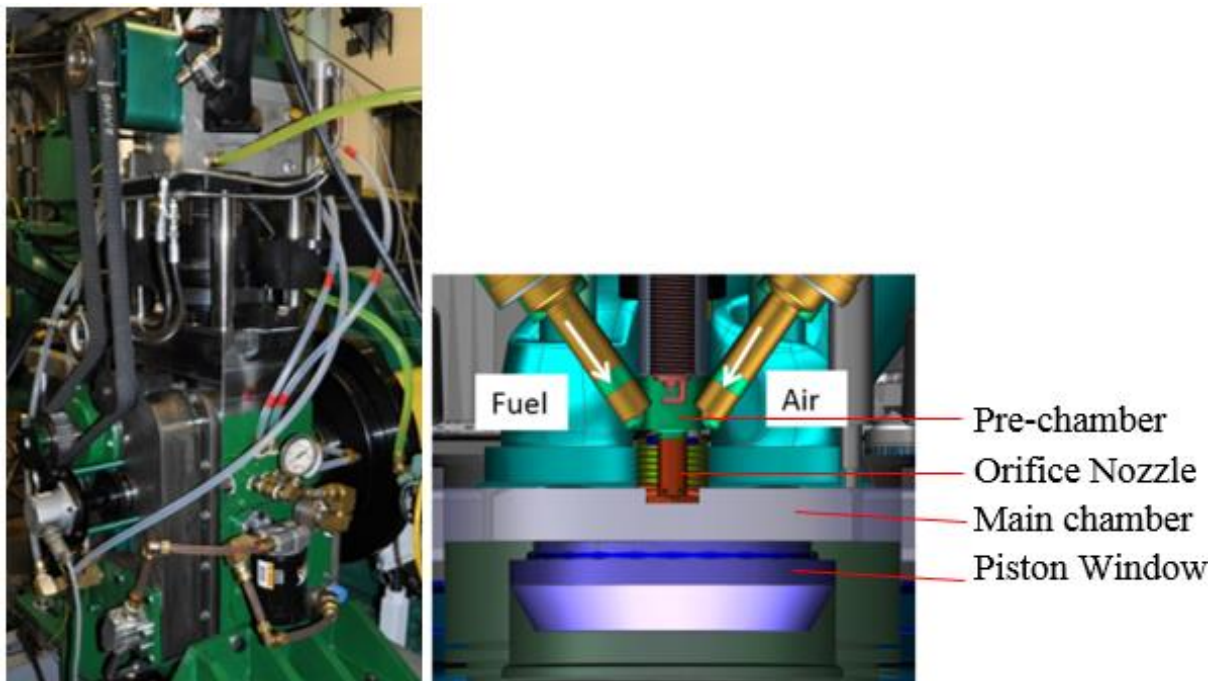


Figure 3.1: Dual-Mode TJI optical engine (left) and sectional view showing the details of its architecture (right).

Table 3.1: DM-TJI Engine Specifications

Bore	95 mm
Stroke	100 mm
Connecting Rod Length	190 mm
Compression Ratio	9.5:1
Motored Peak Pressure	19 bar at TDC
Pre-chamber Volume	2700 mm ³ (4.3% of main chamber clearance volume)
Main Chamber Swept Volume	0.709 L
Fuel Injector	High- or low-pressure injector for main chamber High-pressure injector for pre-chamber
Fuel	EPA LEV-II liquid gasoline (both chambers)
Engine Speed	1500 rpm

Coefficient of variation (COV) in the indicated mean effective pressure (IMEP) determined over 100 engine cycles was considered as an index for combustion instability. The stability limit was defined by a COV of IMEP less than 2.0%. A wideband oxygen sensor (or the lambda sensor) mounted in the exhaust manifold was used to record the global air/fuel equivalence ratio (λ) values. The global λ value was considered as a metric to represent leanness of fuel-air mixture. These two variables, COV IMEP and global λ , were chosen to design the current set of operating conditions for the DM-TJI engine.

3.2.2 Engine Controls and Data Acquisition

Gasoline was primarily used in both chambers. High-pressure DI injectors were employed for both fuel and air injections in the pre-chamber. A low-pressure PFI injector and a high-pressure DI injector were tested separately for fueling the main chamber; while installing the injector in the

intake port. A cylinder of compressed nitrogen gas was used to pressurize the fuel tank at a pressure controlled by the cylinder regulator. A Kistler type 6117BFD17 spark plug and pressure sensor combination (see **Figure 3.2**) was used to record pre-chamber pressure data. A piezoelectric pressure transducer (Kistler type 6125C) inserted in the main chamber was used to record main chamber pressure data. The charge output from the transducers was converted to an amplified voltage using a DSP Technologies model 1104CA charge amplifier.



Figure 3.2: Front- and bottom-views of the spark plug combined with pressure sensor for pre-chamber measurements.

A Mototron controller sent the control signals to an injector drive box to control injection and spark timing, and injection pulse widths as shown in **Figure 3.3**. The controller provided the camera trigger as well. The controller received the crank and cam signals from the engine for syncing with the compression top dead center (TDC) position. The control signals were outputted from the Mototron to the injector driver. A Wineman System DC Dynamometer was used to ramp the engine. The chamber pressure-related signals were recorded during engine operation using an A&D Technologies' Phoenix-AM high speed combustion analysis system (CAS) that is capable

to record data at 0.1 crank angle resolution. The data from the current testing were recorded at 1.0 crank angle resolution for saving acquisition time and ease in data handling. The CAS TDC position was synchronized with piston TDC position using an encoder. After acquiring data with one test condition, the control parameters were changed using the Mototune software that allows to send signals to the Mototron controller.

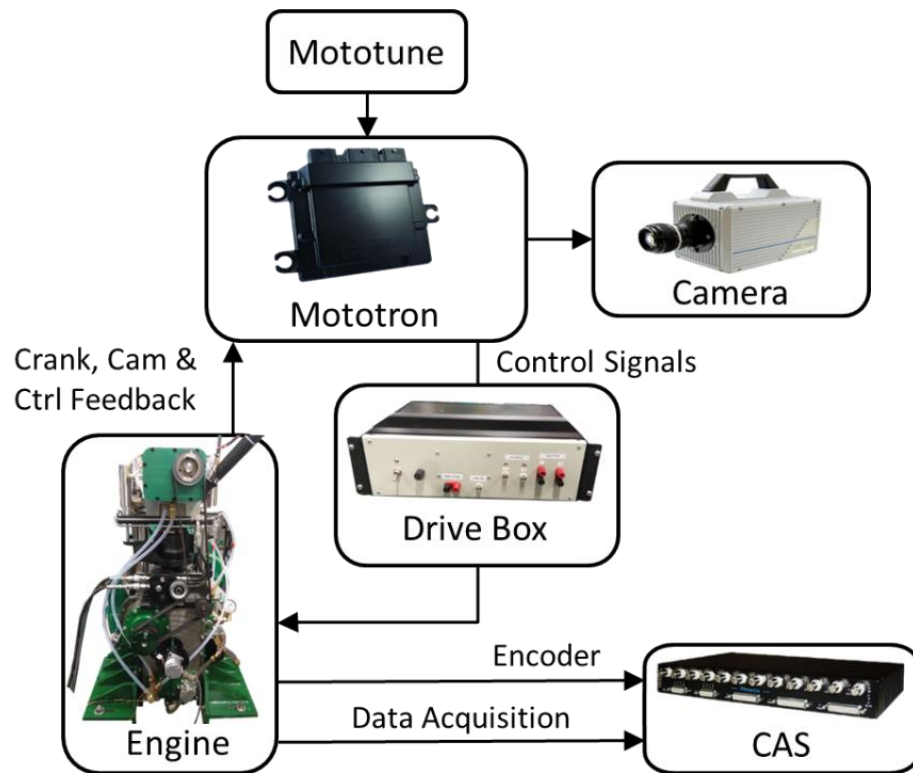


Figure 3.3: Optical Engine Controls System.

The pre-chamber fuel timing was set at 80 CAD before TDC and the injection pressure was 1500 psi (103 bar). It is to be noted that all crank angles are with reference to compression TDC position. A special feature of this engine was to include pre-chamber air injection. A conventional DI fuel injector was used to inject air at about 60 bar. The injection parameters are listed in **Table 3.2**. The spark dwell was 1.7 ms and the spark timing was set at 25 CAD bTDC.

Table 3.2: Fuel and Air Injection Settings

<i>Pre-chamber Air:</i>	
Injection pressure	870 psi (60 bar)
Injection pulse width	1.4 ms
Injection timing	0.2 ms before pre-chamber fuel injection
<i>Pre-chamber Fuel:</i>	
Injection pressure	1500 psi (103 bar)
Injection pulse width	1.1 to 1.5 ms
Injection timing	80 CAD bTDC
<i>Main chamber Fuel (with low-pressure injector):</i>	
Injection pressure	40 psi (2.7 bar)
Injection pulse width	12 to 14 ms
Injection timing	300 CAD bTDC, 330 CAD bTDC
<i>Main chamber Fuel (with high-pressure injector):</i>	
Injection pressure	1500 psi (103 bar)
Injection pulse width	5 pulses of 0.75 ms; pulse-to-pulse = 4 ms
Injection timing	360 CAD bTDC

3.2.3 Combustion Imaging

A PHOTRON APX-RS high-speed visible video camera with a lens objective of f/0.95 was used to capture the low-luminous combustion of lean-burn conditions in the DM-TJI optical engine. Combustion events of 40 cycles were captured viewing through a 50.75 mm diameter sapphire window inserted in the piston, and the 45-degree mirror at an imaging frame rate of 5000 frames/sec. The image size was 384x384 pixels which corresponds to a resolution of 5.4 pixels/mm. **Figure 3.4** shows the camera positioned against the piston mirror for viewing the combustion chamber through the piston window. This frame rate corresponds to a temporal

resolution of about one frame for every other crank angle at an engine speed of 1500 rpm. The camera was externally triggered with a 5V transistor-transistor logic (TTL) pulse provided by the Mototron controller as shown earlier in **Figure 3.3**.

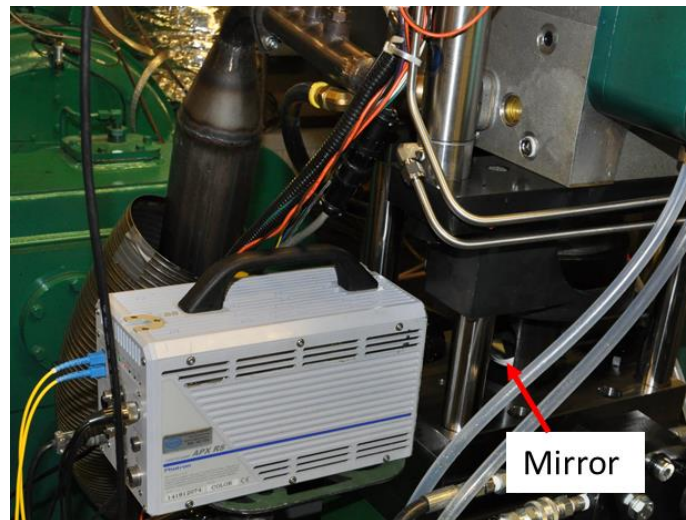


Figure 3.4: Camera setup for bottom-view imaging of combustion.

3.3 RESULTS AND DISCUSSION

3.3.1 DM-TJI Engine: With a Low-Pressure Injector for Main Chamber Fueling

Pressure traces of pre-chamber and main chamber of an individual cycle along with the corresponding combustion event images are shown in **Figure 3.5**. The falling edge of the spark timing was set to -25 CAD aTDC. The edge of the piston window or the field of view is added in the images as white-circle for clarity. The label under each image is crank angle after TDC (-ve value means angle before TDC). The visible jet discharged from the pre-chamber to the main chamber was first seen after 7 CADs. On the other hand, the pressure rise in the pre-chamber started at about 4 CADs after spark. This observation could indicate that either the camera sensor's minimum threshold is higher than the luminosity of the reacting jet or the jet (and its partially-combusted precursor flame) took the time to develop and reach the main chamber. Another

possibility is that these initial jets might not be luminous in the visible spectrum [92]. Luminosity of jet increased in the next recorded image (-16.0 CAD aTDC) and the pressure reached a peak point accordingly indicating pre-chamber flame propagation. The jet was seen to spread out and diminish in the next couple of images and the pressure dropped in the pre-chamber indicating the end of jet discharge event. The pressure rise in the main chamber was at about -16.0 CAD aTDC which is the same time when the pre-chamber pressure peaked. Multiple yellow spots were consistently observed, as in the right-half of image at 0.2 CAD aTDC, which can be attributed to burning droplets that were initially located near the intake valve as shown in **Figure 3.6**.

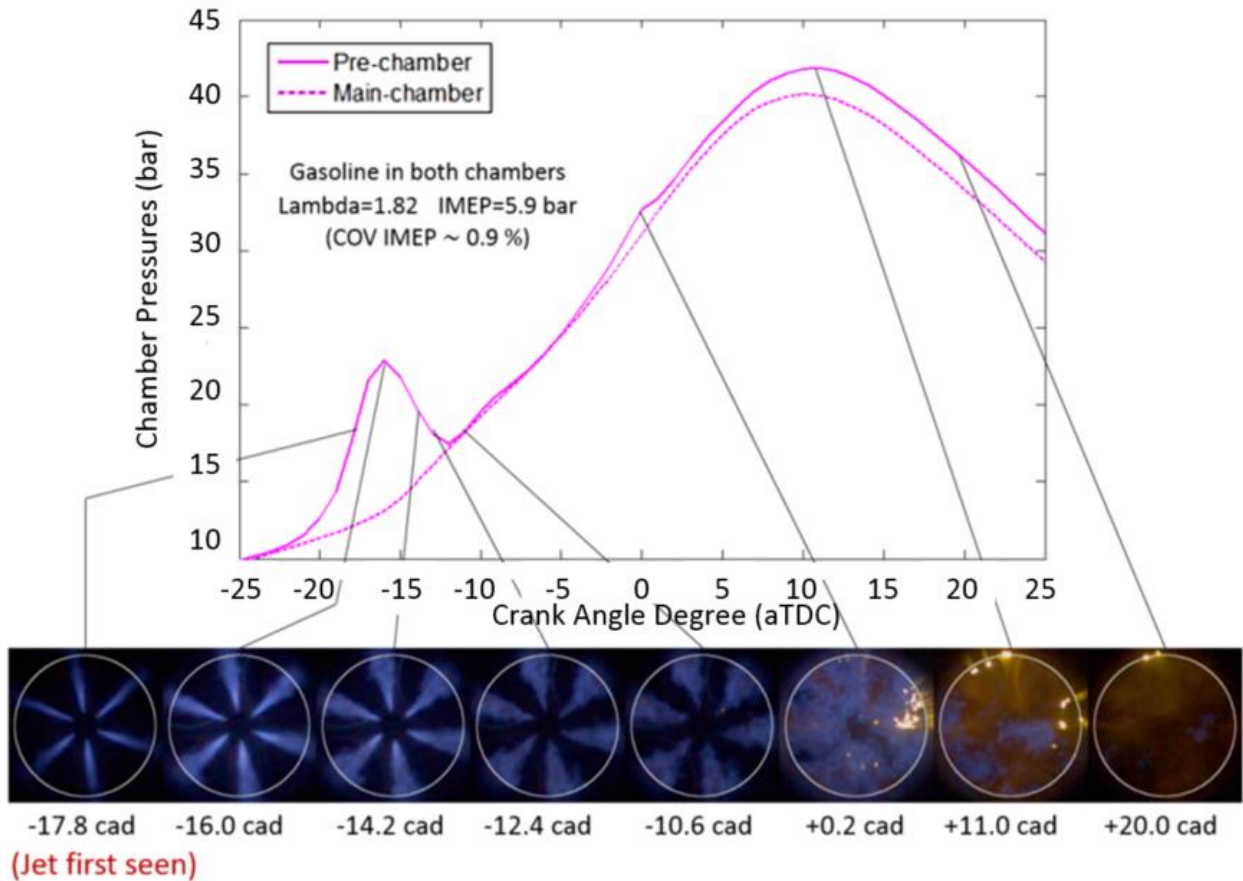


Figure 3.5: Pre-chamber and main chamber pressure traces and phase-synchronized images of combustion events for $\lambda=1.8$.

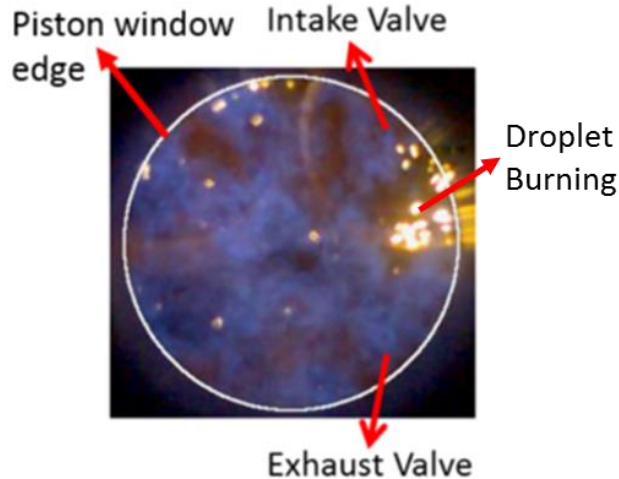


Figure 3.6: Camera view of the combustion chamber.

Knowing the source of these droplets is essential to control undesirable particulates in the emissions. To this effect, gaseous methane was used in the following fuel combinations: a) Methane in pre-chamber, gasoline in main chamber; b) Gasoline in pre-chamber, methane in main chamber. A separate set of experiments were performed where the sole target was to know the source of droplets. Hence, these set of experiments involved operating conditions that either resulted in several misfires or a COV IMEP value greater than 10 and no further optimization was attempted. Also, the spark timing and injection pulse widths were slightly varied among these test conditions. **Figure 3.7** shows images for different fuel combinations wherein first (gasoline in both) and third (methane in pre-chamber) frames correspond to a duration of same number of crank angles after the jet was first seen. The second image (methane in main chamber) showed a blue jet with a tinge of orange near the orifice exit as indicated with a white arrow there. The occurrence of smaller droplet(s) that moved radially along the jet could not be embedded in a single frame to show here, however, were seen in the recorded videos. In contrast, the droplets initiated near the intake valve for the other two cases that had gasoline in the main chamber. These two cases exhibited similar droplet trajectories wherein the droplets moved towards left flowing along with

the counter-swirl flow in the main chamber. These observations indicate that the droplets seen in **Figure 3.6** most likely resulted from the incompletely atomized liquid fuel coming from the low-pressure injector.

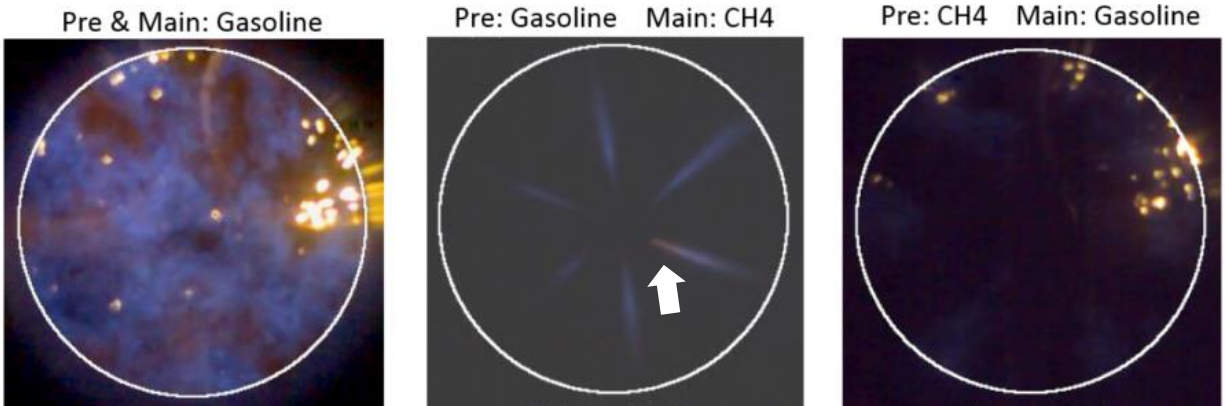


Figure 3.7: Combustion images showing burning droplets for different fuels in the pre- and main chamber.

3.3.2 DM-TJI Engine: With a High-Pressure Injector for Main Chamber Fueling

Based on above findings regarding the source of droplets, it was decided to switch over to a high-pressure injector in the intake port. First, a single injection pulse was used and the later stage of combustion showed a shade of darker-red indicating soot luminosity. So the Mototron program was updated to include multiple injection pulses for the injector in the intake port. With this setup, a single large injection was divided into multiple smaller injection sequences per cycle with a preset pulse-to-pulse duration (4 ms in the current study). Three different conditions were tested with the pre-chamber fuel pulse width increments of 0.2 ms while keeping all other parameters the same. The output variables of interest based on 100 cycle average are included in **Table 3.3**. The indicated efficiency was estimated using the equation,

$$\text{Indicated Efficiency} = \left(\frac{\text{IMEP} * \text{Swept Volume}}{\text{LHV} * m_{fuel}} \right) \quad (3.1)$$

where LHV is the lower heating value of fuel = 41.8 MJ/kg. Fuel injector calibrations were performed to determine the total amount of fuel injected, m_{fuel} , into the pre-chamber and main chamber for each fuel injection pulse width.

Table 3.3: Output Variables of Interest

	IMEP (bar)	COV (%)	Global λ	Indicated Efficiency (% Estimated)
Pre-chamber Fuel=1.1 ms	5.78	1.2	2.10	42.8
Pre-chamber Fuel=1.3 ms	5.80	1.1	2.09	42.6
Pre-chamber Fuel=1.5 ms	5.84	1.2	2.08	42.5

The engine was demonstrated to run at a global $\lambda \approx 2.1$ with an acceptable COV IMEP of 1.2% for an IMEP of approximately 5.8 bar (average of 100 cycles). This operating condition resulted in an indicated efficiency of about 42.8%. The corresponding combustion images for the three pre-chamber fuel injection timings included in **Table 3.3** are shown in the **Figure 3.8** where numbers on the top are crank angles after compression TDC. As seen here, burning droplets were almost completely eliminated for the whole combustion duration up to MFB 90% with the new injection setup. The contrast of the first image in the top row had to be additionally enhanced in order to see the emerging jet on the upper-left. Overall, longer pulse widths (P.C Fuel) showed longer jet penetration and a brighter jet near the orifice exit indicating probable soot formation. Starting from about TDC position (0.2 cad aTDC), the images for all the conditions exhibited a fainter flame. Lower natural luminosity is attributed to leaner equivalence ratio [106].

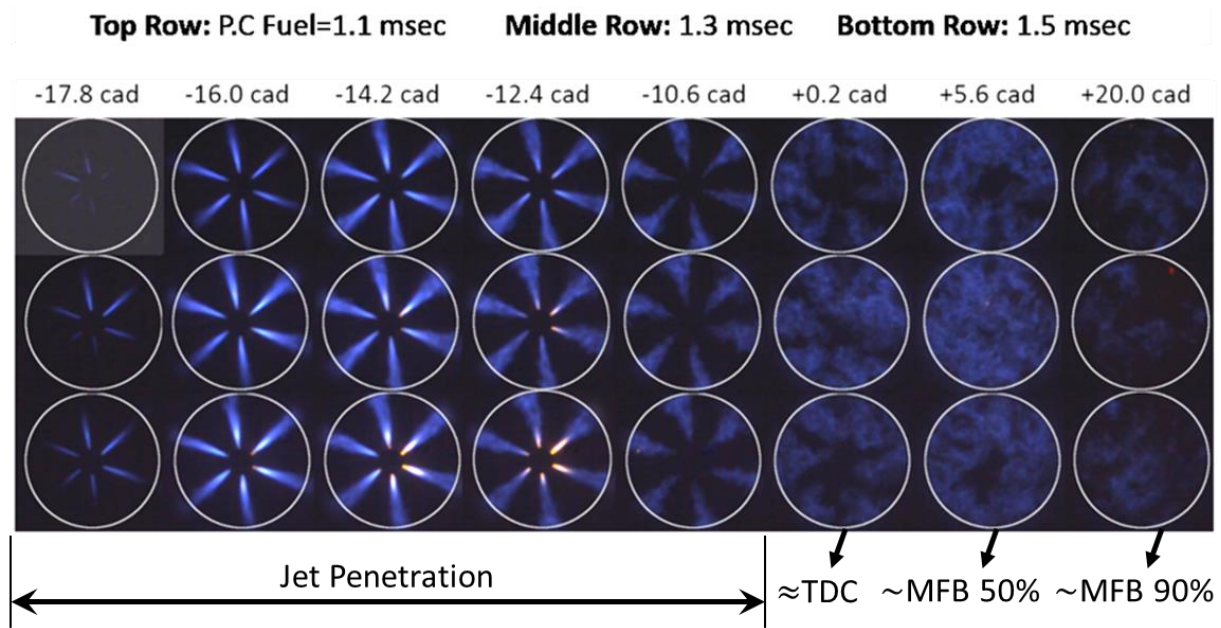


Figure 3.8: Main chamber combustion images for three different pre-chamber fuel pulse widths.

While testing different pre-chamber gasoline injection parameters with methane in main chamber, the combustion during initial cycles showed bright luminous flame and burning droplets whose occurrence was notably reduced during later cycles recorded. This could be accounted to the pre-chamber warm up effect. An operating condition was found that could heat up the pre-chamber within 10 to 15 seconds of engine firing (COV IMEP drops to 1% more rapidly than for other conditions tested).

3.4 SUMMARY

A Dual-Mode TJI optical engine was tested at different engine speeds while focusing on the combustion behavior at 1500 rpm. This engine incorporated an air injector in the pre-chamber along with the fuel injector and spark plug. Gasoline was used in both pre-chamber (direct injection) and main chamber (port fuel injection) for the main set of experiments. All communications to the engine and its controls were made using Mototron control system. Global

λ value and COV IMEP were considered to qualitatively measure the leanness and stability of combustion, respectively. Experiments conducted with a low-pressure injector, for injecting fuel in the main chamber, resulted in noticeable burning droplets. These droplets were concluded to arise from the low-pressure injector of main chamber after replacing gasoline with gaseous methane in pre-chamber or main chamber. Based on these findings, the low-pressure injector was replaced with a high-pressure injector for main chamber that was port fuel injected. Also, multiple injection pulses were employed per cycle with the high-pressure injector and the resulting combustion showed negligible traces of droplets during the entire combustion event for a global $\lambda \approx 2.1$ and a COV IMEP of 1.2%. The 1500rpm/6 bar IMEP speed/load conditions identified from this study delivered an estimated indicated efficiency of close to 43%. It should be noted that this efficiency includes the amount of work input required to drive the pre-chamber air injector. The amount of work required to supply air to the pre-chamber was estimated to be 1% by using a one-dimensional engine model as discussed in the Appendix. This would lead to a corrected indicated thermal efficiency of 42% for the current DM-TJI engine with a compression ratio of 9.5.

CHAPTER 4

Thermal Efficiency of a High Compression Ratio Dual-Mode Turbulent Jet Ignition Gasoline Engine Under Near-Stoichiometric Operation

4.1 SYNOPSIS

In this work, the compression ratio of the DM-TJI optical engine was increased to 12.0 by lowering the squish height. Also, this DM-TJI engine configuration consists of a metal piston with bowditch extension. High speed pressure-related recordings were used to compare and analyze different operating conditions up at 1500 rpm part-load conditions. Coefficient of variation in the indicated mean effective pressure and the global air/fuel equivalence ratio values were used to characterize the engine testing operating conditions. In the end, operating conditions for a global air/fuel equivalence ratio of 1.85 were identified that offered an indicated efficiency of $46.0\% \pm 1\%$ at 1500 rpm and 6.0 bar IMEP.

In addition, the combustion stability of this engine was tested with nitrogen-simulated exhaust gas recirculation (EGR). The EGR % was controlled by monitoring the intake O_2 % that was recorded by a wideband O_2 sensor mounted in the intake manifold. After rigorous testing, the DM-TJI engine of compression ratio 12.0 was demonstrated to deliver an estimated indicated efficiency of $46.6\% \pm 1\%$ under near stoichiometric operation at 1500 rpm and 7.7 bar IMEP.

4.2 EXPERIMENTAL SETUP

4.2.1 High Compression Ratio DM-TJI Engine

The DM-TJI engine with metal piston has a compression ratio of 12.0 based on the measured squish height. The cylinder head was lowered by removing shims under the head until the main chamber clearance height was 8.74 mm that reflected a compression ratio of 12.0. The engine consists of a flat head that was pre-heated by flowing coolant through the flow passages.

The coolant used was 50:50 ethylene-glycol water mixture that was heated to 90°C using an electrically-powered heating element. Using a PID (proportional-integral-differential) controller, the temperature was maintained at this set temperature during the entire testing time. Such an approach of pre-heating the head is usually employed for single-cylinder research engines to attain metal engine steady temperatures. **Figure 4.1** shows a drawing of the engine highlighting various parts of the DM-TJI system installed on the head. A high-pressure fuel injector and a high-pressure air injector were inserted in the pre-chamber. The orientation plane of these pre-chamber injectors is out-of-paper and hence, are not viewable in **Figure 4.1**. For the main chamber fueling, a high-pressure fuel injector was located in the intake port. A measuring spark plug (Kistler 6117BFD17) that incorporates a pressure transducer was employed for pre-chamber pressure measurements. A six-orifice nozzle was used to connect the pre-chamber to the main chamber. Various dimensions and other details of this engine are given in **Table 4.1**.

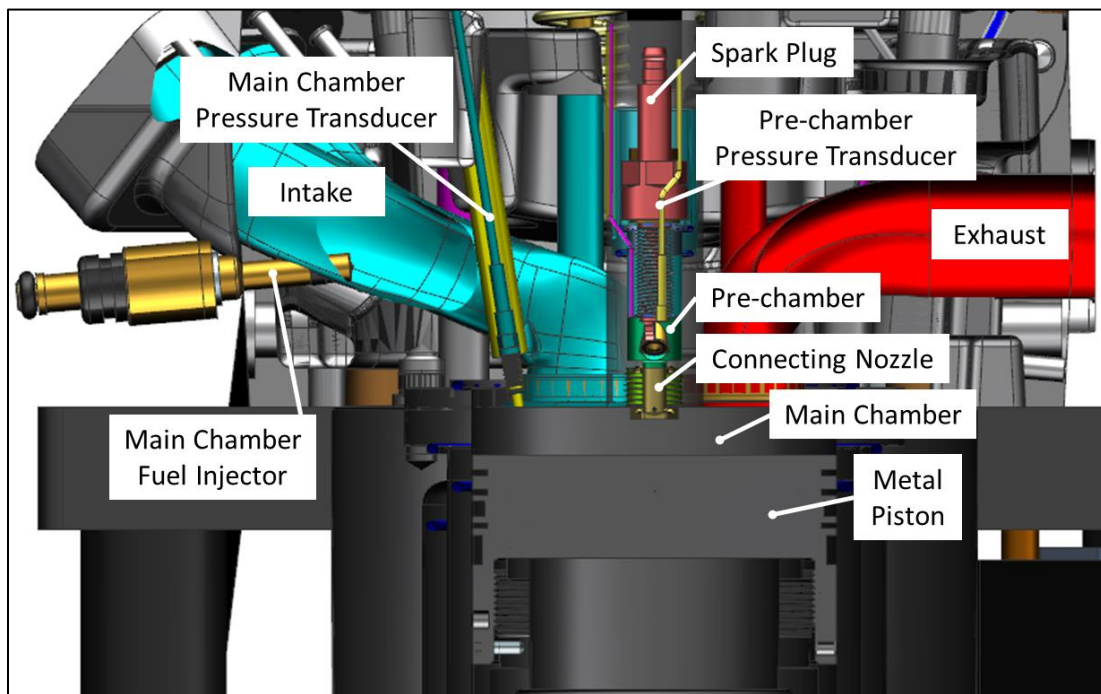


Figure 4.1: High compression ratio DM-TJI engine with metal piston.

Table 4.1: Specifications of DM-TJI Engine with Extended Metal Piston

Bore	95 mm
Stroke	100 mm
Connecting Rod Length	190 mm
Compression Ratio	12.0:1
Motored Peak Pressure	22.5 bar at TDC
Pre-chamber Volume	2700 mm ³ (4.3% of main chamber clearance volume)
Main Chamber Swept Volume	0.709 L
Fuel Injection	High-pressure injectors for both chambers
Fuel	EPA LEV-II liquid gasoline (both chambers)
Engine Speed	1500 rpm
Engine Load	~6.0 bar IMEP (Wide open throttle) – without EGR ~7.7 bar IMEP (Wide open throttle) – with EGR

Coefficient of variation (COV) in the indicated mean effective pressure (IMEP) determined over 100 engine cycles was considered as an index for combustion instability. The stability limit was defined by a COV of IMEP less than 2.0%. A wideband oxygen sensor mounted in the exhaust manifold was used to record the global air/fuel equivalence ratio (λ) values. The global λ value was considered as a metric to represent leanness of fuel-air mixture. These two variables, COV IMEP and global λ , were chosen to design the current set of operating conditions for the DM-TJI engine.

4.2.2 Nitrogen-Simulated EGR Dilution

Exhaust gas recirculation was simulated by adding nitrogen to the engine intake flow. Nitrogen was supplied from a bank of nine compressed N₂ cylinders, arranged next to the engine.

A quarter-turn ball valve was manually opened to allow nitrogen to flow through a large plenum attached to the intake manifold, upstream of the throttle plate, as shown in **Figure 4.2**. A hollow cylinder was attached to top of the plenum through which the nitrogen supply tube was inserted. The end of nitrogen tube that goes into the plenum has 5 orifices (4 tangential and 1 vertical). The air entered the engine at the plenum through the annular region of the hollow cylinder. The orifice design as employed for the nitrogen tube was intended for better air and nitrogen mixing.

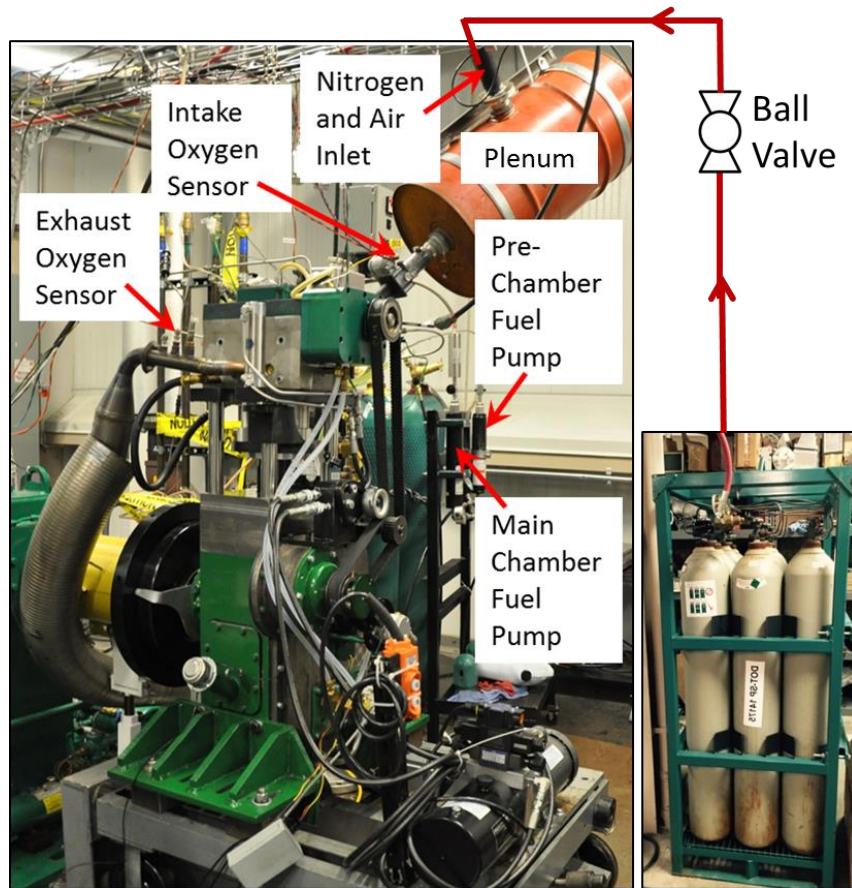


Figure 4.2: Experimental setup for DM-TJI engine with EGR dilution.

As shown in **Figure 4.2**, two oxygen sensors were employed while working with EGR dilution. The EGR % was quantified by the amount of intake oxygen measured using the intake oxygen sensor. The burn quality of combustion was realized by the amount of exhaust oxygen as

measured using the exhaust oxygen sensor. A high exhaust O₂ % is indicative of a high temperature combustion, which further results in high NO_x formation [107]. A low exhaust O₂ % indicates that all the oxygen was consumed for burning fuel during combustion. This could indicate either stoichiometric or fuel-rich combustion. One of the primary goals of this part of the study is to operate the DM-TJI engine under near-stoichiometric conditions with EGR dilution. The EGR dilution efforts aimed for reduced NO_x formation during combustion and near-stoichiometric operation aimed to reach light-off temperatures for a closely-coupled three-way catalyst (oxidize CO and HC). To this effect, operating conditions that ideally resulted in an exhaust O₂ of 0.5% were sought.

The main chamber events of selected operating conditions were recorded using a PHOTRON APX-RS high-speed visible video camera with a lens objective of f/0.95. For these set of experiments, a sapphire window of 66 mm diameter was inserted in the extended piston, for optical access to the main chamber. Combustion events were captured at an imaging frame rate of 5000 frames/sec. The image size was 302x302 pixels which corresponds to a resolution of 4.6 pixels/mm. This frame rate corresponds to a temporal resolution of about one frame for every other crank angle at an engine speed of 1500 rpm. The camera was externally triggered with a 5V transistor-transistor logic (TTL) pulse provided by the Mototron controller.

4.3 RESULTS AND DISCUSSION

4.3.1 DM-TJI Engine: Without EGR Dilution

While keeping all other parameters the same, different spark timings were tested at 1500 rpm and 6 bar IMEP speed/load condition. Both pre-chamber peak pressure and main chamber heat release rate (HRR) increased with spark advance as shown in **Figure 4.3**. The HRR calculation was based on Heywood's model [105] while the heat loss terms are neglected for a

simple analysis. With spark timing of 25 CAD bTDC, the main chamber peak HRR occurred earlier than the pre-chamber pressure second peak occurrence. The indicated efficiency was calculated as described earlier in Section 4.3.2. For the same amount of fuel used, this spark timing resulted in the highest indicated efficiency of 45.14% compared to the other two spark timings. This indicates that the maximum work was extracted with the advanced spark timing for the given fuel and air injection conditions.

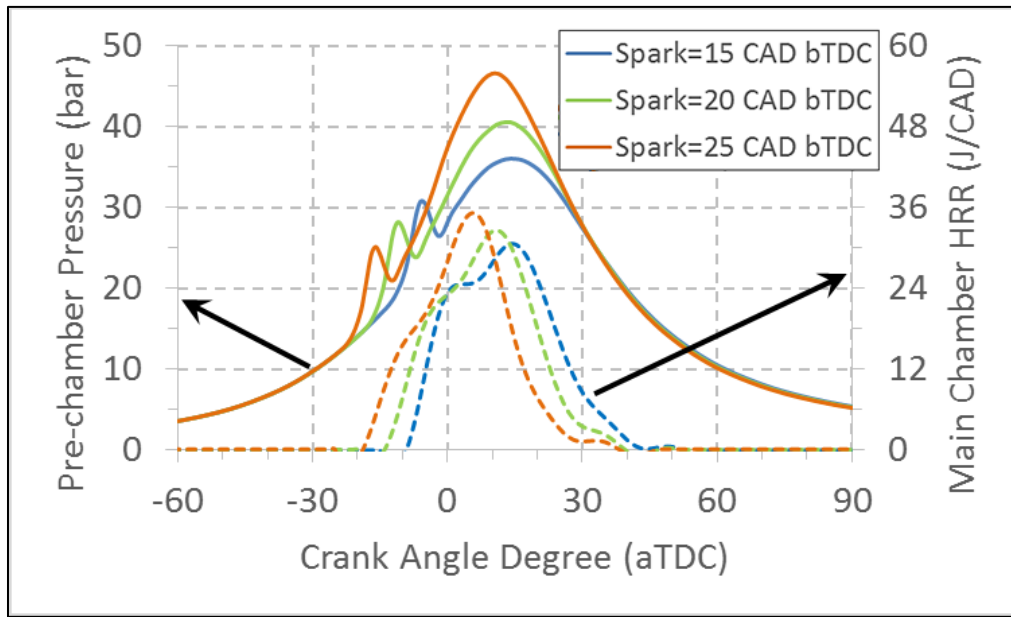


Figure 4.3: Pre-chamber pressures and main chamber heat release rates for different spark timings.

With spark timing set at 25 CAD bTDC, different pre-chamber fuel timings were tested: a) 120 CAD bTDC – early fuel injection (EFI); b) 80 CAD bTDC – middle fuel injection (MFI) and c) 40 CAD bTDC – later fuel injection (LFI). All these tests involved only one fuel injection pulse in the pre-chamber, with a pulse width of 0.90 ms. It should be noted that the MFI pre-chamber fueling condition was employed in the earlier discussion related to **Figure 4.3**. Also recall that this combination of injection and spark timing resulted in an indicated efficiency of 45.14%. Ignition

delay in the pre-chamber was defined as the duration between spark initiation and the time when the pre-chamber pressure differential first reached about 25% of its maximum pressure differential. This percentage was chosen based on visual inspection of inflection point on the pressure trace. With this definition, it was observed that the pre-chamber ignited faster with EFI condition followed by MFI and LFI conditions.

As shown in **Figure 4.4**, the first pre-chamber peak pressure was higher for LFI condition indicating the occurrence of a high-speed jet in this injection condition. Ignition delay in the main chamber was defined as the duration between spark initiation and the time when the main chamber pressure differential first reached about 25% of its maximum pressure differential. It was observed that the main chamber ignited almost at the same time since the start of pre-chamber ignition (PCI) for all fuel injection conditions. The combustion phasing angle for main chamber, however, was 2-3 CADs earlier for the LFI condition compared to the other two injection conditions. The LFI condition showed higher combustion pressures (-14 CAD aTDC and beyond in **Figure 4.4**) and remained to possess the highest combustion peak pressure, which was 3.5 bar more than that obtained with the EFI condition. With the global $\lambda \cong 1.85$, the EFI injection condition resulted in a 1% increase in the indicated thermal efficiency compared to MFI and about 0.6% higher than with LFI condition. The low chamber pressure might implicate a low combustion temperature with the EFI condition. Low temperature combustion reduces the heat losses, thereby, resulting in high indicated work output with EFI condition. Therefore, with this pre-chamber injection testing, the new indicated efficiency of the DM-TJI engine is 46.00% at 1500rpm/6.0 bar IMEP. It should be noted that this efficiency includes the work required to pump high-pressure air into the pre-chamber. Also, the current non-optimized results were obtained for a fixed spark timing. It would be worthwhile to check the consistency of these results when tested with different spark timings.

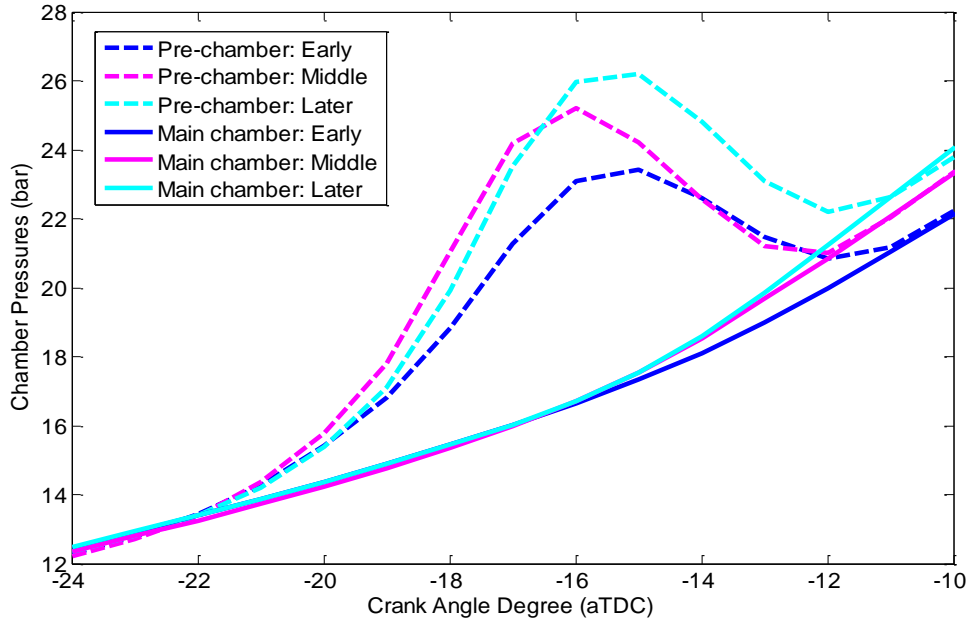


Figure 4.4: Pre-chamber and main chamber pressures for different pre-chamber fuel injection timings.

4.3.2 DM-TJI Engine: With EGR Dilution

4.3.2.1 Effect of Air Injection in the Pre-chamber

The importance of having an air injection in the pre-chamber can be illustrated using the IMEP plots in **Figure 4.5**. For 1500 rpm/6.0 bar IMEP condition with EGR (nitrogen dilution) of 25.8% (intake $O_2\%$ of 15.5%), one misfire was detected without air injection in the pre-chamber and no misfires occurred with pre-chamber air injection. When the EGR was further increased to 27.3%, several misfires were detected without pre-chamber air injection. Among these misfire cycles, majority of misfires occurred in the main chamber while occasional misfires were detected in the pre-chamber as well. The absence of misfires by having an air injection in the pre-chamber hint the capability of the DM-TJI engine to operate at an ideal EGR-diluted near stoichiometric mixture burning condition. The EGR dilution helps in reduced NO_x formation and the stoichiometric operation provides catalyst light-off temperatures in the exhaust manifold to oxidize CO and any unburnt HC emissions and/or reduce NO_x using a close-coupled three-way catalyst.

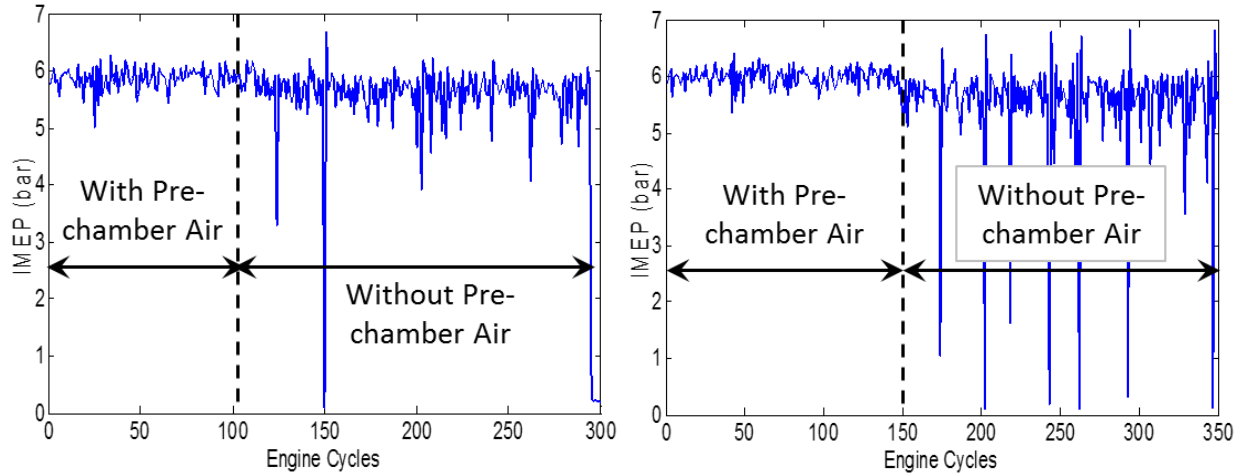


Figure 4.5: Effect of having pre-chamber air injection on the combustion of diluted mixture consisting an intake O_2 of 15.5% (left) and 15.2% (right).

4.3.2.2 Main Chamber Fuel Injection Pulse Width

The MFI fuel injection condition (80 CAD bTDC) in the pre-chamber was used for EGR dilution testing with more fuel mass injected there compared to without dilution. Also, for enhanced combustion stability with EGR dilution, a high-energy ignition coil of around 80 mJ was employed (compared to previously used plug of ~ 30 mJ). With the spark timing set at the same 25 CAD bTDC, three main chamber fuel injection pulse widths were tested at approximately 25% EGR (20.9% intake O_2 considered as zero EGR point). The outputs of interest are listed in **Table 4.2**. All EGR-diluted conditions showed good combustion stability with a COV IMEP below 1.30%. As the amount of fuel injected in the main chamber (port fuel injected) was increased, the IMEP value increased and the exhaust O_2 % decreased. At first, it might be conceived that the higher fuel resulted in higher indicated work. However, the indicated efficiency results showed that the condition having smallest fuel pulse width benefitted the most out of the fuel energy used. Lower efficiency with the largest fuel pulse width condition can be explained by looking at the burn durations as included in the third column of **Table 4.2**. The values within the square brackets are crank angles CA10 and CA50, and burn duration CA10-90. The condition with largest pulse

width (5 x 0.9 ms) resulted in an earlier CA10, CA50, as well as fastest CA10-90 duration. A combustion phasing close to TDC, as seen with this largest pulse width condition, indicates increased compression work and heat losses, thereby resulting in relatively lower efficiency [108].

Table 4.2: DM-TJI Engine Results with Approximately 25% EGR Dilution

Main Chamber Fuel Pulse Width (ms)	Intake O ₂ %	IMEP (bar) [CA10, CA50, CA10-90]	COV IMEP (%)	Exhaust O ₂ %	Indicated Efficiency (Estimated)
5 x 0.80	15.66	6.474 [-5,7,23]	1.29	4.45	44.99%
5 x 0.85	15.61	6.741 [-6,5,21]	1.18	3.85	44.20%
5 x 0.90	15.58	6.990 [-7,3,19]	1.12	3.27	43.39%

Figure 4.6 shows the corresponding pre-chamber and main chamber pressures plots for these fuel pulse widths. As seen here, the main chamber combustion peak pressure occurred earlier with an increase in the fuel pulse width. A common observation for the non-optimized conditions shown in **Figure 4.6** and **Figure 4.4** is that a lower main chamber peak pressure resulted in highest indicated efficiencies. Also, for the chosen spark and pre-chamber fuel injection timings, an earlier pre-chamber ignition time and a lower pre-chamber pressure before reaching its first peak (as seen in the zoomed-in view on the right) resulted in highest indicated efficiency. Thus it is believed that the reduced heat losses in both pre-chamber and main chamber as well as better mixing in the main chamber contributed to the maximum expansion work from fuel combustion. As mentioned earlier, it would be worthwhile to validate these findings by testing with different spark timings.

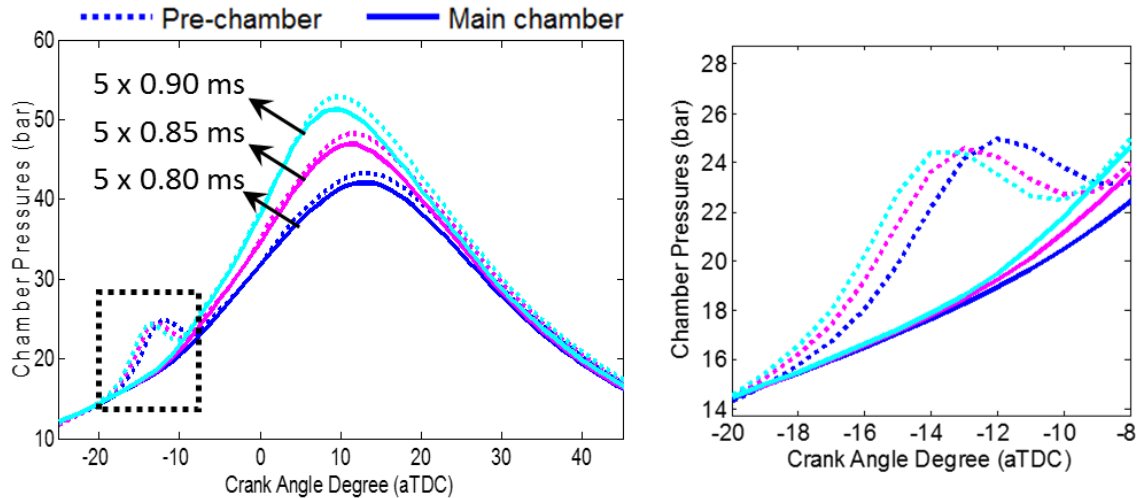


Figure 4.6: Comparison of pressures for different main chamber fuel pulse widths (left) and zoomed-in view of pre-chamber pressure first peak regions.

4.3.2.3 Spark Sweep for Early Pre-chamber Fuel Injection Condition

An early fuel injection in the pre-chamber resulted in higher indicated efficiency without intake dilution as seen earlier while discussing **Figure 4.4** results. This effect was tested here with EGR dilution. Spark sweeps were conducted for two different early fuel injection timings in the pre-chamber while maintaining a constant EGR of approximately 30%. The injection timings considered were 120 CAD bTDC (called as EFI-1) and 160 CAD bTDC (called as EFI-2). It should be recalled that an increase in the main chamber fuel pulse width reduced the exhaust O₂ % (**Table 4.2**). To achieve the goal of near stoichiometric operation with EGR dilution, the amount of fuel injected in the main chamber was further increased. This higher fuel mass in the main chamber resulted in a maximum IMEP of 7.7 bar, for maximum spark advance, compared to the standard value of 6.0 bar as implemented in the previous tests of this work. In addition to the higher overall fuel injected, the pulse-to-pulse duration was increased to 5 ms. Also, the pre-chamber air injection pulse width was slightly increased to compensate for the predominantly diluted main chamber air/fuel mixture entering the pre-chamber during compression stroke. The corresponding results obtained with the two pre-chamber fuel injection timings are shown in **Figure 4.7**. The COV IMEP

was less than 2% for a wide range of spark timings demonstrating the high combustion stability observed at these EGR-diluted operating conditions. The CA50 crank angle occurred earlier with the spark advance. An exception to this was for 36 CAD bTDC with EFI-2 which could indicate the limit of spark advance for combustion stability as implied by a higher COV IMEP seen at this spark timing. The exhaust O₂ was observed to be around 1.0% for all the spark timings with both EFI-1 and EFI-2. For EFI-1 injection condition, the indicated efficiency increased by advancing spark and a maximum value of 46.62% was obtained for a spark timing of 27 CAD bTDC. For EFI-2 injection condition, the indicated efficiency reached a maximum at 27 CAD bTDC, then plateaued up to 33 CAD bTDC, and dropped at 36 CAD bTDC spark timing. Based on these results, the optimal operating points that offered high combustion stability, near-stoichiometric combustion, and high thermal efficiency are circled in **Figure 4.7** for the two pre-chamber fuel injection conditions.

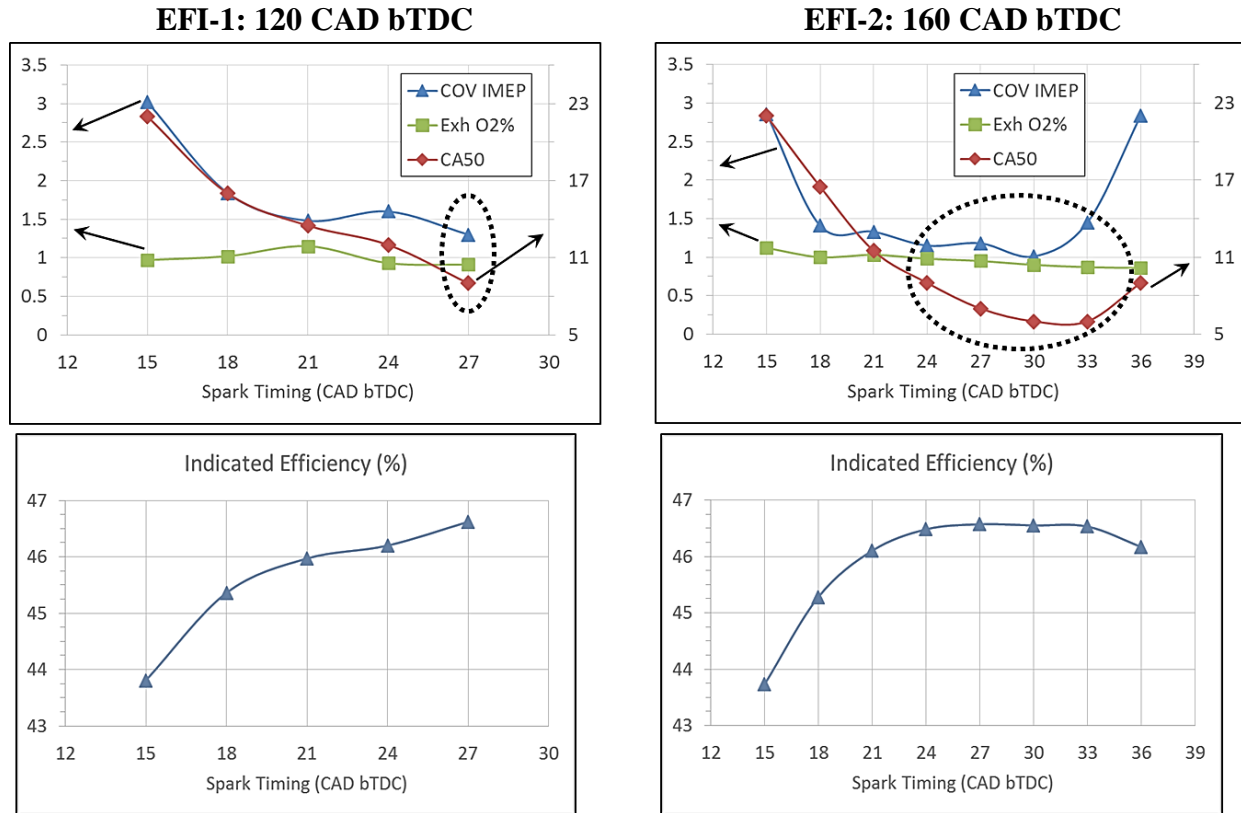


Figure 4.7: Graphical plots showing the DM-TJI engine test results with approx. 30% EGR.

Figure 4.8 shows the heat release rates for selected spark timings with EFI-1 and EFI-2 pre-chamber fuel injection condition. The EFI-1 condition with maximum spark advance that delivered highest indicated efficiency, resulted in an earlier and higher peak HRR in the main chamber. In addition, the condition with retarded spark timing (15 CAD bTDC) had a widely spread heat release curve, representing a slowly propagating flame. Similar observations were evident for the EFI-2 injection condition. Spark timing beyond 27 CAD bTDC, however, showed a decline in the peak HRR. This lower peak HRR and the slower combustion would be the factors leading to lower efficiency and relatively high combustion instability at 36 CAD bTDC for EFI-2 condition as seen earlier in **Figure 4.7**. In a different viewpoint, the prolonged duration for the HRR to reach 0 to 10 J/CAD with a retarded spark timing could be related to the mixture preparation times in the main chamber. For a retarded spark timing of 15 CAD bTDC, the HRR

curves with both EFI-1 and EFI-2 injection conditions showed a gradual rate of heat release. This could indicate that the main chamber contained locally excess lean regions due to additional mixing time available before spark. Thus the reacting jet could have possibly taken longer to initiate combustion in the main chamber compared to the other spark timings. This speculation was confirmed through combustion visualizations made as discussed next.

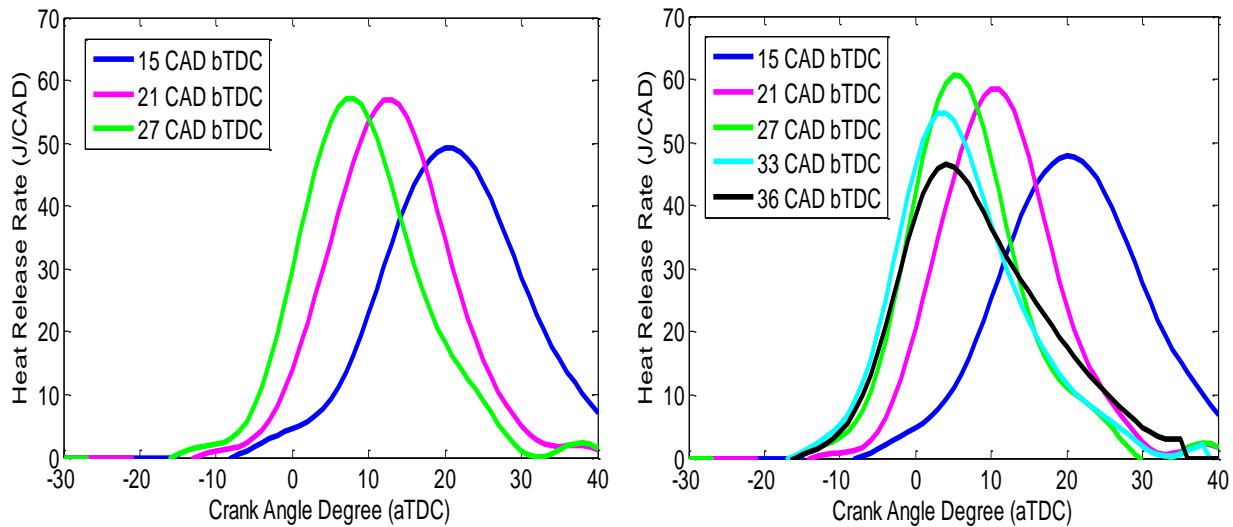


Figure 4.8: Main chamber heat release rates for EFI-1 (left) and EFI-2 (right) injection conditions.

The combustion images recorded for EFI-1 fuel injection condition and the three spark timings in **Figure 4.8** are shown in **Figure 4.9**. The camera was triggered on the onset of spark and hence, the images are arranged with respect to crank angles after spark initiation. It was observed that the reacting jet entered the main chamber earlier with retarded spark timing; spark at 15 CAD bTDC showed jets in the images starting from 10.8 CADs aSPI. However, the burn duration 0 to 10% in the main chamber was determined to be 6 CADs longer with spark at 15 CAD bTDC compared to that at 27 CAD bTDC. This observation supports the earlier speculation that the retarded spark condition took longer to initiate combustion in the main chamber for the same EGR % implemented. Later stages of combustion showed a flame of golden-yellow color in the

high speed images. The total amount of fuel injected in these EGR-diluted conditions was higher than for conditions without EGR. The higher fuel content and lower intake oxygen could have resulted in fuel-rich combustion (soot precursor C_2^* emission at visible wavelengths). On the other hand, the near-stoichiometric combustion temperatures with high nitrogen dilution could have resulted in oxides of nitrogen such as NO_2 (dark brown) or N_2O_4 (light brown). Further optical investigations are required to identify soot formation as well as to quantify the exhaust soot content after soot oxidation possible during expansion and exhaust strokes. Chemiluminescence studies might reveal the presence of oxides of nitrogen at the end of main chamber combustion.

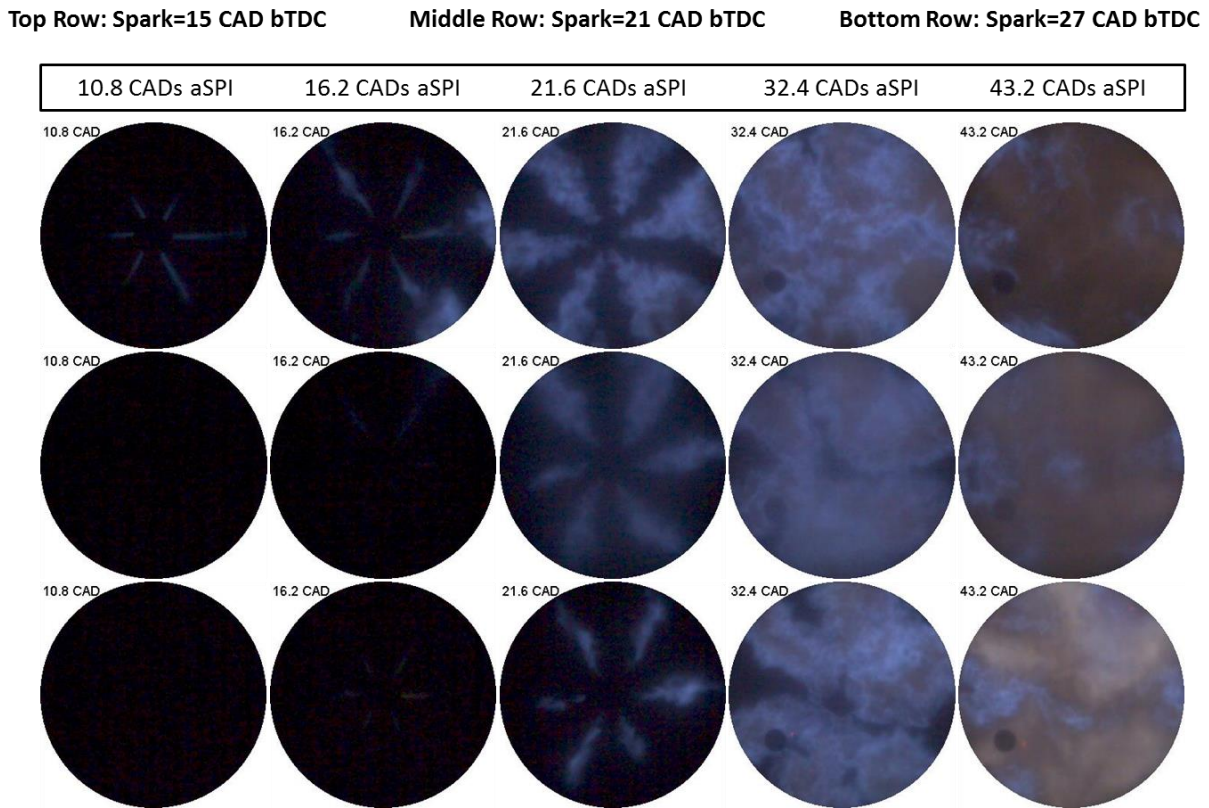


Figure 4.9: Main chamber combustion images for three different spark timings.

4.3.3 Thermal Efficiency of the DM-TJI Engine

Previously, the DM-TJI engine having a compression ratio of 9.5 resulted in an unthrottled part-load indicated efficiency of $42.0\% \pm 1\%$ (including air pump work). The current DM-TJI engine of compression ratio 12.0 resulted in an indicated efficiency of $46.0\% \pm 1\%$, an increase of 4% compared to the low compression ratio engine. Similar to this outcome, Zheng et al. [109] noted an increase of 3.9% in the thermal efficiency when switched from 9.3 to 12.0 compression ratio. It should be noted that the $\pm 1\%$ mentioned in the efficiency value for the 12.0 compression ratio engine is related to fuel injector calibrations. The main chamber fuel injector calibrations conducted twice showed an injected fuel mass difference that lead to a 2% difference in the indicated efficiency. Hence, the efficiency values are written by including a $\pm 1\%$ value.

The remarkable efficiency delivered by the DM-TJI engine of compression ratio 12.0 might be appreciated better when benchmarked with other current single-cylinder light duty engines as shown in **Table 4.3**. These engine works were selected based on the following requirements.

- Gasoline being the primary fuel.
- Engine was operated under unthrottled, part-load conditions with or without EGR.
- Displacement volume was less than 1 L because the DM-TJI has a value of ~ 0.71 L (including pre-chamber volume).

As seen here, majority of these works employed a geometric compression ratio significantly greater than 12.0. Another common observation among these works is the utilization of boosted intake that ranged from 1.5 bar to greater than 2.5 bar intake absolute pressure. The maximum EGR dilution of approximately 41% was observed with the reactivity-controlled compression ignition technique [110, 111]. Kokjohn et al. [146] utilized RCCI on an engine with a compression ratio of 15.24. Interestingly, the same work showed the highest reported indicated efficiency

(49.5%) among this list, even with such high EGR levels. On the other hand, the DM-TJI engine showed high efficiency with the least compression ratio employed amongst this list, and without intake boosting. The 2000 rpm condition for this engine was tested elsewhere and is included in **Table 4.3** to be consistent with the engine speed of other works listed here.

Table 4.3: Reported Efficiencies of Single-Cylinder Light Duty Engines (displacement <1 L)

	CR*	Engine Speed (rpm)	EGR (%)	Intake Mode	IMEP (bar)	Indicated Efficiency (%)
Honda's Single-Cylinder Engine [112]	17.00	2000	>30	Boosted (>2.50 bar)	8.0 (BMEP)	45.0 (brake)
PCCI [113] (Original work reported IMEP and fuel mg/cycle)	16.10	2000	0	Boosted (1.48 bar)	7.0	45.5 (after subtracting PMEP)
RCCI [110] (~84% gasoline; ~16% diesel DI)	15.24	1900	41	Boosted (1.86 bar)	9.0	49.5
RCCI [111] (82.8% gasoline; 17.2% diesel DI)	15.00	1500	~41	Boosted (1.50 bar)	6.8	~37.5
SACI [114]	12.50	2000	~37	Compressed air (1.05 bar)	6.0	46.2
DM-TJI**	12.00	2000	0	Naturally Aspirated	7.4	47.0±1
		1500	0		6.0	46.0±1
		1500	~30	(~0.95 bar)	7.7	46.6±1

* These values represent the geometric compression ratios. Based on the IVC timing, the effective compression ratios could be different.

** The DM-TJI efficiency values include the work required to pump air to the pre-chamber.

Based on different tests conducted in this work, the most favorable operating conditions for the DM-TJI engine at 1500 rpm are shown in **Table 4.4**. These operating conditions were identified to satisfy the requirements of (i) delivering high thermal efficiency and (ii) result in an exhaust O₂ % that is representative of near-stoichiometric combustion.

Table 4.4: Most Favorable Operating Conditions for the DM-TJI Engine at 1500 rpm

Spark (CAD bTDC)	PC. Fuel (ms)	PC. Fuel Timing (CAD aTDC)	PC. Air Duration (ms)	MC. Fuel (ms)	EGR %	IMEP (bar)	COV IMEP (%)	Exhaust O ₂ %	Estimated Indicated Efficiency
27	1.20	-120	1.60	5 x 1.00	30%	7.71	1.30	0.91%	46.62%
30	1.20	-160	1.60	5 x 1.00	30%	7.70	1.01	0.90%	46.55%
26	1.00	-160	2.00	5 x 1.00	32%	7.62	1.84	0.52%	46.06%

4.4 SUMMARY

The Dual-Mode TJI engine with a high compression ratio of 12.0 was tested without and with nitrogen-simulated EGR dilution.

- *Without EGR dilution:* For middle fuel injection condition, advancing the spark to 25 CAD bTDC resulted in highest peak heat release rate and indicated efficiency. With the spark timing set to this value, the pre-chamber ignited faster with early fuel injection condition compared to middle and later fuel injection conditions. Also, the early injection condition resulted in the highest indicated thermal efficiency of 46.00% at 1500rpm/6.0 bar IMEP for a global $\lambda \cong 1.85$.
- *With EGR dilution:* EGR-diluted conditions showed several misfires in the main chamber and/or the pre-chamber without air injection in the pre-chamber. For the same EGR dilution levels, no misfires were detected by including pre-chamber air injection. To enhance combustion stability, a high-energy ignition coil was employed for the

remaining EGR dilution testing. Although, the IMEP value increased with the amount of fuel injected in the main chamber, the indicated efficiency decreased with increased fuel pulse width. With 25% EGR, the condition with largest fuel pulse width for the main chamber showed combustion phasing close to compression TDC, indicating higher compression work and heat losses during combustion, and thus less efficiency. With 30% EGR and the pre-chamber fuel injection at 120 CAD bTDC, the indicated efficiency increased with spark advance. However with the pre-chamber injection at 160 CAD bTDC and the same 30% EGR, the maximum spark advance resulted in lower efficiency due to the lower heat release rate. For a given EGR %, a retarded spark timing is believed to delay the main chamber ignition and flame propagation. This was attributed to longer mixing times before spark, thereby resulting in locally lean mixtures in the main chamber.

- An earlier pre-chamber ignition time, a lower pre-chamber pressure before reaching its first peak, and a lower main chamber peak pressure resulted in high indicated efficiency. Thus, developing combustion phenomenon that leads to less heat losses in both pre-chamber and main chamber could be an effective strategy in improving engine thermal efficiency.
- The current work shows significant improvement of EGR dilution tolerance of the DM-TJI system over a conventional TJI system (without pre-chamber air and fuel injection). With the developed DM-TJI engine, stoichiometric mixture created using large amounts of exhaust gas recirculation (EGR ~32%) provided an indicated efficiency greater than 45% at low-mid loads. It should be noted that this efficiency includes work required to supply high-pressure air to the pre-chamber. With this operating condition,

a conventional three-way catalytic converter can be employed to handle gaseous emissions, making this technology viable with the current state-of-art aftertreatment technology.

CHAPTER 5

Concluding Remarks

The thermal efficiency and emission standards of gasoline engines can be further improved to meet the future environmental regulations. An advanced gasoline combustion technology called dual-mode turbulent jet ignition (DM-TJI) was developed and tested. The lean flammability limits of gasoline with DM-TJI were investigated using iso-octane/air ignition delay study in an optically accessible rapid compression machine. A unique feature of the DM-TJI technology is to separately supply air to the pre-chamber. Providing pre-chamber air injection pulse during the pre-chamber fuel injection event enhanced the combustion burn rates under certain injection timings and mitigated particulate formation. For an early pre-chamber fuel injection timing, an air injection pressure of 200 psi is offered the fastest penetrating jet (reliable ignition source), relatively longer main chamber ignition time (avoids particulate formation), and rapid 10-90% burn duration (increases indicated work and avoids accumulation modes or soot). Combustion visualizations conducted with the DM-TJI optical engine of compression ratio 9.5 showed that the low-pressure injector used for fueling the main chamber resulted in droplet burning due to improper fuel atomization. By using a high-pressure injector for main chamber, the engine delivered an estimated indicated efficiency of greater than 42% at 1500rpm/6 bar IMEP speed/load conditions. The DM-TJI engine with a higher compression ratio of 12.0 showed the pre-chamber ignited faster with an early fuel injection condition. Also, this injection condition resulted in the highest indicated thermal efficiency of 46.00% at 1500rpm/6.0 bar IMEP for a global $\lambda \cong 1.85$. The capability of DM-TJI technology to extend the EGR dilutions levels was evident by the misfires detected when there was no air injection in the pre-chamber. For a given EGR %, a retarded spark timing is believed to delay the main chamber ignition and flame propagation. This was attributed to longer

mixing times before spark, thereby resulting in locally lean mixtures in the main chamber. Combustion phenomenon that leads to less heat losses in both pre-chamber and main chamber is believed to be an effective means to improve the engine thermal efficiency. With the developed DM-TJI engine, near-stoichiometric combustion using nitrogen-simulated EGR ~32% provided an indicated efficiency greater than 45% at engine part-load operation.

APPENDIX

APPENDIX

A Purge Pump System to Scavenge Residuals in the Pre-chamber of Turbulent Jet Ignition Engine

A-1 SYNOPSIS

From previous chapters, the advantage of having an air injection in the pre-chamber is evident. The DM-TJI design currently being employed requires another high-pressure injector implicating higher costs. A “Purge Pump System” was designed by MSU as an alternative solution to supply air to the pre-chamber. This section covers a numerical analysis of the purge pump system performed using one-dimensional code (Gamma Technologies: GT-Power). The GT engine simulation code is based on 1-D gas-dynamic models for flow calculation and thermodynamic models for combustion characterization. The main objectives of this analysis are

- To understand the pressure wave dynamics influenced by adding a purge pump system to the Turbulent Jet Ignition Engine.
- To estimate the amount of work required to operate the proposed purge pump.

A-2 PURGE PUMP SYSTEM

A-2.1 Conceptual Description

Pumping air to the high pressures required for delivery through injector holes several hundred microns in size produce an unrestrained expansion that will be energy-intensive. As an alternative to the high-pressure air injector in the pre-chamber, another option was developed by MSU which addresses the key technical issues required for successful execution of the dual-mode turbulent jet ignition concept with production-demonstrated components. This system permits independent control of fuel and air delivery to the pre-chamber with a single, commercially available direct injector supplying fuel to the pre-chamber as shown in **Figure A.1**. Fresh air is

supplied to the pre-chamber through a poppet valve. This concept is referred to as the DM-TJIv concept, with v standing for valve. Although not previously used in a TJI system, all of the DM-TJIv components have been used in production engines. The system consists of a small pre-chamber air supply poppet valve driven by a low-energy-consuming camshaft and a lost motion lifter providing timing control for this valve. The air pump is shown and although it may not be located in this position, it is an important component whose power consumption is analyzed in this work.

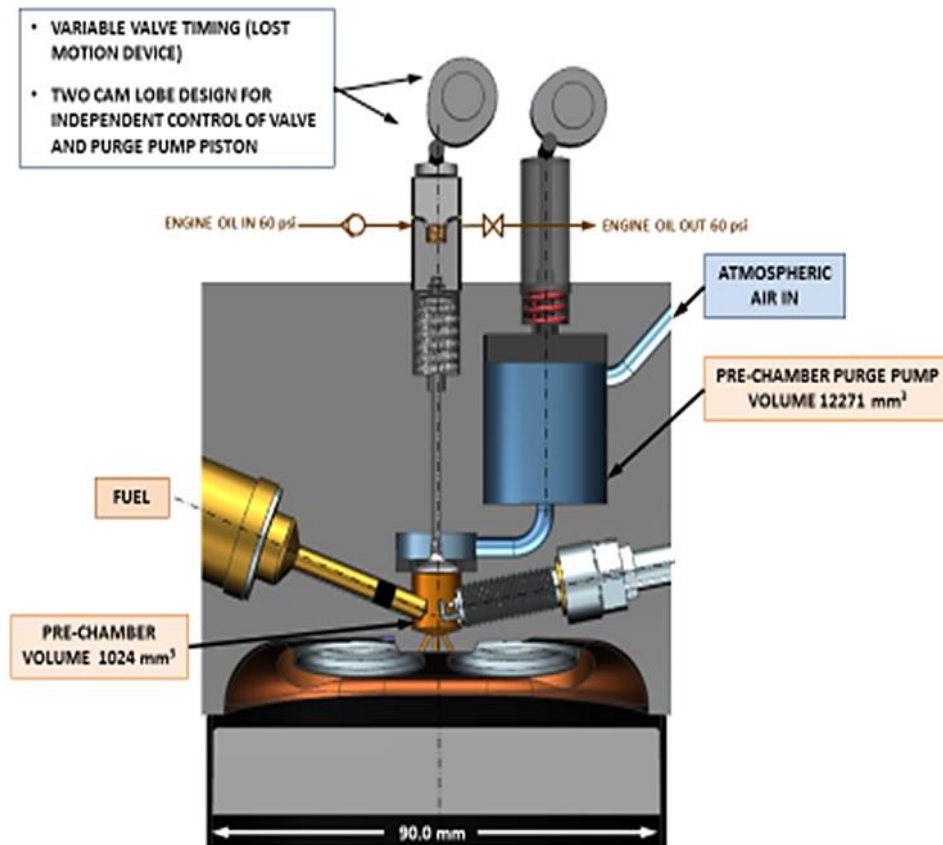


Figure A.1: DM-TJIv concept with air supplied through a camshaft-controlled poppet valve (figure taken from patent disclosure).

A-2.2 Numerical Model Description

A schematic of the DM-TJIv concept for air supply to the pre-chamber is shown in **Figure A.2a**. A segment of the GT-Power model showing the corresponding components of the purge pump system is included in **Figure A.2b**. The engine and the purge system model specifications are listed in **Table A.1** and respectively. It should be noted that the 0 CAD here represents TDC compression.

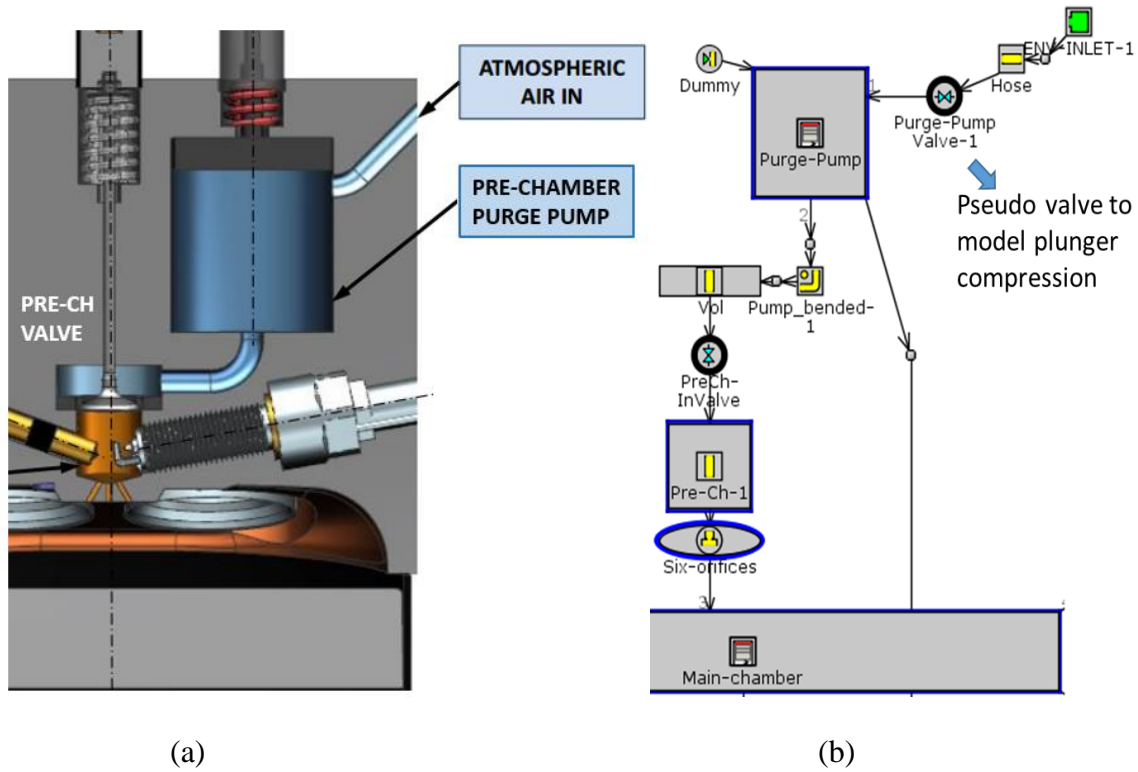


Figure A.2: (a) Cam-driven purging system; (b) a section of the numerical model showing the corresponding purging system.

Table A.1: DM-TJI Engine Model Specifications

Bore	95 mm
Stroke	100 mm
Connecting rod length	190 mm

Table A.1 (cont'd)

Compression Ratio	10:1
Pre-chamber	1024 mm ³
Main chamber swept volume	0.709 L
Fuel	Gasoline (main chamber)
Operating Speed	1500 rpm

Table A.2: Purge System Model Specifications

Plunger Diameter	13 mm, 30 mm, 60 mm
Plunger Swept Volume	3185, 16965, 67860 mm ³
Compression Ratio	12:1
PURGE PUMP VALVE: Valve Timings Max. Valve Lift	IVO = 180 CAD aTDC IVC = 540 CAD aTDC 3 mm
PRE-CHAMBER VALVE: Valve Timings Max. Valve Lift	IVO = 360 CAD aTDC IVC = 78 CAD bTDC 5.6 mm

The purge pump was modeled using a ‘cylinder’ object with the two strokes that occurred during compression and expansion strokes of the main chamber. An ‘EngCylGeomUser’ (GT-Power object name) was employed to model the unconventional piston/plunger motion as shown in **Figure A.3**. Notice that the plunger remains at top (position = -24 mm) during exhaust and

intake strokes, as the cam lobe detaches from the plunger in this duration. A pseudo valve was introduced in the model to simulate the inflow and compression in the purge pump. The opening and closing times of this purge pump valve were chosen in accordance with the plunger position profile. As GT-POWER requires an injector object to be connected to any cylinder object, a “dummy” injector was connected to the purge pump without any fuel mass injected. The pre-chamber valve was modeled such that the valve opens at the start of intake stroke and closes near the pre-chamber fuel injection timing that occurred at 80 CAD BTDC during compression stroke in the actual engine experiments. For the current modeling work, no combustion was imposed in the pre-chamber and the initial state was assigned with either ambient air or selected percentages of combustion gases (including nitrogen) to simulate EGR composition.

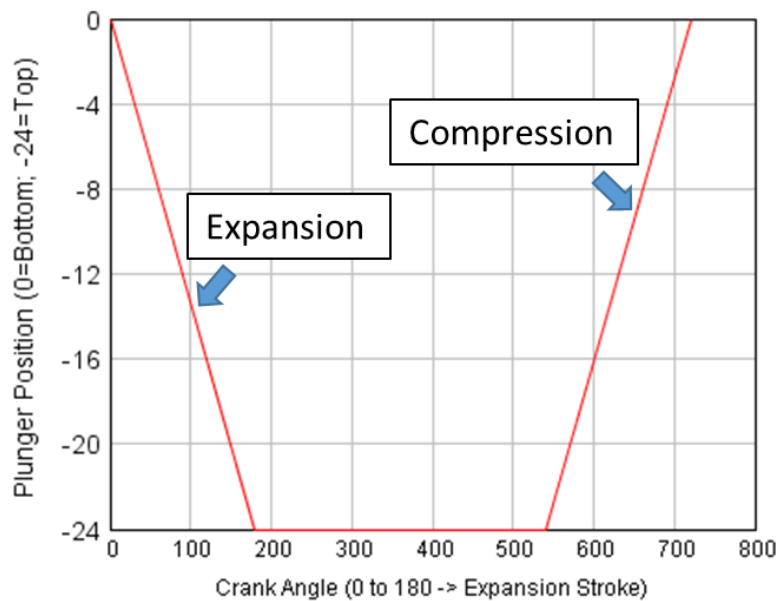


Figure A.3: Plunger position profile in an engine cycle.

A-3 NUMERICAL APPROACH TO ESTIMATE PURGE PUMP WORK

The complete model of the TJI concept-based engine with the proposed purge system is shown in **Figure A.4**. Three cases with different purge pump volumes were investigated by

changing the plunger diameter. The reduction in the backflow that would occur due to pressure difference between the pre-chamber and the purge system regions determines the efficacy of the proposed purge pump. To this effect, the parameters of interest were:

- mass flow rate through the pre-chamber valve
- mass fraction of major burned species (CO_2) in the pre-chamber, and
- mass fraction of CO_2 in the 'vol' object that was located above the pre-chamber valve.

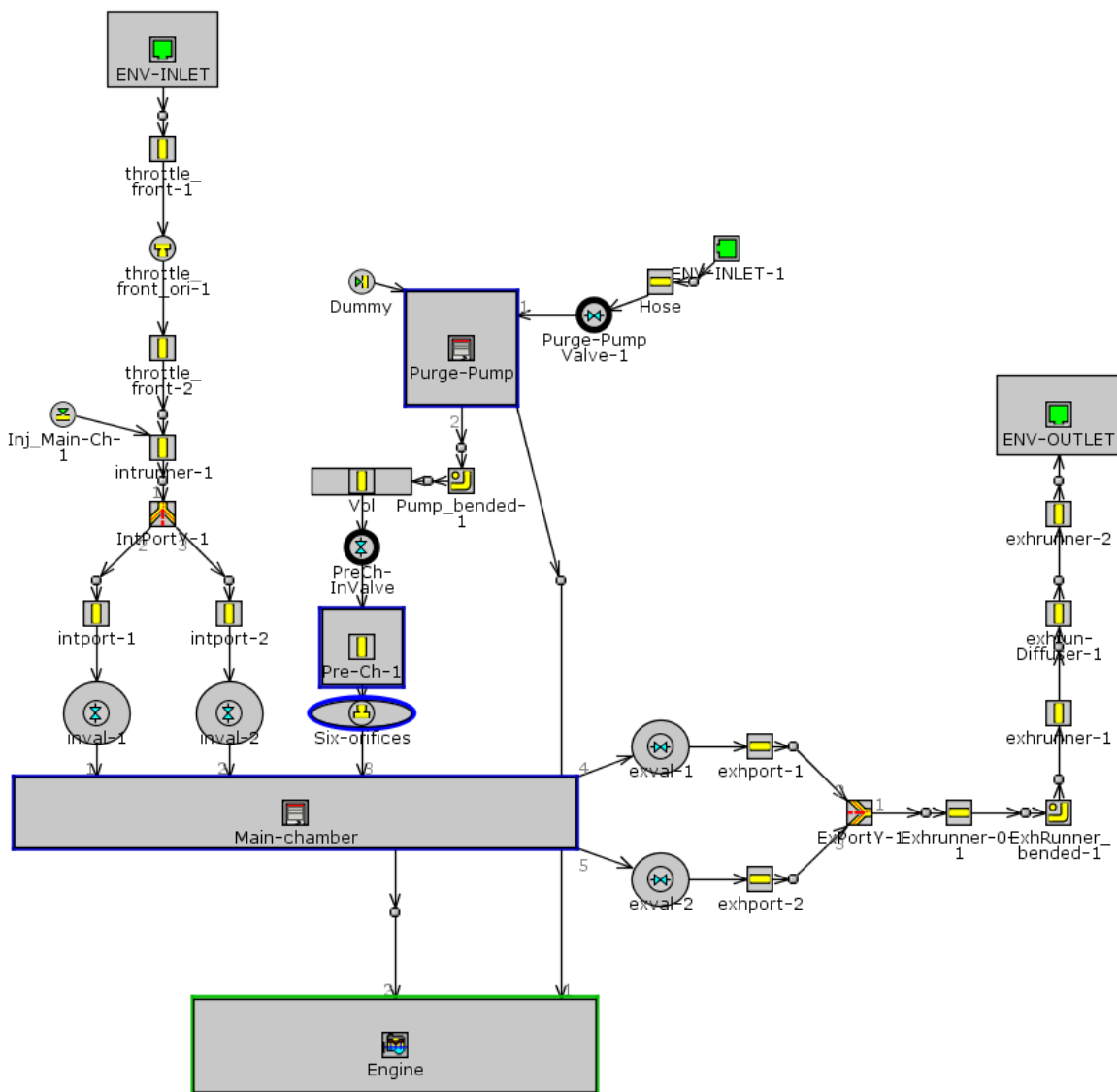


Figure A.4: GT – Power model schematic of the DM-TJIV engine.

Default flow convergence settings were used, and the maximum pressure in the main chamber was chosen as the convergence RLT variable with a steady-state tolerance of 0.1 bar. Recall that there is no combustion model in the pre-chamber for the current investigations, and any burned species observed from the combustion in the main chamber. The combustion in the main chamber was modeled using a Wiebe function with a CA50 of 6.2 CAD ATDC and a 10-90 burn duration of 28 CADs, as noted during DM-TJI engine experiments at MSU. The port fuel injector for the main chamber was modeled using a multiple pulse injection connection, and the main chamber fuel amounts used in the model were calibrated during the DM-TJI engine experiments.

A-4 RESULTS AND DISCUSSION

A-4.1 Ability of Purge Pump to Scavenge Residuals

To ensure that the simulated results were reasonable, a comparison of the experimentally measured main chamber pressure in a DM-TJI engine and the pressure as calculated by the model during combustion is shown in **Figure A.5**. Pressures from the simulation and experiment seem to be well correlated with a slight deviation near the end of power stroke. The engine experiments used a two-injector approach and the model used the proposed DM- TJIv concept. This model is believed to adequate for realistic performance of an idealized purge pump.

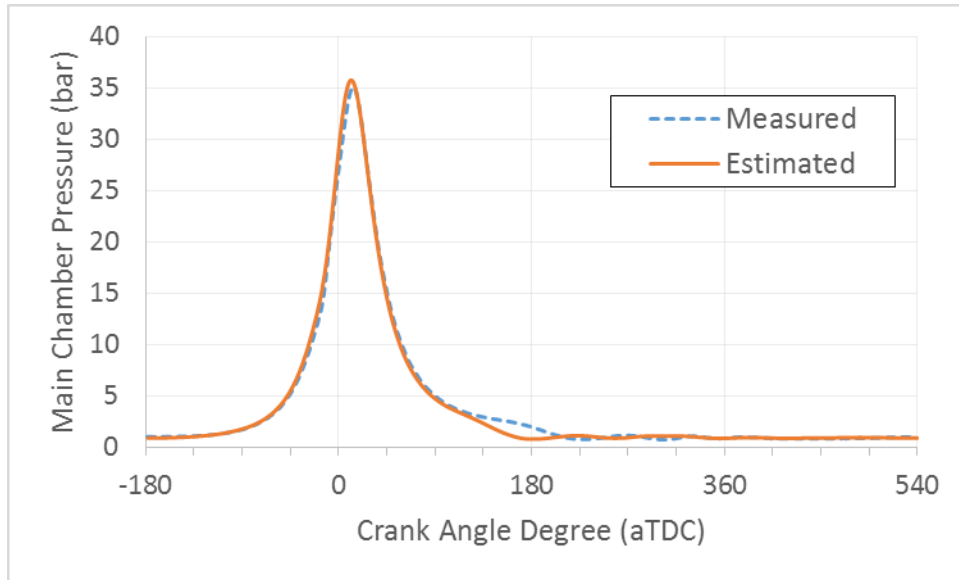


Figure A.5: Plot comparing the measured and calculated pressure traces in the main chamber during firing cycle.

Three cases were studied by changing the range of plunger diameters for the idealized purge pump. They were:

- CASE 1: Volume of the purge pump = 3185 mm (about 33% of pre-chamber volume).
- CASE 2: Volume of the purge pump = 16965 mm (about 150% of pre-chamber volume).
- CASE 3: Volume of the purge pump = 67860 mm (about 500% of pre-chamber volume).

The mass flow rates at the pre-chamber valve for these three cases are shown in **Figure A.6**. All the purge pump volumes showed a positive mass flow rate, i.e. flow leaving the pre-chamber and entering the main chamber during the intake stroke. Based on the prior knowledge of pressure levels in the system during the intake stroke, the proposed purge system is designed such that the plunger rests at the top position while allowing influx of ambient air into the pre-chamber through the opened pre-chamber valve. However, the extent to which the pre-chamber valve is

open during compression would be the determining factor for the selection of a suitable purge pump. As seen in **Figure A.6**, a larger purge pump resulted in higher forward flow discharge from the pre-chamber valve during the early compression. An interesting observation as highlighted in the rectangular box of **Figure A.6** is that the backflow with purge pump #2 was higher than with the smaller purge pump #1. This was found to be a wave dynamic effect and illustrates the importance of understanding the details of flow in the system.

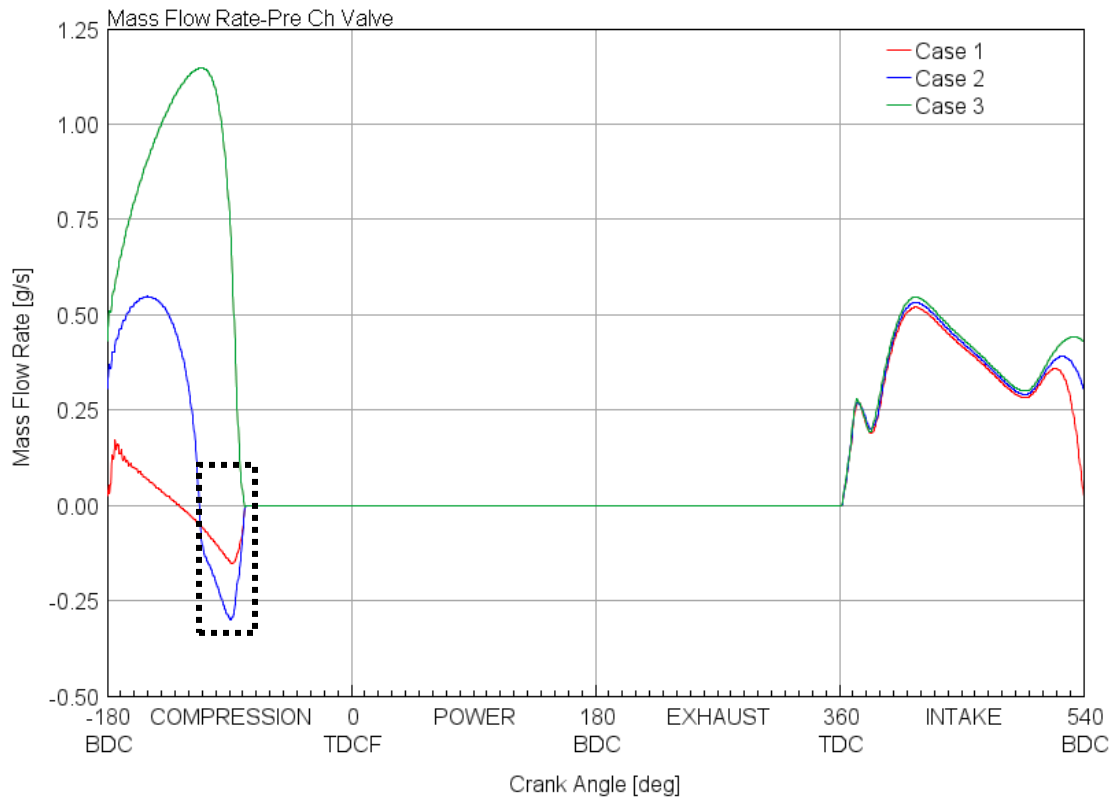
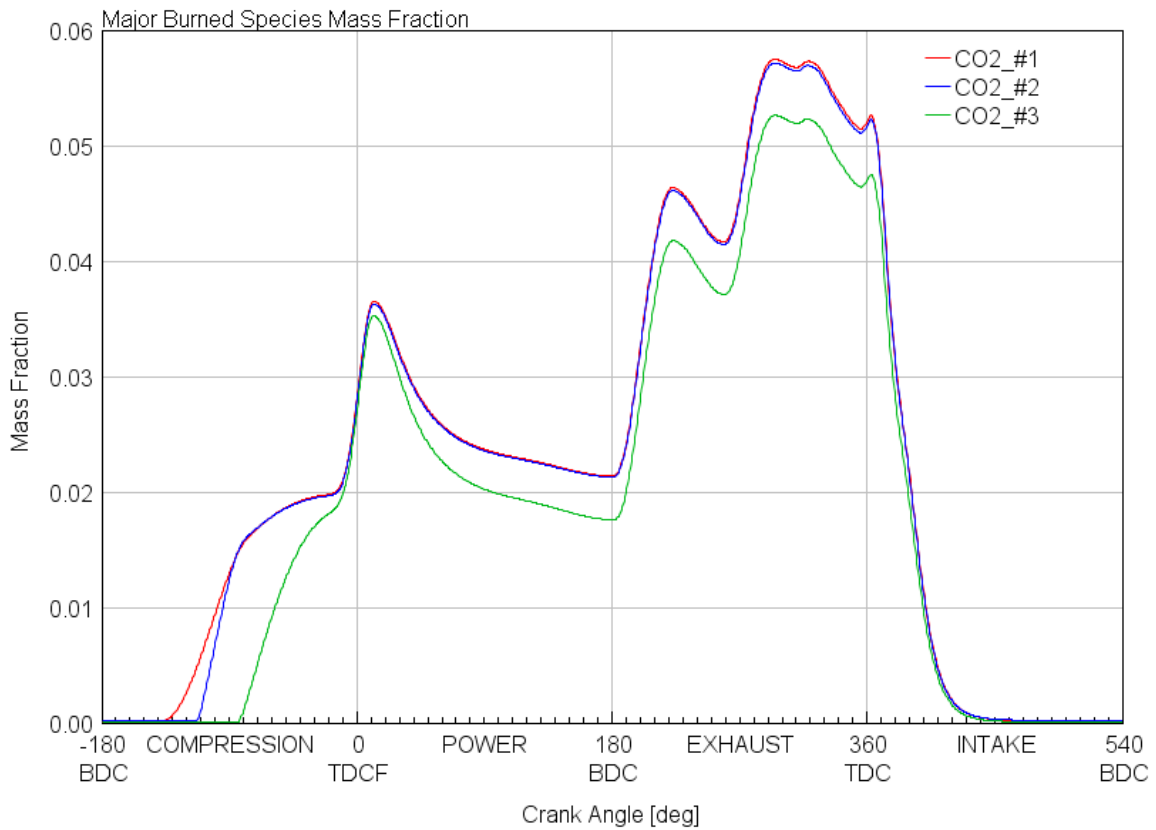


Figure A.6: Mass flow rate at the pre-chamber valve for different purge pump volumes.

Figure A.7, diagrams (a-b) show the mass fractions of CO₂ in the pre-chamber and the Vol object that was located above the pre-chamber valve. On looking at the mass fractions in the pre-chamber, the following observations can be made. First, the mass fraction of the burned gas from the main chamber was overall lower in case #3 than in the other two cases. The mass fraction

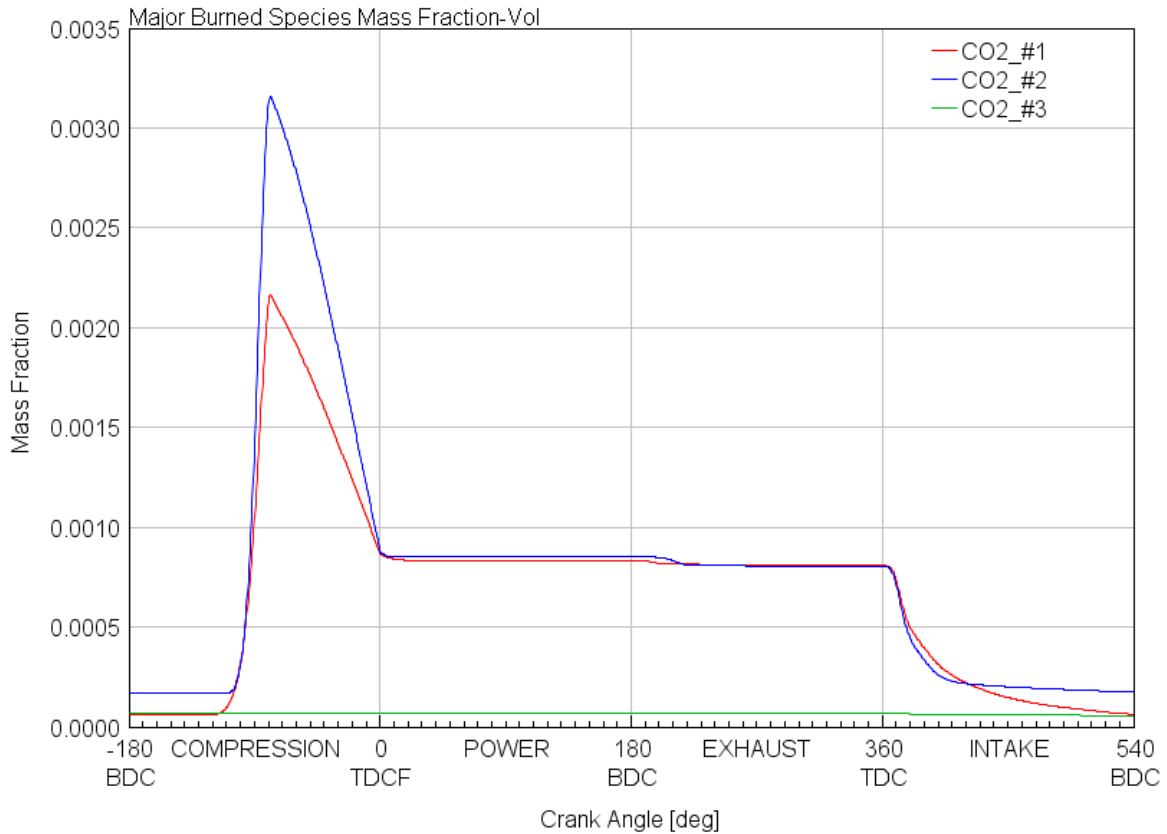
of CO₂ near the pre-chamber valve closure was an order of magnitude higher with cases #1 and #2 when compared to that with case #3. Secondly, a non-zero mass fraction value showed up later (in the compression stroke) as the purge pump volume was increased. When the mass fractions in the ‘Vol’ object are examined, one can see that the mass fraction with case #2 was highest, followed by cases #1 and #3 respectively. Hence, the purge pump in case #3 is capable of suppressing backflow from the pre-chamber to the purge system.



(a)

Figure A.7: Major burned species mass fractions for the three cases in (a) Pre-chamber and (b) Vol object (above pre-chamber valve).

Figure A.7 (cont'd)



(b)

A-4.2 Work Required to Run these Pumps

After a preliminary study of the flow physics of the system, the pressure-volume diagram was used to obtain the indicated mean effective pressure values for the purge pump and the main chamber as listed in **Table A.3**. The work required to run these pumps was calculated as the product of the indicated mean effective pressure and the swept volume. One may recall, during the intake stroke of the engine, purging is accomplished with almost no work except for small flow losses; and during compression the purge pump valve was closed prior to fuel being injected into the purge chamber.

Table A.3: Mean Effective Pressures (bar) in the Purge Pump and the Main chamber

	Case #1	Case #2	Case #3
Purge Pump	0.129	0.251	0.268
Main chamber	5.033	5.036	5.050

Then the work required to run these pumps could be estimated as the product of pressure and the swept volume.

CASE 1: 33% Pre-chamber Purge

Work required to run the purge pump = $0.129 \times 3185 = 4.16 \times 10^{-5}$ kJ

Work produced from the main chamber with the inclusion of this pump = $5.033 \times 7088 = 0.361$ kJ

Hence 0.01 % of work produced in each cycle is needed to run this pump.

CASE 2: 150% Pre-chamber Purge

Work required to run the purge pump = $0.251 \times 16965 = 4.31 \times 10^{-4}$ kJ

Work produced from the main chamber with the inclusion of this pump = $5.036 \times 7088 = 0.362$ kJ

Hence 0.1 % of work produced in each cycle is needed to run this pump.

CASE 3: 500% Pre-chamber Purge

Work required to run the purge pump = $0.268 \times 67860 = 0.002$ kJ

Work produced from the main chamber with the inclusion of this pump = $5.05 \times 7088 = 0.363$ kJ

Hence 0.51 % of work produced in each cycle is needed to run this pump.

A detailed experimental and computational analysis will be required to determine the pre-chamber purge required at various operating conditions. Having said that, it is clear that even with a large pre-chamber purge of 500%, the estimated work requirement is modest at this operating point (1500 RPM, ~6 bar IMEP). With additional flow and friction losses in the purging system not

accounted for in the simulation, an estimate of a 1% efficiency reduction due to pre-chamber purge is reasonable at this operating condition.

REFERENCES

REFERENCES

1. Guzzella, L. and C. Onder, *Introduction to modeling and control of internal combustion engine systems*. 2009: Springer Science & Business Media.
2. Jo, Y.S., et al., *Performance Maps of Turbocharged SI Engines with Gasoline-Ethanol Blends: Torque, Efficiency, Compression Ratio, Knock Limits, and Octane*, 2014, SAE Technical Paper.
3. Pana, C., N. Negurescu, and A. Cernat. *Improvement of the automotive spark ignition engine performance by supercharging and the bioethanol use*. in *Proceedings of the FISITA 2012 World Automotive Congress*. 2013. Springer.
4. Ramadhas, A., S. Jayaraj, and C. Muraleedharan, *Use of vegetable oils as IC engine fuels—a review*. *Renewable energy*, 2004. **29**(5): p. 727-742.
5. Lanjewar, P.B., R. Rao, and A. Kale, *Assessment of alternative fuels for transportation using a hybrid graph theory and analytic hierarchy process method*. *Fuel*, 2015. **154**: p. 9-16.
6. Kleeberg, H., et al., *Increasing Efficiency in Gasoline Powertrains with a Two-Stage Variable Compression Ratio (VCR) System*, 2013, SAE Technical Paper.
7. Constensou, C. and V. Collee, *VCR-VVA-High Expansion Ratio, a Very Effective Way to Miller-Atkinson Cycle*, 2016, SAE Technical Paper.
8. Goswami, A., S. Vashist, and A. Nayyar, *Effect of Compression Ratio on the Performance Characteristics of Spark Ignition Engine Fueled with Alternative Fuels: A Review*, 2015, SAE Technical Paper.
9. Groff, E.G., *Automotive Direct-Injection Stratified-Charge Engine Development in the 1970-1980's*, 2016, SAE Technical Paper.
10. Zhao, F.-Q., M.-C. Lai, and D.L. Harrington, *A review of mixture preparation and combustion control strategies for spark-ignited direct-injection gasoline engines*, 1997, SAE Technical Paper.
11. Alkidas, A.C., *Combustion advancements in gasoline engines*. *Energy Conversion and Management*, 2007. **48**(11): p. 2751-2761.
12. Fiengo, G., et al., *Basic Concepts on GDI Systems*, in *Common Rail System for GDI Engines*. 2013, Springer. p. 17-33.

13. Drake, M. and D. Haworth, *Advanced gasoline engine development using optical diagnostics and numerical modeling*. Proceedings of the Combustion Institute, 2007. **31**(1): p. 99-124.
14. Harada, J., et al., *Development of direct injection gasoline engine*, 1997, SAE Technical Paper.
15. Zigan, L., et al., *Structure of evaporating single-and multicomponent fuel sprays for 2nd generation gasoline direct injection*. Fuel, 2011. **90**(1): p. 348-363.
16. Park, C., et al., *Stratified lean combustion characteristics of a spray-guided combustion system in a gasoline direct injection engine*. Energy, 2012. **41**(1): p. 401-407.
17. Fansler, T.D., et al., *Invited Review: Combustion instability in spray-guided stratified-charge engines: A review*. International Journal of Engine Research, 2015. **16**(3): p. 260-305.
18. Vent, G., et al. *The new 2.0 l turbo engine from the Mercedes-Benz 4-cylinder engine family*. in *21st Aachen Colloquium Automobile and Engine Technology*. 2012.
19. Oh, H., et al., *Effect of the multiple injection on stratified combustion characteristics in a spray-guided DISI engine*, 2011, SAE Technical Paper.
20. Banerjee, R. and S. Kumar, *Numerical investigation of stratified air/fuel preparation in a GDI engine*. Applied Thermal Engineering, 2016. **104**: p. 414-428.
21. Maricq, M.M., et al., *Particulate emissions from a direct-injection spark-ignition (DISI) engine*, 1999, SAE Technical Paper.
22. Zhang, S. and W. McMahon, *Particulate emissions for LEV II light-duty gasoline direct injection vehicles*. SAE International Journal of Fuels and Lubricants, 2012. **5**(2012-01-0442): p. 637-646.
23. Zhu, R., et al., *Tailpipe emissions from gasoline direct injection (GDI) and port fuel injection (PFI) vehicles at both low and high ambient temperatures*. Environmental Pollution, 2016. **216**: p. 223-234.
24. Toulson, E., H.J. Schock, and W.P. Attard, *A review of pre-chamber initiated jet ignition combustion systems*, 2010, SAE Technical Paper.
25. Turkish, M.C., *3-Valve Stratified Charge Engines: Evolvement, Analysis and Progression*, 1974, SAE Technical Paper.
26. Noguchi, M., S. Sanda, and N. Nakamura, *Development of Toyota lean burn engine*, 1976, SAE Technical Paper.
27. Adams, T.G., *Torch Ignition for combustion control of lean mixtures*, 1979, SAE Technical Paper.

28. Brandstetter, W., *The Volkswagen Lean Burn PC-Engine Concept*, 1980, SAE Technical Paper.
29. Date, T., et al., *Research and development of the Honda CVCC engine*, 1974, SAE Technical Paper.
30. Latsch, R., *The swirl-chamber spark plug: a means of faster, more uniform energy conversion in the spark-ignition engine*, 1984, SAE Technical Paper.
31. Alfonso, J.D. and H. Kersting, *Spark plug, in particular swirl chamber spark plug*, 2015, Google Patents.
32. Dikeman, M.J., *Ignition flash plug*, 1926, Google Patents.
33. Tozzi, L.P. and D.W. Salter, *Pre-chamber spark plug*, 2010, Google Patents.
34. Chiera, D., et al. *Lean Limit Extension for High BMEP Gas Engines via Novel Electronic Ignition and Prechamber Plug: Higher Efficiency and Lower NO_x in Open Chamber Engines*. in *ASME 2011 Internal Combustion Engine Division Fall Technical Conference*. 2011. American Society of Mechanical Engineers.
35. Oppenheim, A.K., *Combustion in Piston Engines: Technology, Evolution, Diagnosis and Control*. 2004: Springer.
36. Dainton, L., *Nikolai Nikolaevich Semenov. 16 April 1896-25 September 1986*. Biographical Memoirs of Fellows of the Royal Society, 1990. **36**: p. 527-546.
37. Abramovich, G.D. and G.L. Abramovich, *Internal combustion engine with jet ignition of a non-uniformly distributed working mixture from a precombustion chamber cut-off by the piston*, 1966, Google Patents.
38. Gussak, L., M.C. Turkish, and D.C. Siegla, *High chemical activity of incomplete combustion products and a method of prechamber torch ignition for avalanche activation of combustion in internal combustion engines*, 1975, SAE Technical Paper.
39. Maxson, J. and A. Oppenheim. *Pulsed jet combustion—key to a refinement of the stratified charge concept*. in *Symposium (International) on Combustion*. 1991. Elsevier.
40. Murase, E., et al., *Pulsed combustion jet ignition in lean mixtures*, 1994, SAE Technical Paper.
41. Attard, W.P., et al., *A turbulent jet ignition pre-chamber combustion system for large fuel economy improvements in a modern vehicle powertrain*. SAE International Journal of Engines, 2010. **3**(2010-01-1457): p. 20-37.
42. Ellies, B., C. Schenk, and P. Dekraker, *Benchmarking and Hardware-in-the-Loop Operation of a 2014 MAZDA SkyActiv 2.0 L 13: 1 Compression Ratio Engine*, 2016, SAE Technical Paper.

43. Ingram, A. *Toyota Gasoline Engine Achieves Thermal Efficiency Of 38 Percent*. 2014.
44. Takahashi, D., et al., *Combustion development to achieve engine thermal efficiency of 40% for hybrid vehicles*, 2015, SAE Technical Paper.
45. Groote, S.D. *Turbulent Jet ignition pushes engine combustion efficiency*. 2016.
46. Reese, R. *Progress (and Challenges) along the Path to 2025*. in *Engine Research Center 2015 Symposium*. 2015. University of Wisconsin, Madison.
47. Johnson, T., *Vehicular Emissions in Review*. SAE International Journal of Engines, 2016. **9**(2016-01-0919): p. 1258-1275.
48. Stanglmaier, R.H. and C.E. Roberts, *Homogeneous charge compression ignition (HCCI): benefits, compromises, and future engine applications*, 1999, SAE Technical Paper.
49. Epping, K., et al., *The potential of HCCI combustion for high efficiency and low emissions*, 2002, SAE Technical Paper.
50. Ghorbanpour, M. and R. Rasekhi, *A parametric investigation of HCCI combustion to reduce emissions and improve efficiency using a CFD model approach*. Fuel, 2013. **106**: p. 157-165.
51. Tunestål, P., *Optimal Control of HCCI*, in *Optimization and Optimal Control in Automotive Systems*. 2014, Springer. p. 291-300.
52. Dec, J.E. and M. Sjöberg, *A parametric study of HCCI combustion-the sources of emissions at low loads and the effects of GDI fuel injection*, 2003, SAE Technical paper.
53. Hasan, A.O., et al., *HC, CO and NO_x emissions reduction efficiency of a prototype catalyst in gasoline bi-mode SI/HCCI engine*. Journal of Environmental Chemical Engineering, 2016. **4**(2): p. 2410-2416.
54. Aoyama, T., et al., *An experimental study on premixed-charge compression ignition gasoline engine*, 1996, SAE Technical paper.
55. Kalghatgi, G.T., P. Risberg, and H.-E. Angstrom, *Partially pre-mixed auto-ignition of gasoline to attain low smoke and low NO_x at high load in a compression ignition engine and comparison with a diesel fuel*, 2007, SAE Technical Paper.
56. Hanson, R., D. Splitter, and R.D. Reitz, *Operating a heavy-duty direct-injection compression-ignition engine with gasoline for low emissions*, 2009, SAE Technical Paper.
57. Manente, V., et al., *An advanced internal combustion engine concept for low emissions and high efficiency from idle to max load using gasoline partially premixed combustion*, 2010, SAE Technical Paper.

58. Inagaki, K., et al., *Dual-fuel PCI combustion controlled by in-cylinder stratification of ignitability*, 2006, SAE Technical Paper.
59. Splitter, D., R.D. Reitz, and R. Hanson, *High efficiency, low emissions RCCI combustion by use of a fuel additive*. SAE International Journal of Fuels and Lubricants, 2010. **3**(2010-01-2167): p. 742-756.
60. Kokjohn, S., et al., *Fuel reactivity controlled compression ignition (RCCI): a pathway to controlled high-efficiency clean combustion*. International Journal of Engine Research, 2011. **12**(3): p. 209-226.
61. Lavoie, G.A., et al., *A multi-mode combustion diagram for spark assisted compression ignition*. Combustion and flame, 2010. **157**(6): p. 1106-1110.
62. Persson, H., et al., *Study of fuel stratification on spark assisted compression ignition (SACI) combustion with ethanol using high speed fuel PLIF*, 2008, SAE Technical Paper.
63. Johnson, T., *Vehicular emissions in review*. SAE International Journal of Engines, 2013. **6**(2013-01-0538): p. 699-715.
64. Heck, R.M. and R.J. Farrauto, *Automobile exhaust catalysts*. Applied Catalysis A: General, 2001. **221**(1): p. 443-457.
65. Fan, Q. and L. Li, *Study on first-cycle combustion and emissions during cold start in a TSDI gasoline engine*. Fuel, 2013. **103**: p. 473-479.
66. Kreuzer, T., et al., *Advanced exhaust gas aftertreatment systems for gasoline and diesel fuelled vehicles*. Catalysis today, 1996. **29**(1): p. 17-27.
67. Koebel, M., M. Elsener, and G. Madia, *Recent advances in the development of urea-SCR for automotive applications*, 2001, SAE Technical Paper.
68. Farrauto, R.J. and R.M. Heck, *Catalytic converters: state of the art and perspectives*. Catalysis Today, 1999. **51**(3): p. 351-360.
69. Alkemade, U.G. and B. Schumann, *Engines and exhaust after treatment systems for future automotive applications*. Solid State Ionics, 2006. **177**(26): p. 2291-2296.
70. Prikhodko, V.Y., et al., *Ammonia Generation over TWC for Passive SCR NO X Control for Lean Gasoline Engines*. SAE International Journal of Engines, 2014. **7**(2014-01-1505): p. 1235-1243.
71. Masum, B., et al., *Effect of ethanol-gasoline blend on NOx emission in SI engine*. Renewable and Sustainable Energy Reviews, 2013. **24**: p. 209-222.
72. Francqueville, L. and J.-B. Michel, *On the effects of EGR on spark-ignited gasoline combustion at high load*. SAE International Journal of Engines, 2014. **7**(2014-01-2628): p. 1808-1823.

73. Lattimore, T., et al., *Investigation of EGR Effect on Combustion and PM Emissions in a DISI Engine*. Applied Energy, 2016. **161**: p. 256-267.
74. Zhu, G.G., C.F. Daniels, and J. Winkelman, *MBT timing detection and its closed-loop control using in-cylinder pressure signal*, 2003, SAE Technical Paper.
75. Myung, C. and S. Park, *Exhaust nanoparticle emissions from internal combustion engines: A review*. International Journal of Automotive Technology, 2012. **13**(1): p. 9-22.
76. Amaral, S.S., et al., *An Overview of Particulate Matter Measurement Instruments*. Atmosphere, 2015. **6**(9): p. 1327-1345.
77. Maricq, M.M., N. Xu, and R.E. Chase, *Measuring particulate mass emissions with the electrical low pressure impactor*. Aerosol Science and Technology, 2006. **40**(1): p. 68-79.
78. Giechaskiel, B., P. Dilara, and J. Andersson, *Particle measurement programme (PMP) light-duty inter-laboratory exercise: repeatability and reproducibility of the particle number method*. Aerosol Science and Technology, 2008. **42**(7): p. 528-543.
79. Seong, H., K. Lee, and S. Choi, *Effects of engine operating parameters on morphology of particulates from a gasoline direct injection (GDI) engine*, 2013, SAE Technical Paper.
80. Storey, J.M., et al., *Novel characterization of GDI engine exhaust for gasoline and mid-level gasoline-alcohol blends*. SAE International Journal of Fuels and Lubricants, 2014. **7**(2014-01-1606): p. 571-579.
81. Choi, K., et al., *Size-resolved engine exhaust aerosol characteristics in a metal foam particulate filter for GDI light-duty vehicle*. Journal of Aerosol science, 2013. **57**: p. 1-13.
82. Manente, V., et al., *Influence of inlet pressure, EGR, combustion phasing, speed and pilot ratio on high load gasoline partially premixed combustion*, 2010, SAE Technical Paper.
83. Hedge, M., et al., *Effect of EGR on Particle Emissions from a GDI Engine*. SAE International Journal of Engines, 2011. **4**(2011-01-0636): p. 650-666.
84. Piock, W., et al., *Strategies towards meeting future particulate matter emission requirements in homogeneous gasoline direct injection engines*. SAE International Journal of Engines, 2011. **4**(2011-01-1212): p. 1455-1468.
85. Kuroda, H., et al., *The fast burn with heavy EGR, new approach for low NOx and improved fuel economy*, 1978, SAE Technical Paper.
86. Caton, J.A., *The thermodynamic characteristics of high efficiency, internal-combustion engines*. Energy Conversion and Management, 2012. **58**: p. 84-93.
87. Diana, S., et al., *A strategy to improve the efficiency of stoichiometric spark ignition engines*, 1996, SAE Technical Paper.

88. Sjöberg, M. and W. Zeng, *Combined Effects of Fuel and Dilution Type on Efficiency Gains of Lean Well-Mixed DISI Engine Operation with Enhanced Ignition and Intake Heating for Enabling Mixed-Mode Combustion*. SAE International Journal of Engines, 2016. **9**(2016-01-0689): p. 750-767.
89. Sevik, J., et al., *Extending Lean and Exhaust Gas Recirculation-Dilute Operating Limits of a Modern Gasoline Direct-Injection Engine Using a Low-Energy Transient Plasma Ignition System*. Journal of Engineering for Gas Turbines and Power, 2016. **138**(11): p. 112807.
90. Attard, W.P. and H. Blaxill, *A lean burn gasoline fueled pre-chamber jet ignition combustion system achieving high efficiency and low nox at part load*, 2012, SAE Technical Paper.
91. Biswas, S. and L. Qiao, *Prechamber Hot Jet Ignition of Ultra-Lean H₂/Air Mixtures: Effect of Supersonic Jets and Combustion Instability*. SAE International Journal of Engines, 2016. **9**(2016-01-0795).
92. Bunce, M., et al., *The effects of turbulent jet characteristics on engine performance using a pre-chamber combustor*, 2014, SAE Technical Paper.
93. Fujiwara, Y., et al., *Formation of soot particulates in the combustion chamber of a precombustion chamber type diesel engine*, 1984, SAE Technical Paper.
94. Allen, C., et al., *Application of a novel charge preparation approach to testing the autoignition characteristics of JP-8 and camelina hydroprocessed renewable jet fuel in a rapid compression machine*. Combustion and Flame, 2012. **159**(9): p. 2780-2788.
95. Miller, D., et al., *Novel Biofuel Formulations for Enhanced Vehicle Performance*, 2013, Michigan State University.
96. Hiaki, T.T., Kenji; Tsuji, Tomoya; Hongo, Masaru; Kojima, Kazuo., *Normal Boiling Point: Pentane, 2,2,4-trimethyl-*, 1994, National Institute of Standards and Technology: NIST Chemistry WebBook.
97. Van Basshuysen, R. and F. Schäfer, *Internal combustion engine handbook-basics, components, systems and perspectives*. Vol. 345. 2004.
98. Schock, H., et al., *Internal combustion engine*, 2013, Google Patents.
99. Tanaka, S., F. Ayala, and J.C. Keck, *A reduced chemical kinetic model for HCCI combustion of primary reference fuels in a rapid compression machine*. Combustion and flame, 2003. **133**(4): p. 467-481.
100. Gentz, G.R. and E. Toulson, *Experimental Studies of a Liquid Propane Auxiliary Fueled Turbulent Jet Igniter in a Rapid Compression Machine*. SAE International Journal of Engines, 2016. **9**(2016-01-0708): p. 777-785.

101. Chiera, D., M. Riley, and G.J. Hampson. *Mechanism for High Velocity Turbulent Jet Combustion From Passive Prechamber Spark Plug*. in *ASME 2012 Internal Combustion Engine Division Fall Technical Conference*. 2012. American Society of Mechanical Engineers.
102. Walton, S., et al., *An experimental investigation of iso-octane ignition phenomena*. *Combustion and Flame*, 2007. **150**(3): p. 246-262.
103. Serras-Pereira, J., et al., *Characteristics of ethanol, butanol, iso-octane and gasoline sprays and combustion from a multi-hole injector in a DISI engine*. *SAE International Journal of Fuels and Lubricants*, 2008. **1**(2008-01-1591): p. 893-909.
104. Roshanghalb, F., *Study of the far field of a pulsed spray from an automotive fuel injector*. 2015: MICHIGAN STATE UNIVERSITY.
105. Heywood, J.B., *Internal combustion engine fundamentals*. Vol. 930. 1988: McGraw-hill New York.
106. Benajes, J., et al., *Conceptual model description of the double injection strategy applied to the gasoline partially premixed compression ignition combustion concept with spark assistance*. *Applied Energy*, 2014. **129**: p. 1-9.
107. Zheng, M., G.T. Reader, and J.G. Hawley, *Diesel engine exhaust gas recirculation—a review on advanced and novel concepts*. *Energy conversion and management*, 2004. **45**(6): p. 883-900.
108. Caton, J.A., *Combustion phasing for maximum efficiency for conventional and high efficiency engines*. *Energy Conversion and Management*, 2014. **77**: p. 564-576.
109. Zheng, B., T. Yin, and T. Li, *Analysis of Thermal Efficiency Improvement of a Highly Boosted, High Compression Ratio, Direct-Injection Gasoline Engine with LIVC and EIVC at Partial and Full Loads*, 2015, SAE Technical Paper.
110. Kokjohn, S., et al., *Fuel reactivity controlled compression ignition (RCCI) combustion in light-and heavy-duty engines*. *SAE International Journal of Engines*, 2011. **4**(2011-01-0357): p. 360-374.
111. Heuser, B., et al., *Experimental Investigation of a RCCI Combustion Concept with In-Cylinder Blending of Gasoline and Diesel in a Light Duty Engine*, 2015, SAE Technical Paper.
112. Ikeya, K., et al., *Thermal efficiency enhancement of a gasoline engine*. *SAE International Journal of Engines*, 2015. **8**(2015-01-1263): p. 1579-1586.
113. Loeper, P., et al., *Experimental investigation of light-medium load operating sensitivity in a gasoline compression ignition (GCI) light-duty diesel engine*, 2013, SAE Technical Paper.

114. Olesky, L.M., et al., *The effects of diluent composition on the rates of HCCI and spark assisted compression ignition combustion*. Applied Energy, 2014. **124**: p. 186-198.